Generation, Ascent and Eruption of Magma on the Moon: New Insights Into Source Depths, Magma Supply, Intrusions and Effusive/Explosive Eruptions (Part 2: Predicted Emplacement Processes and Observations)

James W. Head[1] and Lionel Wilson[1,2]

[1]Department of Earth, Environmental and Planetary Sciences
Brown University, Providence, RI 02912 USA.

[2]Lancaster Environment Centre, Lancaster University,
Lancaster LA1 4YQ, UK

Submitted to *Icarus* Special issue on Lunar Reconnaissance Orbiter:
January 1, 2016
Review Received March 17th, 2016
Revised Version Submitted April 21st, 2016

Abstract

We utilize a theoretical analysis of the generation, ascent, intrusion and eruption of basaltic magma on the Moon to develop new insights into magma source depths, supply processes, transport and emplacement mechanisms via dike intrusions, and effusive and explosive eruptions. We make predictions about the intrusion and eruption processes and compare these with the range of observed styles of mare volcanism, and related features and deposits. Density contrasts between the bulk mantle and regions with a greater abundance of heat sources will cause larger heated regions to rise as buoyant melt-rich diapirs that generate partial melts that can undergo collection into magma source regions; diapirs rise to the base of the anorthositic crustal density trap (when the crust is thicker than the elastic lithosphere) or, later in history, to the base of the lithospheric rheological trap (when the thickening lithosphere exceeds the thickness of the crust). Residual diapiric buoyancy, and continued production and arrival of diapiric material, enhances melt volume and overpressurizes the source regions, producing sufficient stress to cause brittle deformation of the elastic part of the overlying lithosphere; a magma-filled crack initiates and propagates toward the surface as a convex upward, blade-shaped dike. The volume of magma released in a single event is likely to lie in the range 10^2 km^3 to 10^3 km^3, corresponding to dikes with widths of 40-100 m and both vertical and horizontal extents of 60-100 km, favoring eruption on the lunar nearside. Shallower magma sources produce dikes that are continuous from the source region to the surface, but deeper sources will propagate dikes that detach from the source region and ascend as discrete penny-shaped structures. As the Moon cools with time, the lithosphere thickens, source regions become less abundant, and rheological traps become increasingly deep; the state of stress in the lithosphere becomes increasingly contractional, inhibiting dike emplacement and surface eruptions.

In contrast to small dike volumes and low propagation velocities in terrestrial environments, lunar dike propagation velocities are typically sufficiently high that shallow sill formation is not favored; local low-density breccia zones beneath impact crater floors, however, may cause lateral magma migration to form laccoliths (e.g., Vitello Crater) and sills (e.g., Humboldt Crater) in floor-fractured craters. Dikes emplaced into the shallow crust may stall and produce crater chains due to active and

passive gas venting (e.g., Mendeleev Crater Chain) or, if sufficiently shallow, may create a near-surface stress field that forms linear and arcuate graben, often with pyroclastic and small-scale effusive eruptions (e.g., Rima Parry V). Effusive eruptions are modulated by effusion rates, eruption durations, cooling and supply limitations to flow length, and pre-existing topography. Relatively low effusion rate, cooling-limited flows lead to small shield volcanoes (e.g., Tobias Mayer, Milicius); higher effusion rate, cooling-limited flows lead to compound flow fields (e.g., most mare basins) and even higher effusion rate, long-duration flows lead to thermal erosion of the vent, effusion rate enhancement, and thermal erosion of the substrate to produce sinuous rilles (e.g., Rimae Prinz). Extremely high effusion rate flows on slopes lead to volume-limited flow with lengths of many hundreds of kilometers (e.g., the young Imbrium basin flows).

Explosive, pyroclastic eruptions are common on the Moon. The low pressure environment in propagating dike crack-tips can cause gas formation at great depths and throughout dike ascent; at shallow crustal depths both the smelting reaction and the recently documented abundant magmatic volatiles in mare basalt magmas contribute to significant shallow degassing and pyroclastic activity associated with the dike as it erupts at the surface. Dikes penetrating to the surface produce a wide range of explosive eruption types whose manifestations are modulated by lunar environmental conditions: 1) terrestrial strombolian-style eruptions map to cinder/spatter cone-like constructs (e.g., Isis and Osiris); 2) hawaiian-style eruptions map to broad flat pyroclastic blankets (e.g., Taurus-Littrow Apollo 17 dark mantle deposits); 3) gas-rich ultraplinian-like venting can cause Moon-wide dispersal of gas and foam droplets (e.g., many isolated glass beads in lunar soils); 4) vulcanian-like eruptions caused by solidification of magma in the dike tip, buildup of gas pressure and explosive disruption, can form dark-halo craters with mixed country rock (e.g., Alphonsus Crater floor); 5) ionian-like eruptions can be caused by artificial gas buildup in wide dikes, energetic explosive eruption and formation of a dark pyroclastic ring (e.g., Orientale dark ring); 6) multiple eruptions from many gas-rich fissures can form regional dark mantle deposits (e.g., Rima Bode, Sinus Aestuum); and 7) long duration, relatively high effusion rate eruptions accompanied by continuing pyroclastic activity cause a central thermally eroded lava pond and channel, a broader pyroclastic ‘spatter’ edifice, an even broader pyroclastic glass deposit and, if the eruption

lasts sufficiently long, an associated inner thermally eroded vent and sinuous rille channel (e.g., Cobra Head and Aristarchus Plateau dark mantle).

The asymmetric nearside-farside distribution of mare basalt deposits is most plausibly explained by crustal thickness differences; intrusion is favored on the thicker farside crust and extrusion is favored on the thinner nearside crust. Second-order effects include regional and global thermal structure (areal variations in lithospheric thickness as a function of time) and broad geochemical anomalies (the Procellarum-KREEP Terrain). Differences in mare basalt titanium content as a function of space and time are testimony to a laterally and vertically heterogeneous mantle source region. The rapidly decreasing integrated flux of mare basalts is a result of the thermal evolution of the Moon; continued cooling decreased diapiric rise and mantle melting, thickened the lithosphere, and caused the global state of stress to be increasingly contractional, all factors progressively inhibiting the generation, ascent and eruption of basaltic magma. Late-stage volcanic eruptions are typically widely separated in time and characterized by high-volume, high-effusion rate eruptions producing extensive volume-limited flows, a predictable characteristic of deep source regions below a thick lithosphere late in lunar history. This improved paradigm for the generation, ascent, intrusion and eruption of basaltic magma provides the basis for the broader interpretation of the lunar volcanic record in terms of variations in eruption conditions in space and time, and their relation to mantle heterogeneity and a more detailed understanding of lunar thermal evolution.

I. Introduction:

Planetary crusts have been classified into three basic types, primary, secondary and tertiary (Taylor, 1989) (Figure 1a). *Primary crust* is that formed from initial accretional energy in the late stages of planetary formation, and involves large scale melting at the magma ocean scale; depending on planetary size and the composition of the material being melted, temperature-pressure gradients and mineral buoyancy, primary crust may be a plagioclase-dominated flotation crust, as in the Moon, or a more complex mafic crust. *Secondary crust* is derived from partial melting of the predominantly mafic mantle and is typically basaltic in composition. *Tertiary crust* is formed by the recycling of primary and secondary crust; examples include continental crust on Earth and basal

melting of basaltic crust by impinging mantle plumes. On the Moon tertiary crust might derive from evolution of secondary crust magmas or remelting of primary crust. The primary focus of our analysis is the formation of basaltic secondary crust, by partial melting of the lunar mantle following the formation and solidification of the anorthositic primary crust derived from the magma ocean (Shearer et al., 2006) (Figure 1a). Although visibly significant (~18 percent of the surface, primarily on the lunar nearside) (Figure 1b), the volume percentage of the total lunar crust formed by the lunar maria is less than 1% (Head, 1976; Head and Wilson, 1992). Mare deposits, however, represent the products of mantle melting, and therefore give insight into the nature, location and evolution of interior melting, and the thermal evolution of the Moon (Head, 2001; 2002). Thus, the processes of mare basalt magma generation, ascent, intrusion and eruption are of significant interest (Wilson and Head, 1981, 2015; Head and Wilson, 1992), and the resulting emplacement processes, deposits, landforms and history are the subject of this paper (Figure 1c).

New data from the Lunar Reconnaissance Orbiter (LRO) mission, related NASA missions such as the Gravity Recovery and Interior Laboratory (GRAIL) mission (Zuber et al., 2013), and international missions to the Moon (SMART 1, Foing et al., 2006; Kaguya, Kato et al., 2008; Chandrayaan-1, Goswami and Annadurai, 2009; Chang'e, Li et al., 2015), enable our analysis of the generation, ascent and eruption of magma (Wilson and Head, 2016a) and the description and interpretation of emplacement processes and the geologic record presented here. Building on the theoretical framework of the generation, ascent and eruption of magma (Wilson and Head, 2016a) derived from analysis of: 1) new data on lunar crustal thickness and structure from the GRAIL mission (Zuber et al., 2013), and 2) new data on the production of volatiles during magma ascent and eruption (Wilson and Head, 2003a; Rutherford and Papale, 2009; Saal et al., 2008; Hauri et al., 2011, 2015; Wetzel et al., 2015), we use data from LRO on the global topography of the Moon from new altimetry (Figure 1b) (Lunar Orbiter Laser Altimeter, LOLA; Zuber et al., 2010; Smith et al., 2010), and detailed characterization of lunar volcanic features and deposits using new imaging data (Lunar Reconnaissance Orbiter Camera, LROC; Robinson et al., 2010), altimetry data (LOLA; Zuber et al., 2010; Smith et al., 2010), and spectral reflectance data (Moon Mineralogy Mapper, M3; Pieters et al.,

2009). In this analysis we compare our theoretical treatment (Wilson and Head, 2016a) and its predictions with the variety and context of observed volcanic features, structures and deposits in order to test the predictions and refine the principles of ascent and eruption and to provide an interpretative framework for the major characteristics of mare basalt and related volcanism on the Moon (Wilhelms, 1987). These deposits and landforms provide fundamental information on the nature of magma generation, ascent, storage and eruption on the Moon that can be applied to other planetary bodies, including Earth, taking into account the corresponding differences in planetary gravity, presence and nature of atmospheres, crustal composition and thickness, and thermal structure and evolution.

We first summarize the basic principles of lunar secondary crustal magma generation, ascent and eruption, as treated in detail by Wilson and Head (2016a), and focus on the predicted emplacement processes. The generation, ascent and eruption of magma is controlled by a wide variety of variables (Figure 2), many of which are subject to quantitative analysis. In the mantle magma source region, fertile mantle material must be heated or decompressed sufficiently to undergo partial melting (see summary in Shearer et al., 2006) and mantle melt regions must be sufficiently interconnected at a range of scales to permit the migration and collection of partial melts into magma reservoirs (Figure 3). This requires heat sources (e.g., residual accretional heat, radioactive decay, shear) and heat concentrations of sufficient magnitude and duration to melt and collect the partial melts. The scale and geometry of the resulting magma source region is the next critical factor; small source regions may evolve in situ and ultimately solidify. For larger magma source regions, the density contrast between the heated mantle partial melts and their cooler surroundings will cause them to rise buoyantly (Figure 2), forming melt-rich diapirs. These diapirs will vary in size and shape, depending on the geometry of the heated zone, the buoyancy of the diaper, and the rheological properties of the surrounding mantle. Melt-rich mantle diapirs will rise until they reach a density trap - the base of the crust, or a rheological trap - the base of the elastic lithosphere (Figures 2, 3), here defined as the rheological transition between plastic and elastic behavior of the host rocks in the context of these strain rates.

Following the formation and evolution of the magma ocean, solidification of the anorthositic crust, density inversion of the residue and emplacement of the Mg-suite (Figure 1c) (Shearer et al., 2006; Wieczorek et al., 2006; Hiesinger and Head, 2006; Elkins-Tanton et al. 2011), the Moon progressively cooled during most of the period of mare basalt emplacement. The thermal evolution of the Moon (loss of accretional heat, waning of radioactive heat sources) caused an increase in the thickness of the lithosphere with time (Solomon and Head, 1979, 1980; Wieczorek et al., 2006; Shearer et al., 2006; Hiesinger and Head, 2006); thus, the base of the lithosphere was at relatively shallow depths earlier in lunar history and at much greater depths later in lunar history, significantly influencing the stalling depths of rising melt-rich diapirs (Figure 2). In earliest lunar history the lithosphere was thinner than the crust, and rising diapirs would have tended to stall at the base of the anorthositic crust, a density trap (Figure 2). As the lithosphere thickened in early lunar history, rising melt-rich diapirs ascended to subcrustal depths and stalled at the base of the lithosphere. At this point, residual buoyancy, combined with magma overpressurization by the continued production and arrival of diapiric material, produced sufficient stress to causes brittle deformation of the elastic part of the overlying lithosphere (Figure 3). Magma-filled cracks (dikes), convex-upward in shape and blade-shaped in cross-section (Figure 4), propagated upward from the magma reservoir. The size of a dike (length, width and height) was to first order dependent on the elastic properties of the host rocks and the buoyancy of the melt leaving the diapir. The volume of magma released from the magma source region in a single event was commonly a very small fraction (less than a few percent) of the total source region volume. Even so, the volumes of magma released in these events are likely to have been in the range of several tens of km^3 to over a thousand km^3 (Wilson and Head, 2016a).

From this point, magma in the dikes rose buoyantly toward the surface and its fate was influenced by the following factors (Figure 5a): 1) heat loss to the surrounding wall rock can cause crystallization, viscosity increase and ultimate solidification of the dike prior to reaching the surface; 2) the combination of source region pressure and magma-host rock density contrast may be insufficient to continue to support the magma column in the dike; 3) available magma in the source region may be depleted; 4) the stress

intensity in dike tip may become insufficient to fracture overlying rocks. Dikes that suffered from these fates (Figure 5a) would stall, and solidify in the mantle and crust and not reach the surface. Dikes that overcame these potential fates propagated toward the vicinity of the surface to form shallow intrusions (Figure 5b-d) and eruptions (Figure 5d-f). Clearly, large-volume magma batches (producing wide, long dikes) were favored to reach the surface (Figures 2, 3).

The influence of lunar thermal evolution (Figures 1c, 2) on the generation, ascent and eruption of magma was significant. First, as the Moon cooled, average mantle temperatures decreased, and source regions deepened and were less abundant. Secondly, the lithosphere thickened, causing rising melt-rich diapirs to stall at greater depths; volumes of magma emplaced in dikes were now insufficient to retain a source-to-surface connection and dikes pinched off and rose as buoyant penny shaped diapiric dikes, independent from the source region. Thirdly, the cooling of the Moon (e.g., Wieczorek et al., 2006) resulted in a transition from a global net extensional state of stress in the lithosphere to net contractional, and as the Moon continued to cool, the net contractional state of stress in the lithosphere increased in magnitude, further inhibiting the ability of dikes to reach the surface (Head and Wilson, 1992).

The net effect on mare volcanic history was to require deeper source regions with time (Figure 2), and also increased volumes of melt in dikes in order to overcome the net contractional state of stress in the lithosphere and allow them to reach the surface from such great depths, and erupt. The direction dictated by the thermal evolution of the Moon is clear (Solomon and Head, 1980; Head and Wilson, 1992; Wieczorek et al., 2006): the high surface area to volume ratio of the Moon enhances conductive heat loss and causes efficient cooling with time, resulting in lithospheric thickening, decrease in magma generation, increase in depth of production, and increasing difficulty of propagating dikes to reach the surface (Figure 2).

In summary, the theoretical treatment of the generation, ascent and eruption of lunar mare basalt magma (Wilson and Head, 2016a) predicts that the geological record of mare basalt volcanism (Figure 1c) will be closely linked to lunar thermal evolution, with more abundant and relatively shallow sources early on, and less abundant, more deeply sourced and more voluminous eruptions later on, ultimately leading to lower volumes of magma

generation and greater difficulty in propagating magma the increasingly greater distance from the source to the surface (Figure 2).

The intrusion of dikes into the shallow part of the crust, with some dikes stalling and others intersecting the surface, can result in a host of variations in emplacement processes, geological settings for eruption styles, and resulting landforms (Figures 5-16). The production of gas in the shallow crust by volatile exsolution and the smelting reaction (both of which take place in the low pressure regions in the propagating tips of all dikes even if they do not reach the surface) can lead to explosive eruptions (Figure 5a-f), both accompanying effusive eruptions and independent of them. Together, these features and landforms provide the surface geologic record of mare volcanic history predicted by theoretical treatments (e.g., Wilson and Head, 1981, 2003a,b, 2015; Head and Wilson, 1992a). The purpose of this paper is to summarize the range of eruption environments, emplacement processes and styles predicted by theory (Wilson and Head, 2016a) as a basis for comparison to observed landforms and deposits, in order to test and evaluate these predictions, and to provide a suite of examples of these candidate processes.

II. Predicted Emplacement Processes, Eruption Conditions, Eruption Styles and Landforms:

Various intrusion geometries and eruption styles have been observed and classified on the Earth and this range primarily represents differences in magma composition, viscosity, volatile content (abundance and type), magma/rock density contrast, magma cooling behavior, effusion rate, atmospheric pressure and tectonic environment (see summary for the Earth and Moon in Wilson and Head, 1981). The styles, landforms and deposits that occur on each planetary body reflect the basic differences in fundamental planetary variables such as acceleration due to gravity, presence, absence and nature of an atmosphere, crustal and mantle composition and configuration, tectonic environment, and thermal evolution. We have explored these variables on the Earth and Moon (Wilson and Head, 1981, 1988, 2003a,b, 2007a,c, 2015; Head and Wilson, 1979, 1987, 1989, 1991, 1992; Head et al., 1996), Venus (Head and Wilson, 1986, 1992b, Head et al., 1992), Mars (Wilson and Head, 1994, 2007b; Head and Wilson, 2002) and Mercury

(Wilson and Head, 2008; Head and Wilson, 2016a). Variations in these parameters produce a physical continuum of eruption styles, and some eruption styles do not occur or are significantly modulated due to different planetary environments. For example, the terrestrial tectonic environment has a major influence on dike emplacement processes and rates (Head et al., 1996), the presence of large bodies of surface water (oceans) on Earth significantly modifies the presence and style of explosive eruptions (Head and Wilson, 2003) and cooling lava flows, relative to the terrestrial subaerial environments, producing styles and landforms not seen on the Moon. Surface water, near-surface water, and ice in the subaerial regions of the Earth can produce volcano-water/ice interactions (Wilson and Head, 2007) that find parallels on Mars (Head and Wilson, 2007c) but not on the Moon. The low gravity of the Moon, combined with the lack of an atmosphere, the depth of melting and the large volumes of ascending and erupting magma, and differences in volatile production sources and abundances, result in some fundamental variations on the basic terrestrial subaerial eruption styles. For example, as gas and foam-rich dike tips penetrate to the lunar surface, they vent into a vacuum, precluding the incorporation of atmosphere to form a convecting ash-gas cloud as in classic plinian eruptions on Earth (Figure 5d-f). Instead, ultraplinian jets are initially formed. Furthermore, classic strombolian and hawaiian eruption styles (Head and Wilson, 1987, 1989) are highly modified on the Moon: the terrestrial gas/clast cloud above the vent ceases expanding when it reaches atmospheric pressure, resulting in a narrow spread angle from the vertical on Earth (Head and Wilson, 1989). In contrast the plume that forms in the lunar vacuum at $1/6^{th}$ Earth gravity (Head and Wilson, 1989; Weitz et al., 1988, 1989; Weitz and Head, 1999) consists of clasts decoupling from a hemispherically expanding gas cloud and following ballistic trajectories, leading to a parabolic upper envelope to the flight paths, thus forming the same umbrella shape as seen in the plumes on Io. Although the basic physics is the same, there is a significant variation in the distribution of clasts and their cooling behavior, the distribution of optical density in the cloud, and the fate of pyroclasts. "Hawaiian"-style eruptions on the Moon produce widely dispersed pyroclasts and widespread and thin blankets of tephra, with tephra-cone-like accumulations only in the very optically thick inner portion of the cloud (Weitz et al., 1998, 1999) (Figure 9). In some cases, these clasts arrive so rapidly and in such abundance that they can coalesce

into a pond and cause thermal erosion (Figure 9a), rather than accumulating into a tephra cone. "Strombolian"-style activity on the Moon is limited to near-vent accumulation of clasts too large to be incorporated in the expanding gas cloud (Figure 10). On the basis of these basic principles for the Moon, we now proceed to describe and graphically illustrate the range of predicted emplacement processes and eruption styles described by Wilson and Head (2016a).

Dikes rising from the mantle into the crust can stall in the shallow crust due to a variety of causes (Figure 5a), including insufficient density contrasts, excessive cooling, and depletion of magma in the mantle source region. Some dikes will reach a level of neutral buoyancy at a local low-density zone (for example, the breccia lens below an impact crater floor) and propagate laterally (Figure 5b), forming a laccolith or sill. In this case, the gas/foam layer at the upper dike tip will participate in the inflation and uplift of the overlying rocks and may vent to the surface through cracks. In some cases, stalled dikes can build up additional free gas at the top of the dike due to convection in a wider-than-average dike (Head et al., 2002) leading to propagation of a gas-filled fracture to the surface and a very gas-rich Ionian-style eruption (Figure 5f). If the dike stalls in the shallow crust, and the pressure in the gas/foam layer exceeds the tensile strength of the overlying rocks (Figure 5c), the overlying rocks will fracture and the gas in the upper part of the dike will vent to the surface vacuum (Figure 5d). Initial venting of the gas (Figure 5e) occurs at velocities of 1-1.5 km/s, reminiscent of ultraplinian eruption conditions on Earth, and entrained regolith and small clasts of wall rock can be extremely widely dispersed, up to 2000-5000 km, essentially antipodally. As the gas layer undergoes catastrophic expansion (Figure 5e), an expansion wave propagates into the underlying foam, causing its collapse and venting to the surface. This results in an energetic, but more areally restricted, eruption lasting until the foam is depleted. Deposition of pyroclasts can range up to ~25 km radius. In the case of the stalled dike (Figure 5d), some further gas exsolution from the magma at the top of the dike may occur, but the dike is likely to cool and solidify in the upper crust. This eruptive environment is different from that in which the dike continues to propagate to the surface and vent (Figure 5d), leading to choked or unchoked flow (Figure 7).

The surface manifestation of dikes that stall in the shallow crust can be visualized by illustrating the dike in cross-sectional view (Figure 6a) and side view (Figure 6b). The magma rises as a blade shaped (cross-sectional view) and penny-shaped (side view) magma-filled crack that is producing a gas/foam accumulation at the dike tip (Figure 6a); this gas/foam increases considerably in volume and rate of accumulation in the shallow crustal zone of maximum volatile production through the smelting reaction and magmatic volatile exsolution (Figure 6b). If the dike stalls relatively deeper in the crust, the near-surface extensional stress field caused by the emplacement of the dike is insufficient to cause graben-forming deformation. However, the dike may still be shallow enough that the gas/foam overpressure exceeds the tensile strength of the overlying rock, and the gas catastrophically vents to the surface, forming pyroclastic deposits from the collapsed foam (Figure 5d-f; 6c). Venting of gas and foam in the upper part of the dike is predicted to manifest itself as a series of craters aligned along the top of the dike (Figure 5d, 6c). Due to the active nature of this process, supporting evidence for this situation would be the presence of positive crater rim topography and perhaps some evidence for venting of pyroclasts from the collapsed foam (Figure 6c). Alternatively, the dike may not reach sufficient overpressure to fracture the overlying rocks and vent catastrophically, but instead may vent diffusively and passively, forming a series of collapse craters over the dike location. In this case (Figure 6c), regolith will drain into the vacated gas cavity, and raised rims in craters in the chain would not be predicted to form. Raised rims are not likely to be formed due to the very rapid expansion of the gas in a vacuum if the dike propagates to the surface (Figure 5e).

Dikes stalling below the surface and not immediately venting to the surface by either dynamic or diffusive processes can continue to build up volatiles in the dike tip by convection in magma in the upper part of the dike (Figure 5f). In this case, convective overturn of magma in the upper part of the dike causes degassed magma to sink, and relatively undegassed magma to ascend into the shallow region of maximum volatile production. This activity would be favored for wider, longer dikes (those more susceptible to convection). Continued gas production could occur along a significant part of the upper convex-upward dike (Figure 6b), and this gas would become concentrated at the dike top, closest to the surface. Such concentrations could lead to very energetic

eruptions of gas/collapsed-foam mixtures (Ionian-like; Head et al., 2002; Figure 5f) and result in the formation of extremely large circular, linear and irregular pits and depressions through a combination of initial explosion, followed by collapse, subsidence and drainage into the vacated gas cavity. Void space associated with the upper part of a convex upward dike ~100 km in length and ~250 m wide could easily approach 15-60 km^3 (Wilson et al., 2011). This volume alone could translate into ~5-20 drainage pits with a diameter of ~3.5 km and depth of ~500 m (with the pit walls at the angle of repose).

Dikes propagating into shallower parts of the crust, but not immediately venting to the surface, can set up near-surface stress fields (Figure 6a, d) that result in graben forming above the dike (Figure 8). These graben are predicted to show variations in lengths and widths linked to the widths and depths of the dike intrusion. Of course, lunar graben can also be related to purely tectonic forces in cases where extensional lithospheric stresses lead to failure (McGill, 1971; Golombek 1979). This is seen most prominently on the Moon associated with lithospheric loading by mare basalts, flexure and graben formation around the mare-filled impact basins (Solomon and Head, 1979, 1980). Indeed, the temporal variation in stress distribution associated with mare basalt loading in lava-filled impact basins can itself influence the regional lithospheric stress orientation associated with dike emplacement, favoring certain pathways and orientations of dike ascent, propagation and eruption (Solomon and Head, 1979, 1980; McGovern et al., 2014). Thus, lunar graben could be 1) purely tectonic in origin, 2) related to near surface stresses associated with shallow dike emplacement and stalling (such examples commonly should show evidence of venting along their strike in the form of collapse pits, small pyroclastic cones, and/or small mare patches), and 3) related to near surface stresses associated with deeper dike emplacement and stalling (such examples may not show evidence of venting along their strike) (Petrycki et al., 2004).

It is reasonable to assume that dikes that get closer to the surface are vertically more extensive and so are also wider on average, the length/width ratio being determined by rock mechanics. A dike that stalls at a significant depth below the surface is the one least likely to form volcanic features (Figure 8a). Because its top is deep, for fixed fault angles the resulting graben will be wider. Also because the dike is deep, it does not force the

crust apart as much, so the resulting graben is shallower (Figure 8a). The reverse is true for a dike that penetrates closer to the surface (Figure 8b). This dike will be wider, and also is more likely to produce minor eruptions: the graben is less wide, but because the dike is wide it forces the crust apart more, and the graben is predicted to be deeper.

First we consider the shallow dike "with surface volcanics" case (Figure 8b). If a dike propagates to a very shallow depth in the lithosphere in a state of neutral tension, the dike forces the crust apart and the resultant fractures form a graben. The dike width is *W*, the average graben half-width is *H*, the graben subsidence depth is *S* and the hade of the fault (inclination from the vertical) is angle *A*. The depth to the top of the dike is *Z*. From simple geometry:

$$Z = (S / 2) + (H / \tan A) \qquad (1)$$

Neglecting compaction changes, simple conservation of volume requires that the dike props apart the crust above the dike top by an amount equal to the dike width, so that the potential area made available is equal to ($W Z$). This space is ultimately filled by an amount equal to the area of missing rock implied by the graben subsidence, i.e. ($2 H S$), so

$$2 S H = W Z \qquad (2)$$

Thus using equation (1):

$$W = (4 H S \tan A)/(S \tan A + 2 H) \qquad (3)$$

Average graben dips on the Moon are very close to 60 degrees (McGill, 1971; Golombek, 1979) so typical hades are ~30 degrees. On the Moon, the mean depth *S* of graben that show evidence of associated volcanics is 132 m and their mean half-width is 615 m (Petrycki et al., 2004), so the average dike width causing this amount of subsidence is *W* = ~144 m and the average depth to the dike top is *Z* = 1131 m.

Of course, not all of the graben subsidence may have been forced by the emplacement of the dike. For example, in the dike with "no-volcanics" case (Figure 8a), where the dike top did not reach a shallow depth, the dike intrusion could have triggered faulting due to pre-existing lithospheric tension. Graben that have no associated volcanics have an average graben subsidence of ~97 m and an average half-width of 915 m (Petrycki et al., 2004). Thus, the extreme assumption would be that ~97 m of the 132 m was simply due to relaxation of pre-existing tension. In this case, only 132-97 = 35 m would be due specifically to the dike intrusion. Using these values would imply that dikes associated with volcanics had a smaller dike width, close to 40 m, and a larger depth to dike top of just over 2600 m.

Dikes that stall sufficiently close to the surface could vent gas and pyroclasts to the surface derived from evolution of the gas/foam pocket at the top of the dike (Figure 5c). Such eruptions should be favored at the top of the convex-upward dike (Figure 6b), where gas might migrate and collect, enhancing the local volatile content.

Dikes propagating all the way to the surface will erupt (Figure 6e), with the central part of the convex-upward dike reaching the surface first. This convex upward geometry (Figure 6b) has a strong influence on the evolution of the eruption. The width of the dike will vary along its strike, being wider in the middle and tapering towards the edges. Initial effusion will be concentrated along the central widest part of the dike, and the narrower dike tips will progressively cool and solidify, centralizing the eruption over the course of hours to days. The enhanced centralized flux in the widest part of the dike will then feed lava flows and form extensive channels and flow deposits (Figure 6e).

Critical to the understanding of eruption conditions in the initial stages of the dike reaching the surface is the transition of the magma from a gas-containing fluid to a magma-droplet-containing gas, and the way in which the subsurface/surface interface accommodates to this transition (Wilson and Head, 2016a). As the magma rises toward the surface it is a single-phase fluid in which the speed of sound is relatively high (Figure 7a). As lithostatic pressure decreases, and nucleating and expanding bubbles accelerate magma rise, the magma becomes a two-phase flow (liquid plus bubbles) and the speed of sound decreases. If sonic conditions are met at the surface vent, the total mass flux is maximized, and the system adjusts to this condition. In choked flow (Figure 7a), the vent

pressure exceeds the atmospheric pressure and the magma rise speed remains equal to the sound speed. In unchoked flow (Figure 7b), the vent pressure equals the local atmospheric pressure. The lunar vacuum results in the condition that virtually all lunar eruptions are choked. Magma disruption may occur below the vent but otherwise will occur through a series of shocks immediately above the vent (Figure 7a) and the two-phase fluid (now gas and pyroclasts) decompresses to atmospheric pressure (the vacuum in this case), accelerating the gas to supersonic speeds (Figure 7c). The gas density is initially sufficiently high to accelerate the smaller particles, while progressively larger particles fall out of the expanding gas cloud closer to the vent. The smaller particles continue to accelerate in the expanding gas cloud until the gas density becomes so small (i.e. the Knudsen regime is reached) that the drag force between particles and clasts becomes negligible; the individual small particles decouple from the still-expanding gas flow and continue their travel on ballistic trajectories, ultimately falling to the surface to form a thin and widely dispersed pyroclastic deposit. This environment is clearly favorable for radial pyroclast sorting, with the finest particles maintaining coupling with the expanding gas cloud the longest, and being most widely dispersed, and the coarsest particles decoupling from the cloud earliest and landing closest to the vent. This geometry (Figure 9a) also results in significant variations in the optical density of the expanding gas/pyroclast cloud, creating a very wide variety of consequences for eruption styles and associated features and deposits (Figure 9b). In the inner part of the cloud (Figure 9a), the high number of particles makes the cloud optically dense, inhibiting heat radiation and loss, so that particles do not cool effectively and essentially reach the ground at magmatic temperatures, coalescing into a lava pond to feed a lava flow. Where motion in the pond is turbulent, thermal erosion can result, forming an eroded depression around the vent; the pond in the depression feeds lava into flows forming thermally eroded sinuous rilles. In the optically thinner outer edge of the fountain (Figure 9a), pyroclastic particle density is low and particles are smaller, both maximizing heat radiation and cooling. Particles continue accelerating until they decouple from the gas cloud, and then follow ballistic trajectories to the ground, continuing to cool throughout their trajectory. Their ultimate fate, glass content, and mineralogic character can be predicted from their position in the expanding gas cloud; samples of pyroclasts returned

from the Moon can be linked to their position in the plume in this model (Figure 9b,c) (Weitz et al., 1998, 1999).

Lunar 'strombolian' eruption styles occur in the region very close to the vent (Figure 10). A wide range of pyroclast sizes can be produced by shearing forces at the edge of the conduit. In addition, variations in gas bubble sizes can produce variations in bubble wall thickness that map out into variations in disrupted bubble wall droplet volume and droplet sizes. Approximately 80% of the erupted clasts are so coarse that they acquire only ~50% of the gas speed, and they thus fall out of the ejecta cloud in the vicinity of the vent. Clast accumulations should form spatter/tephra cones within about 1-2- km radius of the vent. The remaining 20% of the clasts (typically less than about 1 mm in size) that are exposed to increased gas acceleration increase their speeds by up to a factor of 3 to 4, and their ranges by 10 to 15 times, producing pyroclastic mantles surrounding the vent out to ~10-30 km radius.

What is the relationship between volume eruption rates and pyroclastic properties surrounding eruptive vents? Table 1 shows a series of blocks of solutions, one for each of a wide range of volume eruption rates of magma between 50 and 100,000 $m^3 s^{-1}$. Lunar magma is assumed to have a viscosity of 1 Pa s and a density of 2900 kg m^{-3} (Wilson and Head, 2016a). Each block treats a wide range of possible total volatile contents, *n*, assumed to be dominated by CO, between 100 ppm and 10,000 ppm. In earlier treatments (Wilson and Head, 1981; Head and Wilson, 1992; Fogel and Rutherford, 1995) it was assumed that *n* was a few to several hundred ppm, but recent work suggests values up to at last a few thousand ppm (Saal et al., 2008; Hauri et al., 2011, 2015; Wetzel et al., 2015). For each *n* in Table 1, values are given for: 1) the maximum range, R_f, of pyroclasts (assuming a polydisperse grainsize distribution with median 300 microns); 2) the radial width, *X*, of the optically thin outer shell of the fire-fountain where pyroclasts can cool; 3) the difference between R_f and *X*, which gives the radius of the hot pond that forms; and 4) the Reynolds number of the motion of the lava in the hot pond.

For volume fluxes less than 200-300 $m^3 s^{-1}$, there is no turbulence in the accumulating ponds and so significant thermal erosion is not expected. At these low volume fluxes and for CO contents up to ~600 ppm hot ponds with radii between ~250 and ~700 m form,

surrounded by cool shells (capable of building spatter/cinder cones) several tens to several hundred meters wide. If the accumulation is slightly asymmetric or on a slope, so that part of the spatter structure gets rafted away, a breached cone and a (technically rootless) laminar lava flow can be produced. If the gas content exceeds a critical value in the range ~200 to ~600 ppm at these low volume fluxes, there is no optically dense zone and all the pyroclasts are able to cool significantly, producing localized cool to cold deposits with radii that are up to ~3 km for n = 1000 ppm and ~10 km for n = 3000 ppm. The smallest examples of these would appear as wide, low cinder cones with no associated lava flows. The importance of this is that cinder cones, and also cinder/spatter cones feeding laminar lava flows, can be produced from steady eruptions, i.e., without invoking Strombolian activity, for a wide range of gas contents as long as the volume flux is less than 200-300 $m^3 s^{-1}$.

For all erupted volume fluxes greater than 200-300 $m^3 s^{-1}$, turbulence is predicted in the accumulating lava pond for some part of the range of gas contents, n (Table 1). The range of values of n for which this occurs increases as the erupted volume flux increases. Of course, as the range of values of n increases, the largest value of n for which turbulence occurs also increases, and so the radius of the hot pond also increases; all the possible combinations are highlighted in bold in Table 1. However, sinuous rille source depressions are only observed with radii (for circular depressions) or half widths (for elongate depressions) up to about 2 km (Head and Wilson, 1980), and so in Table 1 all combinations that lead to ponds larger than this are underlined and in italics - these are physically possible but not actually observed on the Moon. The implication of these predictions and observations is that values of n for sinuous rille-forming eruptions rarely exceed about 700 ppm; this is entirely consistent with earlier, less-detailed analyses (Head and Wilson, 1981) that found values up to ~450 ppm.

Steady magma eruptions will produce lava flows (Figure 11a), with commonly accompanying pyroclastic activity. Initial dike penetration forms a fracture and results in gas and collapsed foam release, with initial fine-grained pyroclasts dispersed widely. Coarse pyroclasts land near the vent and are carried away by the lava flow. As the marginal parts of the dike cool, effusion centralizes over the widest part of the dike and centralizes flow (Figure 6e). On the basis of the range of volume eruption rates predicted

from magma sourced at great depth (Wilson and Head, 2016a), typical eruption rates can lie in the range from 10^4 to 10^6 m^3 s^{-1}. Resulting lava flows are predicted to be commonly 10-20 km wide, often >10 m thick and often 200 km in length. A lava flow erupting in the daytime (surface temperature ~100 ^oC) will cool less efficiently than a nighttime eruption (surface temperature ~-173 ^oC), but eruption duration is likely to significantly exceed two weeks, so any differences may be averaged out. Heat loss mechanisms from simple lava flows (Figure 11b) consist of conduction to the substrate below the flow, radiation from the top of the flow and, in planets with an atmosphere, convection, including natural, and forced (wind). These lava flow cooling processes result in an increasingly thick upper, marginal and lower thermal boundary layer as a function of distance from the vent. The absence of atmosphere on the Moon slightly reduces the cooling rates of flow tops and margins. With time, cooling of the lava flow margins penetrates into the flow interior, slowing its forward motion; when the Grätz number (Wilson and Head, 2016a) reaches ~300, the flow will stop advancing.

This condition represents one of the three common limits to lava flow length: *cooling-limited* flows (Figure 12). Cooling-limited flows can often be recognized by the behavior of the more proximal parts of the flow where cooling has progressed to a lesser degree (Figure 12b), and the continuing supply of magma to the flow can inflate the flow behind the cooled front and breach the thinner parts of the thermal boundary layer, forming breakout flows (Figure 12b). Cooling-limited flow behavior is favored in lower-volume-flux eruptions, which optimize cooling time. A second type of flow-length limit comes from supply limitations. In *supply-limited* or *volume-limited* flows (Figure 12a), the supply of magma from the source region is exhausted before any cooling limitation can be reached. A third type of flow-length limit can be reached by the flow encountering a topographic depression (Figure 12c), in which the flow ponds and the flow surface inflates, assuming the shape of the outline of the depression. This typically happens in impact craters, intercrater depressions and in tectonic depressions. In addition, positive topography (ridges, mounds, crater rims) can also serve to create barriers and diversions to the forward advancement of lava flows.

Wilson and Head (2016a) summarized earlier work on the formation of sinuous rilles by thermal erosion, showing that the low viscosity of lunar lavas, combined with the

shallow slopes of pre-existing lava surfaces within mare basins, meant that small differences in slope or effusion rate could determine whether lava flows were turbulent or laminar, and hence more or less likely to erode sinuous rilles. Later detailed models of thermal erosion using explicit thermal and mechanical properties of volcanic rocks known or inferred to be present on planetary surfaces were developed for eruptions on several planets, including the Moon (Williams et al., 2000; Hurwitz et al., 2012), and Wilson and Head (2016a) showed that these newer models concur with the earlier work in requiring eruptions lasting typically a few months to explain the observed depths of the rille channels. Wilson and Head (2016a) further related sinuous rille formation to lava eruption rates, using arguments developed by Head and Wilson (1980, 1981) and Wilson and Head (1980) that utilize the observed widths of sinuous rille channels and the geometries of the source depressions that feed the rilles.

Assuming that the motion must be fully turbulent for efficient thermal erosion implies that the minimum volume flow rate through the rille channel must be ~300 $m^3 s^{-1}$. More stringent limits can be set by considering the turbulent lava ponds that feed the rilles, and Wilson and Head (1980) showed that the geometry of source ponds for several rilles (Prinz, Vera, Ivan, Beethoven and Handel) (Head and Wilson, 1980) give an average of ~1200 $m^3 s^{-1}$, both values being very much lower limits because the Reynolds number for the flow motion is expected to be much greater than the limiting value of ~2000; values estimated by Head and Wilson (1981) were of order 10^5. Using rille morphometric observations and Hulme's (1973) model, Head and Wilson (1981) found eruption durations of 100-300 days and volume eruption rates in the range 10^4 to 10^6 $m^3 s^{-1}$. Multiplying the durations by the volume rates implied erupted volumes of ~100 km^3 to nearly 2000 km^3.

What is the difference between lava flows and sinuous rilles? Wilson and Head (2016a) found that the smallest volume flux likely to be associated with an eruption feeding a typical mare lava flow was ~10^4 $m^3 s^{-1}$, and that typical flows were fed by eruption rates in the range 10^5 to 10^6 $m^3 s^{-1}$ producing flow volumes of order 100 km^3. The previous discussion shows that sinuous rille-forming eruptions have similar minimum and maximum magma discharge rates and minimum magma volumes. However, the rille-forming eruptions commonly involved greater magma volumes

erupted over much longer periods of time. The longer eruption durations appear to be the key factor in the ability of these flows to erode rille channels.

Additional distinctive properties of sinuous rilles include narrower precursor lava flows erupted from vents with much smaller horizontal extents than those feeding the more common sheet-like flows (Oberbeck et al., 1971; Hurwitz et al., 2013). Indeed, where the sources of the rilles are circular depressions, it is not the actual vent geometry that defines the lava flow width but rather the size of the overflowing lava pond feeding the flow, which in turn is dictated by the explosivity of the eruption (Figure 9a). An additional significant factor is related to the long duration of the sinuous-rille forming eruptions (Figure 13). In long-lasting fissure eruptions, activity progressively focuses toward the center of the active fissure, so that eventually just a short fissure segment or a single localized vent is active. If flow in a fissure continues for long enough (Figure 13a), the walls of the feeder dike are heated and the initial dike width increases as the wall rocks are thermally eroded (Figure 13b). Wilson and Head (2016a) found that the rate of dike wall erosion will be ~15 $\mu m\ s^{-1}$. For a range of eruption conditions they showed that the magma rise speed at depth increases by ~50% as a 1600 m long fissure vent evolves into the circular shape needed to accommodate the same volume flux; the time required for the change ranged from 66 to 108 days. Given the likely 100-500 day durations of sinuous rille-forming eruptions (Hulme, 1973; Head and Wilson, 1981), it is clear why many sinuous rilles appear to be fed by relatively short fissures (Figure 13b).

Lava flow behavior and effusion rates will change as a function of time during the course of an eruption due to 1) changes in the geometry of the vent (Figure 13), and 2) integrated pressurization relationships and eruption history (Figure 14). As described previously (Figures 6a, e, 11a), the top of the dike that intersects the surface at the onset of the eruption is wider in the middle, and progressively narrows as the dike tip extremities cool, concentrating the flux in the central part of the dike (Wilson and Head, 1988), and leading to 10-20 km wide lava flows emanating from this central region. If the flow from the central part of the vent continues for some period of time (Figure 13a), over the course of 2-3 months, the active vent can widen and circularize (Figure 13b). It accomplishes this by thermally eroding the active vent walls, first melting any chilled lava from the early phases of the eruption, and then melting the adjacent dike-wall

country rock. This widening and circularizing of the vent causes a focusing of the magma flux and can result in a 50% increase in flux. The vent circularization also narrows the head of the flow (Figure 13b), with the result being high fluxes of turbulent effusive magma flow concentrated in a much narrower zone; this means that surface thermal erosion can be enhanced and concentrated over the course of up to ~500 days, providing a clear mechanism to produce thermally eroded sinuous rilles.

Lava flow behavior and effusion rates will also change as a function of time during the course of an eruption due to integrated pressurization relationships and eruption history (Figure 14). When a dike penetrates to the surface, discharge rates will be at a maximum. Subsequently, the discharge rate undergoes exponential decay, decreasing the net flux to the surface. Narrowing and closing of the dike go on continuously and may continue until the dike is so narrow that cooling intervenes and the eruption stops. If the top of the dike is at the surface and still capable of discharging magma, dikes sufficiently near the surface to let the internal excess pressure go to zero close completely except for a layer of chilled magma always present on the dike walls. If the dike is connected to a large pressurized source, i.e. a relatively shallow magma reservoir, the larger total volume than in an isolated dike means that the process is slower and the eruption lasts longer, but the decay pattern is still exponential. When magma is denser than the crust (always true for the Moon), the magma will tend to sink and this force will attempt to keep the lower parts of the dike open. During the period of global compression in later lunar history (Figure 1c), the compressive stress tries to pinch the dike completely shut at all depths but sinking magma still attempts to keep the lower part open. In either case, an equilibrium may be reached in which not all of the magma is extruded, but less will be retained at depth in the compressive case. These relationships have important implications for subsurface crustal intrusions. In early lunar history, dikes are emplaced in a global extensional stress regime (Figure 1c), have shallower source regions (Figure 2), and are thus more likely to be connected to the source region as the eruption winds down. This general environment maximizes the likelihood that the remaining dikes will tend to retain their thicknesses and solidify in the crust, a trend that will progressively make the crust more dense (Head and Wilson, 1992). Later in lunar history, dikes are emplaced in a global contractional stress regime (Figure 1c), have deeper source regions

(Figure 2), and are thus more likely to be disconnected from the source region as the eruption winds down. This general environment minimizes the addition of solidified dike material to the shallow crust.

These dike evolution relationships also have important implications for resulting surface landforms. The behavior of dikes and their surface manifestations may differ radically between the onset and the termination of the eruption. At the end of an eruption (Figure 14), the contracting and slowly closing dike may tend to expel magma from the upper part of the dike, creating a ridge-like structure of passively extruded cooled and partly solidified magma. Furthermore, any remaining volatiles may vent to the surface in a dike-pressure environment favoring low velocity eruptions and spatter-like strombolian-style accumulations. Care must be exercised to distinguish landforms and deposits associated with the main eruption from those that might be produced in the waning stages of an eruption, under very different conditions.

A final consideration is related to magmatism and volcanism in the early history of the Moon, prior to the time that the lithosphere thickened to a depth well in excess of the crustal thickness (Figure 2). In the first few hundred million years of lunar history (Figure 1c), magma ocean cooling and solidification (Shearer et al., 2006) was accompanied by lithospheric stabilization and thickening (Wieczorek et al., 2006; Elkins-Tanton et al., 2011). At some point, the thickness of the lithosphere reached the thickness of the lunar crust. Should mantle melting and mare basalt generation have been active at that time, rising diapirs would have stalled at the base of the crust/lithosphere, both a mechanical and density barrier (Figure 15). In this particular configuration, the excess pressure in the magma reservoir would have been relatively small due to its shallow depth and small vertical extent, and the low density of the overlying anorthositic crust; overpressures in the reservoir would have been insufficient to propagate dikes to the lunar surface. This mechanical and buoyancy stability of the magma reservoirs at the base of the crust/lithosphere would have encouraged 1) growth of stationary reservoirs, 2) possible sill formation, 3) long-duration of stable reservoirs (encouraging magma differentiation and volatile evolution), and 4) contact between magma reservoirs and the base of the crust (potentially enhancing heating, metamorphism and melting). Products of magma differentiation and/or crustal melting and assimilation are likely to be of lower

density then basaltic melts and could potentially form dikes that would propagate to the lunar surface and erupt (Figure 15).

III. Observed Lunar Volcanic Landforms and Processes: Relation to Predicted Eruption Processes and Conditions:

We now investigate the population of geological features associated with the period of lunar mare emplacement and secondary crustal formation (Figure 1c), with the purpose of 1) documenting the key emplacement processes, eruption types and their relationships, 2) comparing them with the theoretical predictions, and 3) assessing specific trends in eruption styles in space and time. We begin with those features that might represent buried dikes at depth, and we then proceed to effusive and explosive eruptions.

A. Dikes that propagate to the near-surface and stall: These dikes can undergo a series of predicted behaviors (Figures 5-6), ranging from dying a "heat death", solidifying and showing no surface morphologic manifestation (Figure 16), to catastrophic venting and the production of crater chains and explosion/collapse pits (Figure 6c). We describe candidate examples of each of these types of eruptions.

1) No surface manifestation: In some cases, perhaps quite commonly (Head and Wilson, 1992), dikes will propagate into the lunar crust but their rise to the surface will be halted by a combination of factors (Figure 5a). In these cases, there will be no direct surface manifestations of their presence at depth. On Earth, magnetic minerals forming in dikes stalled in the crust are susceptible to preferential orientation in the magnetic field as they cool below their Curie temperature, and linear, arcuate and radiating mafic dike swarms with recognizable magnetic signatures are common (Ernst et al., 1996; Reeves, 2000). Similar magnetized dikes should be detectable in the lunar crust if they formed during the period when the Moon is thought to have possessed a magnetic field possibly associated with a lunar dynamo, perhaps to as young an age as 3.56 Ga (Suavet et al., 2013). Rima Sirsalis, a linear graben on the southwest nearside near Mare Humorum, is one example of a graben interpreted to be characterized by an underlying dike with a magnetic signature (Srnka et al., 1979; Head and Wilson, 1993; Hood et al., 2001).

Puruker et al. (2012) produced a magnetic map of the Moon, based on Lunar Prospector magnetometer observations, that shows a set of WNW-trending linear to

arcuate magnetic features, evident in both the radial and scalar observations over a 1000 km wide region centered on the NW portion of the South Pole-Aitken (SPA) basin. Patchy mare basalts of generally late Imbrian-age are emplaced within SPA (Yingst and Head, 1997) through dikes (Head and Wilson, 1992), directly from mantle sources. Purucker et al. (2013) interpreted the magnetic features to represent dike swarms that served as feeders for these mare basalts, as evident from their close correlation with the surface mare ponds. Future high-resolution orbital magnetometry data, together with surface magnetic and seismic traverses, could identify and map the subsurface distribution and extent of these deeper crustal dikes, both those with and without surface manifestation. In general, dikes that stall and cool in the crust without reaching the surface are more likely to retain their original widths than those that erupt to the surface and decrease their thickness during, and following, the eruption (Figure 14).

2) Isolated crater chains: Crater chains (catenae), rows of craters and pits that are aligned in linear to somewhat arcuate surface patterns, are known to originate from impact, volcanic, tectonic and subsurface drainage processes. Those derived from impact processes include secondary crater chains and aligned impacts due to the breakup of projectiles from close planetary flybys, and the subsequent aligned and commonly overlapping impacts on planetary surfaces (e.g., Melosh and Schenk, 1993; Rampino and Volk, 1996; Bottke et al., 1997). Aligned projectile impacts are usually readily distinguished from those of internal sources by the abundance of ejecta from the individual craters. Secondary impact chains commonly have associated herringbone patterns from the typical low impact angle of the projectiles (e.g., Oberbeck and Morrison, 1974). Tectonic pits, caused by collapse and drainage into subsurface fault zones, are not predicted to display ejecta and are aligned along the faults, usually within graben (e.g., Horstman and Melosh, 1989; Melosh, 2011, p. 251). Collapse pits (skylights) associated with the collapsed roofs of lava flow channels and sinuous rilles, typically do not occur as extensive multiple closely spaced pits (Haruyama et al., 2009) like those of catenae.

Aligned pits not associated with graben, and not showing any characteristics of those formed from impacts and tectonism, are candidates for volcanic origins (McGetchin and Ullrich, 1973; Eppler and Heiken, 1975; Muller and Binder, 1983; Okubo and Martel,

1998). Large crater chains on the Moon with these characteristics are few, and the most prominent examples include Mendeleev, Davy, and Abulfeda. Davy crater chain (11^{o} S, 7^{o} W), slightly curved towards its western end, consists of ~46 craters aligned along the floor and rim of Davy crater for a total length of ~73 km (Muller and Binder, 1983; Wichman and Wood, 1995). Abulfeda crater chain (16.9^{o} S, 17.2^{o} W) starts at the southern rim of the crater Abulfeda, and continues for a total length of ~450 km, containing a total of 171 craters (Muller and Binder, 1983). Although not apparently radial to any prominent crater, many of the craters in the chain contain ejecta that does not appear to overlap that of adjacent craters (Muller and Binder, 1983), that might suggest simultaneous high-angle impacts associated with tidal breakup-derived projectiles (Oberbeck and Morrison, 1974). In contrast to the internal origin proposed by Muller and Binder (1983), Melosh and Whitaker (1994) interpreted these to be aligned simultaneous lunar impacts from a comet that had fragmented during a close Earth flyby, citing their lack of similarity to secondary crater chains, their isolation, and location on the lunar nearside. Simultaneous active venting of magmatic gas (Figures 6c, 16) could, however, produce ejecta interference patterns that might not be distinguishable from those produced from simultaneous impacts.

The farside Mendeleev crater chain (Eppler and Heiken, 1975) (Figure 17) is located on the floor of the 313 km diameter Mendeleev crater, and consists of ~73 craters aligned along a chain 190 km in length (Muller and Binder, 1983). The individual craters are often elongated along the strike of the chain, are both overlapping and separated from one another, and have an average diameter of 2.3 km (Muller and Binder, 1983). Impact chains formed from projectile disruption during close approach to Earth are unlikely to occur on the lunar farside (Melosh and Whitaker, 1994). Although Wilhelms and Hodges (1978) pointed out that the Mendeleev crater chain is radial to Tsiolkovsky crater, ~850 km away, no other similar examples radial to Tsiolkovsky have been documented, and the degradation state suggests an Eratosthenian or early Copernican age (Muller and Binder, 1983), younger than Tsiolkovsky. On the basis of its length (similar to the dike lengths penetrating to the near surface; Wilson and Head, 2016a), the broad size frequency distribution of individual craters, their separation, and the nature of the rims on members of the crater chain, the Mendeleev crater chain is considered one of the best

candidates for a lunar crater chain of relatively deep endogenic origin (Muller and Binder, 1983), potentially representing a combination of both active gas venting and passive regolith drainage (Figures 6b,c, 16).

In a separate category, less extensive aligned pits are sometimes seen in, and associated with, the maria, or mare eruptions. Several examples of these (Figure 18) illustrate that they may be collapse pits aligned along roofed lava flows (Haruyama et al., 2009) or flooded sinuous rilles, collapse pits along partly flooded depressions, collapse pits along the strike of a dike related to an effusive eruption (interpreted to be drainage into the vacated top of the dike), and unevenly spaced pits aligned along small linear rilles (commonly on floor-fractured craters), suggesting collapse and/or explosive venting in the case of the dark-haloed craters).

3) Isolated circular, elongated and irregular pits: These isolated rimless pits are commonly associated with mare volcanism and typically readily distinguished from impact craters by their lack of raised rims and ejecta deposits, and their association with mare volcanic features. Examples of these include circular and elongated pits at the summits of mare domes (Head and Gifford, 1980) (Figure 19a,b) and a range of elongated pits in the vicinity of mare lava source regions (Schultz, 1976a) (Figure 18). In some cases, these can be isolated dark halo craters associated with floor-fractured craters (Schultz, 1976b; Jozwiak et al., 2012, 2015a), and interpreted to be related to vulcanian-style eruptions (Head and Wilson, 1979; Figure 5g) in which the explosivity of the eruption disperses the ejecta so widely that any raised rim is difficult to detect. The origin of these pits is attributed to a range of processes, including late-stage magma withdrawal (summits of small shields), collapse along the top of dikes due to volatile release, post-formational collapse of inflated flows and lava channels (producing "skylights", for example; Haruyama et al., 2009), or explosive dispersal of ejecta as in the vulcanian examples. In some cases, as in the isolated pits and dark-halo craters that are associated with floor-fractured craters (Schultz, 1976b), these are related to the evolution of volatiles in the intruded sill (Jozwiak et al., 2012, 2015a).

4) Crater chains along graben: In a few cases, craters are aligned in chains in association with linear rilles interpreted to be graben (Figure 16). One of the largest examples on the Moon is the Rima Hyginus structure (Figure 20), consisting of the

rimless crater Hyginus, about 9 km in diameter, and two pit-containing graben radiating from Hyginus and extending northwest for ~45 km and east-southeast for ~45 km. Hyginus crater is surrounded by a smooth, low-albedo unit interpreted as mare basalt (Wilhelms, 1968), basalt lava flows or possibly pyroclastic debris (Pike, 1976) or primarily pyroclastic material (McCord et al., 1972; Schultz, 1976a; Hawke et al., 1989). Carter et al. (2009) showed that the low-albedo unit has a lower-backscatter cross section in S-band radar images than would be expected for mare basalts and very low circular polarization ratio values. These lines of evidence provide strong support for the hypothesis that the low-albedo unit is characterized by fine-grained pyroclastic mantling material. This, in turn, suggests that the intersecting graben are also likely to represent the surface manifestation of near-surface dike emplacement (Head, 1976; Head and Wilson, 1992, 1993) and that the very closely associated pits centered on the graben are related to dike emplacement and its aftermath.

Wilson et al. (2011) proposed a detailed model for the formation Hyginus, the rilles, the pits and the associated pyroclastic deposit. They showed that the geometry of the graben is consistent with the emplacement of a dike at depth that did not breach the surface. They interpreted Hyginus crater as a caldera-like feature formed by surface subsidence into a partly evacuated sill that locally grew from the upper part of a dike. Emplaced dikes have a gas-filled cavity in the upper tip of the dike (Wilson and Head, 2003a), underlain by a layer of magmatic foam (Figure 5a). Wilson et al. (2011) envisioned that a mixture of free gas from the dike tip and vesiculating and fragmenting magmatic foam from the sill erupted through the graben boundary faults to provide enough released gas to account for the extent of the pyroclastic deposit. The collapse pits in various places along the graben formed by subsidence of material into the depressurized dike tip gas cavity. Supporting evidence for this model is found in the close agreement between 1) the total volume of the pits measured from images and the volume of the dike tip gas cavity predicted by theoretical calculations and, 2) the estimated volume of the pyroclastic deposit and the calculated magmatic liquid content of the sill.

5) Graben and associated features: For many linear rilles on the Moon, their locations relative to impact basins and their orientation geometries strongly suggest that they are graben produced solely by large-scale tectonic stresses (Golombek, 1979;

Solomon and Head, 1979, 1980). Filling of the circular impact basins, such as Imbrium, Serenitatis and Crisium, by mare basalts caused central loading of the lithosphere, flexure, and the formation of circumferential graben at locations around the basins; the radial distance of graben formation is a function of the load magnitude and the elastic lithosphere thickness. However, the presence of subtle volcanic features associated with various lunar linear rilles (Schultz, 1976b; Head, 1976; Mason et al., 1976; Lucchitta and Watkins, 1978) is evidence that at least some linear and arcuate rilles are graben whose formation is linked to the shallow intrusion of dikes (Head and Wilson, 1993; Petrycki and Wilson, 1999a,b Petrycki et al., 2004).

There has been much discussion of the factors that control whether dikes originating at various depths in the lunar mantle will reach the surface and, when they do not, at what depths they will form dike-like or sill-like intrusions (Head, 1976; Head and Wilson, 1991, 1992, 1993; Wichman and Schultz, 1995, 1996; Wieczorek et al., 2001, 2006). However, the presence of the mare lavas is incontrovertible evidence that some dikes do reach the surface. Where dikes only approach the surface, there is still an element of tectonic control, in that the stress state of the lithosphere determines the near-surface orientations of dikes propagating from deep within the interior, but the presence of volcanic features associated with a linear rille certainly requires at least one dike as a magma pathway. Furthermore, the stresses associated with the pressure distribution driving magma upward to emplace a shallow dike intrusion have the potential to cause the relationships between the width and depth of the resulting rille, if one forms, to be different from those associated with graben of purely tectonic origin (Petrycki et al., 2004) (Figure 8).

A series of intersecting graben (Rimae Parry) occur in association with the craters Fra Mauro, Parry and Bonpland south of the Apollo 14 landing site (Figure 21). Head and Wilson (1993) described localized volcanic deposits along the Rima Parry V graben and cited these deposits as evidence for the presence of near-surface dike-emplaced magma. The volcanic features (a row of cones aligned along the western margin of the graben, and associated deposits; Figure 21) were interpreted by Head and Wilson (1993) to be the result of degassing and minor pyroclastic eruption subsequent to dike emplacement at shallow depth and graben formation. They investigated the hypothesis that Rima Parry V

was the near-surface manifestation of a dike intruded to swallow depth and that the graben formed simultaneously with dike emplacement. For Rima Parry V, the geometry of the faults implies a dike width (~150) and depth to the top of the dike (~650) consistent with other theoretical and observational data on lunar dike geometry.

Petrycki and Wilson (1999a,b) and Petrycki et al. (2004) reported on a global survey of the properties of lunar graben and used their results to investigate the tectonic and magmatic theories proposed for their formation. To address the question of tectonic or magmatic origin, they mapped graben that showed associated volcanic deposits and features and found that 30% of the global population are directly associated with volcanic deposits (Figure 22). They further subdivided the wide range of geometries and habits observed for lunar graben into two types: 1) narrower and deeper and characterized by associated volcanic deposits and 2) wider and shallower with no associated volcanic deposits. Assuming that volcanic graben are the sites of underlying dikes, they calculated the dike geometries and volumes and found that total volumes of all of the potential graben-related dikes ranges between 32,096 and 63,219 km^3. Furthermore, Petrycki and Wilson (1999a,b) and Petrycki et al. (2004) show that while graben occur predominantly on the lunar nearside, they are unevenly distributed there, being concentrated in the northeastern and southwestern nearside quadrants (Figure 22). Of these, the majority of graben with volcanic associations occur in the northeastern quadrant. These data thus suggest that a significant number of lunar linear rilles (graben) could be underlain by magmatic dikes.

Klimczak (2014) used the dense coverage of high-resolution topographic measurements from the LRO's LOLA instrument to undertake a global survey of the long-wavelength morphology of lunar graben. Using LOLA altimetric profiles across some of the most prominent and best-preserved lunar graben, Klimczak (2014) compared their characteristics with model ground displacements for graben that form solely from faulting, and those that would be produced from faulting involving a dike at depth (Head and Wilson, 1992. 1993; Petrycki et al., 2004). His results show that many of these graben are underlain by a dike. Klimczak (2014) points out that the process of matching ground displacement models to topographic observations is the only way to detect dikes too small to be resolved in available gravity and magnetic data. This technique also

provides specific geometric information about the dikes, complementing and supplementing other approaches (Head and Wilson, 1993; Petrycki et al., 2004), and permitting quantitative assessment of magma source depths and required magma overpressures. Klimczak (2014) uses his data to conclude that the magmas that formed the documented dikes are mantle-derived and originate from >20 km depths. Furthermore, his derived dike widths exceeding 100–500 m are only plausible if a mechanically weak lunar lithosphere was under extension at the time of dike emplacement.

B. Dikes that propagate to the near-surface and intrude sills: In some cases, dikes will encounter low density zones in the crust (crater breccia zones, etc.; Figures 5b, 19) and modify their behavior accordingly, producing sills and laccoliths.

1) Floor-fractured craters: Floor-fractured craters (FFCs) (Figure 23) (Schultz, 1976b) are a class of 170 lunar impact craters characterized by anomalously shallow floors, and cut by radial, concentric, and/or polygonal fractures (Jozwiak et al., 2012). Additional features observed within FFCs are moats, ridges, and patches of mare material. Two formation mechanisms have been hypothesized for the origin of FFCs: 1) floor uplift in response to shallow magmatic intrusion and sill formation (Schultz, 1976b), and 2) floor shallowing in response to thermally driven viscous relaxation (Hall et al., 1981). To address the question of the origin of FFCs, Jozwiak et al. (2012) combined new LOLA and LROC data to characterize and categorize the entire population of FFCs and map their distribution on the Moon. They used variations in crater morphology and topography, and regional distribution, to investigate the proposed formation mechanisms. They first verified and expanded on the FFC categories recognized by Schultz (1976b) and showed that the distribution of these categories documents an evolution of crater morphology from areas adjacent to lunar impact basins to areas in the lunar highlands (Figure 23a). Jozwiak et al. (2012) proposed that this trend was supportive of formation by shallow magmatic intrusion and sill formation, as originally hypothesized by Schultz (1976b). They showed that crustal thickness determined the magnitude of magmatic driving pressure, and produced either a convex floor profile for low magnitude (Figure 23b), or a piston-like floor uplift for high

magnitude (Figure 23c). Furthermore, they showed that predictions from previous studies modeling viscous relaxation (Hall et al., 1981) are inconsistent with the observed LOLA altimetric profiles of FFCs. The Jozwiak et al. (2012) analysis favored FFC formation by shallow magmatic intrusion, with the variety of FFC morphologies being intimately linked with location and crustal thickness, crater size, and the driving pressure of the intrusion (Thorey and Michaut, 2014) (Figure 23).

Utilizing the new characterizations derived from LRO altimetry and imaging and insights into the mode of origin of FFCs as subcrater magmatic intrusion and related sill formation (Jozwiak et al., 2012), Jozwiak et al. (2015a) further assessed the geometry, modes of emplacement, associated tectonic and volcanic features, and implications for lunar history. Using the distribution and characteristics of the FFC population (Figure 23a) that showed that FFCs correlate strongly with crustal thickness and the predicted frequency distribution of overpressurization values of magmatic dikes, and that for a typical nearside lunar crustal thickness, dikes with high overpressurization values favor surface effusive eruptions, medium values favor intrusion and sill formation, and low values favor formation of solidified dikes concentrated lower in the crust. They developed a model for this process, made predictions for the morphologic, morphometric, volcanic, and geophysical consequences of the process and then compared these predictions with the population of observed floor-fractured craters. In their model, the process of magmatic intrusion and sill formation begins when a dike propagates vertically towards the surface; as the dike encounters the underdense brecciated region beneath the crater (Figure 5b), the magmatic driving pressure is insufficient to continue vertical propagation, but pressure in the stalled dike exceeds the local lithostatic pressure. The dike then begins to propagate laterally forming a sill (Thorey and Michaut, 2014) which does not propagate past the crater floor region because increased overburden pressure from the crater wall and rim crest pinch off the sill at this boundary (Figure 23d); the sill then continues to inflate, further raising and fracturing the brittle crater floor. When the intrusion diameter to intrusion depth ratio is smaller than a critical value, the intrusion assumes a laccolith shape with a domed central region (Figure 23b). When the ratio exceeds a critical value, the intrusion concentrates bending primarily at the periphery, resulting in a flat, tabular intrusion (Figure 23d).

Jozwiak et al. (2015a) predict that this process will result in concentric fractures over the region of greatest bending. This location is close to the crater wall in large, flat-floored craters, as observed in the crater Humboldt (Figure 23c), and interior to the crater over the domed floor in smaller craters, as observed in the crater Vitello (Figure 23b). On the basis of this model, a variety of volcanic features are predicted to be associated with the solidification and degassing of the intrusion, including (Figure 23d): 1) surface lava flows associated with concentric fractures (e.g., in the crater Humboldt; Figure 23c); 2) vents with no associated pyroclastic material, from the deflation of under-pressurized magmatic foam (e.g., the crater Damoiseau); and 3) vents with associated pyroclastic deposits from vulcanian eruptions of highly pressurized magmatic foam (e.g., the crater Alphonsus).

Furthermore, Jozwiak et al. (2015a) predicted that the intrusion of basaltic magma beneath the crater will contribute a positive component to the Bouguer gravity anomaly, predictions they further tested using GRAIL data (Jozwiak et al., 2015b). They observed that the positive Bouguer anomalies of individual floor-fractured craters showed spatial correlations with volcanic surface morphologies, but that the FFC positive Bouguer anomalies were spatially heterogeneous. Jozwiak et al. (2015b) interpret these observations to mean that the spatial heterogeneity observed in the Bouguer signal is due to variable degrees of magmatic gas content and degassing within the intrusions, leading to underdense portions of the intrusion (Figure 23d).

C. Dikes that propagate to the near-surface and produce local pyroclastic eruptions: Dikes that reach the near surface can produce a variety of constructs and deposits.

1) Cones: Circular, elongated and breached cones (Figure 24) have been observed locally in, and associated with, the lunar maria (Scott, 1973; Head, 1976; Schultz, 1976a) and have commonly been interpreted as cinder and spatter cones. Knowledge of the influence of the lunar environment on typical terrestrial strombolian and hawaiian eruptions (McGetchin and Head, 1973; Wilson and Head, 1981) led to the understanding that lunar cinder and spatter cone eruptions would map out to different pyroclastic cloud optical densities, cooling rates, radial accumulation rates and

pyroclastic construct shapes (Figures 5e, 7c, 9, 10). Examples of these cone-shaped features are commonly distributed in linear arrays (Figure 24a, b), are often elongated along strike (Figure 24c), and are commonly related to graben, or areas where graben or linear depressions are developed (Figures 21, 24d). For example, two cones, Isis (18.96^{o} N, 27.48^{o} E) and Osiris (18.6^{o} N, 27.6^{o} E) (Figure 24d), are separated by about 8 km from each other along a linear feature among a series of graben in southern Mare Serenitatis. Osiris is a circular cone ~1.9 km in diameter and ~90 m high, with slopes of ~7^{o}, and is in the same diameter range as the theoretical prediction for a cone produced in a lunar strombolian-type eruption (Figure 10). Similarly, Isis, ~1.5 km in diameter, ~70 m high, and with slopes ~7 ^{o}, is typical of the predicted behavior of a strombolian eruption (Figure 10), but its western wall is breached and characterized by a sinuous channel emerging from the source crater (Figure 24d), similar to breached cinder and spatter cones on Earth. Aligned between Isis and Osiris are several lower elevation and less distinct positive features interpreted to represent local spatter accumulations from material emerging from the top of the dike. In some cases cones are very elongated along the strike of the graben/fracture, interpreted to be the top of the dike (Figure 24c). Stopar et al. (2014), using high resolution LROC data, showed that basaltic cones with similar morphology and morphometry were relatively widespread in the lunar maria. They mapped a total of 180 cone occurrences, with ~100 in the Marius Hills, ~30 in the Tobias Mayer-Hortensius region, and the remainder scattered, aligned, or in groupings in the Maria Frigoris, Imbrium, Vaporum, Tranquillitatis, Nubium and Oceanus Procellarum. The cones mapped by Stopar et al. (2014) are typically less than 2 km in diameter, in the range of prediction for lunar strombolian-type eruptions (Figure 10) (Wilson and Head, 2016a).

Some of these aligned cones and positive features clearly form at the onset of a small-volume, short-lived eruption, for example, where the aligned cones occur in a highland crater without adjacent effusive maria (Figure 24a), or along a graben such as the isolated cones at Rima Parry V (Figure 21). In other cases, higher effusion rate eruptions producing flows are likely to bury or carry away near-vent pyroclastics erupted in the initial stages of the penetration of the dike to the surface (Figure 11a). Finally, spatter cones can also form along the top of the dike in the waning stages of an eruption, when

the effusion rate decreases, dike closure occurs, and spatter is favored to accumulate (Figure 14). A candidate example of this dike-closure behavior is seen in southwest Mare Imbrium where a 10 km long linear ridge is preserved along the strike of a number of vent systems (Figure 24e). No individual spatter cones or short flows are observed, but the ridge itself varies little in width and height along strike and is clearly distinguishable from nearby tectonic structures such as mare wrinkle ridges. We interpret this example to be due to late stage extrusion from the top of a dike as the dike underwent final relaxation and closure.

2) Dark Pyroclastic Ring: A large, 154 km diameter dark annular ring (Figure 25), located in the southwestern part of the Orientale Basin along the Montes Rook ring, was studied with Clementine UV-visible multispectral data (Weitz et al., 1998; Head et al., 2002). These data indicate that the dark ring consists of material similar to the pyroclastic orange glass beads, implying relatively rapid cooling times for the eruption products (Figures 5f, 9). Head et al. (2002) proposed that the dark ring is the manifestation of a pyroclastic eruption originating at a fissure vent, an elongate 7.5 km by 16 km depression, located near the center of the ring. The event producing the eruption began with a dike rapidly emplaced from subcrustal depths to within ~3–4 km of the surface; the dike stabilized and degassed over ~1.7 years to form an upper foam layer which then penetrated to the surface to cause an eruption, lasting ~1–2 weeks. The eruption is predicted to have produced a ~38 km high symmetrical spray of pyroclasts into the lunar vacuum at velocities of ~350 to ~420 m/s, and the pyroclastic material accumulated in a symmetrical ring around the vent; the deposits accumulated preferentially in a ring where material ejected at 45° reached its maximum range (Figure 5f). The paucity of pyroclastic rings of this type on the Moon can be attributed to the low probability of a dike stalling at just the right depth (~3–4 km) to create these eruption conditions. The Orientale dark ring deposit has similarities to the pyroclastic rings on the Galilean satellite Io (Head et al., 2002); in both cases the silicate pyroclasts ejected from the vent are accelerated by the gas until they become decoupled and continue on ballistic trajectories controlled only by gravity.

D. Dikes that propagate to the near-surface and produce regional pyroclastic eruptions: Pyroclastic deposits can be produced under a variety of conditions as dikes reach the near-surface and erupt.

1) Regional pyroclastic deposits: Regional dark mantle (pyroclastic) deposits have been mapped and characterized by a number of workers (Gaddis et al., 1985, 1998, 2000, 2003; Weitz et al., 1998; Gustafson et al., 2012) (Figure 26a). Weitz et al. (1998) analyzed seven regional dark mantle deposits (DMDs) using Clementine five-channel UV-visible (UVVIS) data to determine their extent and stratigraphic relationship to other geologic units. Crystallization of pyroclastic beads in each deposit was inferred based on spectral properties and used to estimate cooling rates in the volcanic plumes that emplaced the deposits. A high concentration of glasses reflects volcanic plumes that had low optical densities and high cooling rates (Figure 9), whereas crystallized beads indicate plumes with slower cooling rates due to higher optical densities. Glass:crystallized bead ratios (Figure 9b,c) can be estimated using 415/750 and 750/950 nm reflectivity values and comparison with laboratory bead spectra. The Sinus Aestuum DMD lies at one extreme (bluest color, highest 415/750; weakest glass band absorption, lowest 750/950) and the Aristarchus Plateau DMD lies at the other extreme (reddest color and strongest glass band absorption). The Taurus-Littrow, Sulpicius Gallus, Rima Bode, and Mare Vaporum DMDs lie between these two extremes due to intermediate mixtures of the crystallized beads and glasses with other local soils (Figure 9b,c). The Orientale Ring DMD on the western limb (Figure 5f, 25) is dominated by volcanic glasses and is spectrally similar to the localized DMDs found in Alphonsus crater. Weitz et al. (1999) concluded that the eruptions most likely resulted from dikes breaching the surface and producing a volcanic plume dominated by larger (greater than submillimeter) hot clasts that formed mare lavas and sinuous rilles. The small percent of clasts that formed the smaller volcanic beads were carried by the expanding gas cloud to large distances, in some cases >100 km, to produce the observed continuous regional DMDs.

Two problems exist in interpreting the pyroclastic deposits: 1) the lack of basalt samples that can be petrologically related to primitive picritic volcanic glasses and 2) the source of the gas at great depths driving the rapid eruption to the surface in explosive events (Shearer et al., 2006). Wilson and Head (2003a) proposed a model in which gas

build-up occurred in a low-pressure micro-environment near the tip of a magma-filled crack (dike) propagating rapidly from the magma source depth to the surface (Figure 26b). The gas-rich region consists of a free gas cavity overlying a foam extending vertically for up to 20 km. Eruption of the foam results in the widespread emplacement of unfractionated pyroclastic beads. According to Wilson and Head (2003a), subsequent ascent of the underlying gas-free picritic magma is unlikely to occur, perhaps accounting for the lack of sampled eruptive equivalents.

Lunar pyroclastic deposit subdivision into several modes of occurrence (Gaddis et al., 2003) suggests different modes of emplacement. Some smaller pyroclastic deposits (Figures 7, 9a, 10, 26a) have been interpreted to have erupted during strombolian/hawaiian-like activity (Weitz *et al.*, 1998) while others are linked to vulcanian activity (Figure 5g) related to dike and sill emplacement below crater floors (Head and Wilson, 1979; Jozwiak et al., 2012, 2015a,b) (Figure 26c). The largest pyroclastic deposits (Figure 26a) (Orientale dark ring, Aristarchus Plateau, Sinus Aestuum, Rima Bode, Mare Vaporum, Sulpicius Gallus, and Taurus Littrow) cover regions >1000 km^2 (Gaddis et al., 2003) and their mode of emplacement has been less clear than that of the smaller, more isolated deposits. In the case of the Aristarchus Plateau pyroclastic deposits, very high effusion rate eruptions leading to sinuous rilles (Wilson and Head, 1981) and associated pyroclastic emplacement have been implicated (see discussion in Section D2). The location of specific vents, and thus eruption styles, has been less clear for the remainder of the large deposits, partly due to burial and obscuration by post-pyroclastic deposit effusive volcanism (Head, 1974). Important evidence related to candidate modes of emplacement comes from analysis of the 154 km diameter Orientale dark ring pyroclastic deposit (Figures 5f, 25) that was shown to emanate from a linear depression interpreted to be the remains of an elongated vent at the top of a dike (Head *et al*., 2002); here a wide dike stalled just below the surface, and the low-pressure environment led to gas buildup along the top of the dike as the underlying magma convected, ultimately leading to the eruption of an Io-like pyroclastic plume to produce the dark pyroclastic ring.

Additional evidence for the association of pyroclastics with dike emplacement activity comes from the analysis of the ascent and eruption of magma (Head *et al*., 2002)

where it was shown that the low-pressure environment associated with the dike tip propagation could enhance formation of volatiles *during* dike ascent so that the dike could arrive at the surface with the top of the dike already saturated with magmatic foam, and not requiring secondary buildup as in the vulcanian (Figures 5e, 26b) (Head and Wilson, 1979) or the Orientale dark halo Ionian (Figure 5f) (Head *et al*., 2002) cases. Could this mechanism, arrival of volatile magmatic foam-laden dikes to the shallow subsurface (Wilson and Head, 2003a), perhaps combined with further shallow crustal gas formation subsequent to stalling, lead to the penetration of foams to the surface and eruption of magmatic foams to produce regional pyroclastic deposits?

The association of linear rilles (interpreted to be the surface manifestation of stress fields associated with shallow dike emplacement; Head and Wilson, 1993) with some of these deposits (e.g., Rima Bode, Sinus Aestuum; Figure 26d,e) motivated us to use new altimetry (LOLA) and camera (LROC) data to analyze the lengths, orientations and associations of linear rilles, fissures and crater chains in the Sinus Aestuum and Rima Bode regional pyroclastic deposits, and to use these data to assess whether eruptions of magmatic foam-laden dikes (Wilson and Head, 2003a) from these candidate vents could help to explain the nature and distribution of these regional pyroclastic deposits. Maps of the Sinus Aestuum and Rima Bode regions and the distribution and orientation of linear features (Wilson et al., 2013) suggest the presence of numerous linear dikes of varying orientations in and adjacent to these deposits. Mantling deposits could also cover additional linear dikes. Wilson et al. (2014) used these data to analyze the dispersal and emplacement regional pyroclastics from shallowly intruded dikes and magmatic foams.

The observed spatial relationships between linear rilles and dark mantle deposits suggest that pyroclast ranges are commonly up to 100 km. The maximum range that can be reached by a clast ejected under lunar gravity conditions implies velocities (v) up ~400 m s^{-1}. The corresponding time of flight is ~350 s, a value consistent with the cooling rates and cooling times estimated by Saal et al. (2008) for lunar volcanic glass beads. Wilson et al. (2014) assumed a larger range (200 km), and then v = 570 m s^{-1} and the time of flight is ~500 s. A reasonable way of linking the released magmatic volatile mass fraction, n, to the final gas speed at the end of complete gas expansion, v, is to assume that the gas expands adiabatically and that the pyroclasts acquire all of the gas speed. In

practice some heat is transferred from pyroclasts to gas early in the expansion, maintaining the gas temperature near-magmatic for a while and thus increasing the gas speed and hence the pyroclast range. However, pyroclasts must eventually decouple from the gas when the gas expansion becomes so large that the system enters the Knudsen regime, and this reduces the potential range. Measurements of the volatile chemistry of erupted lunar basalts allow the amounts of volatiles released during explosive eruptions to be estimated. An oxidation-reduction reaction between graphite and various metal oxides at pressures less than ~40 MPa commonly produced up to 2000 ppm CO (Nicolis and Rutherford, 2006; Rutherford and Papale, 2009). Saal et al. (2008) estimated that in addition up to 700 ppm H_2O, 325 ppm S, 15 ppm F and 0.5 ppm Cl could be released by exsolution. The amount of energy per unit mass available from the expansion of volatiles is inversely proportional to their molecular mass. As CO, with molecular mass m = 28 kg kmol^{-1}, is the dominant volatile, it is appropriate to scale the amounts of other volatiles to CO, so that their equivalent amounts become 1089 ppm H_2O, 71 ppm S_2, 11 ppm F_2 and 0.2 ppm Cl_2. The total is ~3170 ppm of equivalent m = 28 kg kmol^{-1}. This treatment then implies that the maximum speed at which pyroclasts are likely to be ejected on the Moon in purely magmatic explosive activity is ~117 m s^{-1}, corresponding to a range of 8.5 km.

This range is very much less than the observed value of ~100 km, implying greater ejection speeds and hence greater gas mass fractions in the eruption products. The amount of released gas needed to eject pyroclasts to a range of 100 km is ~10 times greater than the total available from a typical lunar magma, ~ 3000 ppm. If the range is 200 km, so that v = 566 m s^{-1}, then the value of n that is needed is ~74000 ppm, ~25 times more than is available. This seems to require secondary gas concentration processes, as in the case of the Orientale dark pyroclastic ring (Head et al., 2002) (Figures 5f, 25).

The low pressure always present in the propagating tip of a dike (Figure 26b) means that as dikes approach the lunar surface their upper tips will consist of a cavity containing gas underlain by a region where gas bubbles concentrate into a foam (Wilson and Head, 2003a). If the dike fails to break through to the surface, gas bubbles migrate up through the foam to increase the size of, and pressure in, the gas cavity. Additional foam is generated beneath the gas cavity if the dike is wide enough to allow convection to occur

because this brings magma from depth to shallow enough levels for additional pressure-dependent gas release. Head et al. (2002) showed that these processes acting in a ~500 m wide dike produced an ~25-fold gas concentration leading to an explosive eruption emplacing a ~150 km diameter circular pyroclastic deposit at Orientale (Figure 5f). Wilson et al. (2011) found that a 4-fold gas concentration led to the ~30 km radius pyroclastic deposits around Hyginus crater as gas migrated to the active vent system from the outer margins of the dike whose injection induced the associated Rima Hyginus graben; additional local gas venting caused multiple collapse craters to form along the graben.

A generic example of this process based on Head et al. (2002) and Wilson et al. (2011) would involve a 100 km long linear rille graben induced by a 300 m wide dike making the horizontal cross-sectional area of the dike 3×10^7 m^2. Magmatic foam would occupy the upper ~ 8 km of the dike where the pressure was less than 40 MPa. If the foam evolved to 80% gas volume fraction, close to the upper limit for foam stability (Jaupart and Vergniolle, 1989) then at an average pressure of 20 MPa and a magmatic temperature of 1750 K the average density of the 28 kg kmol^{-1} gas would be 40 kg m^{-3} and this would contribute a partial density of 32 kg m^{-3}. If the remaining 20% of the foam consisted of magma with density 3000 kg m^{-3} this would contribute a partial density of 600 kg m^{-3}. The gas would then represent a mass fraction of 0.0506, i.e., ~5 mass % or ~50000 ppm. Release of this foam would produce an eruption speed of 487 m s^{-1} ejecting pyroclasts to ~147 km. The mass of magma in the foam would be its partial density, 600 kg m^{-3}, multiplied by the volume of foam, 2.4×10^{11} m^3, i.e. 1.44×10^{14} kg. If this magma were deposited as pyroclasts over an area of 100 km (the rille length) × 147 km (the maximum range) with a bulk density on landing of 2000 kg m^{-3}, the resulting deposit thickness would be ~5 m. We infer that essentially all of the observed dark mantle regional pyroclastic deposits on the Moon (Figure 26a) can be explained by minor variations on this scenario.

2) Sinuous rille vents and associated pyroclastics: One of the most distinctive features on the Moon is Schröter's Valley (length ~176 km; average width 4.3 km, average depth 534 m) with Cobra Head at its source, located on the Aristarchus Plateau, and noted since the era of telescopic observations. The feature is a nested sinuous rille,

the largest on the Moon, and appears as a huge sinuous snake that is wide around its point of origin (thus the term Cobra Head). A second much smaller sinuous rille, averaging ~638 m in width and ~120 m in depth (Hurwitz et al., 2013), originates inside the Cobra Head depression, and meanders along the floor of Schröter's Valley for about 261 km, ultimately entering Oceanus Procellarum at the edge of the Aristarchus Plateau and being embayed by younger mare flows. A pyroclastic deposit covers most of the Aristarchus Plateau in the region surrounding Cobra Head and Schröter's Valley (Weitz et al., 1998). Cobra Head itself is an elongate depression ~10-12 km in diameter situated on the summit of a very irregular and roughly textured cone-shaped structure about 50-60 km in diameter and rising as much as ~1.6 km above the surrounding plains (Figure 26f). The cone-shaped feature is asymmetrical, steeper on its eastern flank, and in profile, Cobra Head appears to be centered slightly to the west of the summit with the eastern rim crest ~500-600 m higher than to the west. The flank slopes on the broad cone are in the range of 1-2^{o}. Ejecta from the much younger Aristarchus crater to the southeast modifies the eastern surface of the cone and the interior of Cobra Head, but details of the cone surface morphology can still be seen and are even better preserved to the south and west. Unlike the relatively smooth surfaces of small shield volcanoes (Figure 19a,b) or mare lava flows, the cone surface is highly irregular and dotted with small positive features, lobate irregularly shaped protrusions radiating generally outward, and local vertical relief on the scale of tens of meters. These characteristics suggest the following sequence: As with other smaller sinuous rilles, Cobra Head is the central part of a mare basalt eruption that created the broad Schröter's Valley; in this case however, the eruption deposited magmatic material for several tens of km around the source vent to form the cone. In the waning stages of the event, or in a later eruption from the same vent, a second nested sinuous rille formed on the floor of Schröter's Valley.

The structure, morphology, and scale of the cone, Cobra Head, Schröter's Valley, and the nested interior rille, the largest such features on the Moon, provide important insight into the nature of sinuous rille formation and the origin of nested rilles. We have seen the nature of lunar Hawaiian fire-fountain structures (Figure 9a), with the interior optically thick part of the expanding hemispherical plume having a very high density of particles, with inhibited heat radiation and limited cooling. These particles will reach the ground at

magmatic temperatures and coalesce into a lava pond; turbulent flow in the pond and in the lava exiting the pond will thermally erode the substrate, forming a broad depression (Cobra Head) and a large sinuous rille (Schröter's Valley). In the outer part of the hemispherical cloud, the lower optical density of the cloud maximizes heat radiation and cooling of pyroclastic particles, and a broad mantle of quenched glasses are predicted to form the regional pyroclastics surrounding the vent (Figure 9b,c). In the region intermediate between the optically very dense part of the cloud that forms the thermally eroded pond, and the low optical density part of the cloud forming widespread pyroclastic quenched beads, particles will be sufficiently separated that they form clots of material that partially cool in their exterior, but still remain molten in their cores. This intermediate environment is well-known in terrestrial cinder cones (Head and Wilson, 1989): partially molten particle accumulation forms extensive and irregular spatter deposits and local accumulations can readily produce rootless rheomorphic flows that extend down the flanks of the cone, forming irregular structures and partially cooled viscous flows. On Earth, variations in ejecta spread angle and accumulation rate lead to different morphologies (Head and Wilson, 1989). We interpret the presence and nature of the cone to be due to a situation analogous to that in the terrestrial environment: the cone, with its rough and irregular cone surface, is interpreted to represent the accumulation and flow of partially molten magma clots in the transitional zone between the inner optically very dense part of the cloud and the outer optically low density part of the cloud. Deposition of these clots throughout the course of the eruption results in the building of the broad cone, and variations in local spread angle and local accumulation rates lead to local accumulations, rough topography, and the formation of partially cooled and viscous rootless flows to yield the observed surface texture.

The dimensions of these features (Figure 26f) permit us to reconstruct the eruption conditions that characterized the formation of Schröter's Valley and Cobra Head (Garry and Bleacher, 2011). Given the dimensions of Cobra Head (diameter of ~10-12 km), we interpret the hottest part of the pond around the vent to have a radius of ~5.5 km; this represents the very optically dense part of the fountain (Figure 9a). Intermediate optical density permits descending hot clots to form the dome, out to a radius of 27.5 km. The pyroclastic glass bead distribution, represents the optically thinnest part and extends to

the radius of the outer edge of the fountain, ~200 km. From Wilson and Head (2016a) (their Equation 40) we have

$$X = (6.17\, d\, g^{1/2}\, R_f^{5/2}) / F_e \qquad (4)$$

with R_f being the maximum range of pyroclasts, 200 km, and X the distance in from the outer edge of the cloud where it is *not* optically dense, i.e. (200 - 27.5 =) 172.5 km. As outlined in Wilson and Head (2016a), g is 1.62 m s^{-2} and d is the mean pyroclast size (300 microns). With these values, and inverting the equation for the volume flux F_e, we have

$$F_e = (6.17\, d\, g^{1/2}\, R_f^{5/2}) / X \qquad (5)$$

so that F_e is equal to $[6.17 \times 300 \times 10^{-6} \times 1.62^{1/2} \times (200 \times 10^3)^{5/2}] / [172.5 \times 10^3] = 2.4 \times 10^5$ m^3 s^{-1}.

This erupted volume flux is within the range (10^4 to 10^6 m^3 s^{-1})deduced from earlier work (Wilson and Head, 1980; Head and Wilson, 1980). Using the relationships shown in Figure 13 of Wilson and Head (2016a), we compare pyroclast ranges R_{mono} in steady eruptions with the maximum ranges of the coarse and fine size fractions of a distribution in which 80% of clasts are much larger than ~1 mm and decouple rapidly from the expanding gas phase. A total volatile content of 21,000 ppm, for a mixture of coarse and fine pyroclasts, would make the fine particles extend out to ~200 km and the coarse particles are deposited out to ~17 km. In this case "fine" means that 20% of the mass has the usual average size of 300 microns and "coarse" means that 80% of the mass is much larger than 1 mm; the exact values are not critical. The main conclusion is that for a volatile content of about 20,000 ppm, fine clasts are predicted to extend out to the edge of the observed dark mantle deposit and coarse clasts accumulating out to a radius, in this case, of ~17 km. A radius of ~17 km is less than the 27.5 km radius of the cone shown in Figure 26f, but several factors could readily account for this: 1) small variations in the percentage of particles that are coarse will increase the radius of the cone; 2) a significant part of dome formation and its currently observed radius are due to accumulation of hot

clots to produce rootless flows that will flow into the surrounding regions and can readily extend the radius of the cone, creating the observed radial rough texture from rafted spatter and rootless flows (Figure 26f). One example of variations on this basic theme is to assume that the optically most dense region of the plume corresponds to the dimensions of the eroded pond (radius ~5.5 km); in this case the optically thin region is larger: X = (200 - 5.5 =) 194.5 km, but this decreases the volume flux only slightly, from 2.4×10^5 m^3 s^{-1} to 2.2×10^5 m^3 s^{-1}. Thus, this model (Figure 9a) can account for the major features in the formation of Schröter's Valley, Cobra Head, the surrounding cone and the regional pyroclastics. This example clearly provides an upper end member of the range of lunar mare basalt eruption conditions.

What is the origin of the nested sinuous rille inside Cobra Head and extending over the floor of Schröter's Valley? In a subsequent discussion we show that eruptions that continue for many months can thermally erode the vent (Figure 13), widening its radius, increasing the magma flux and favoring sinuous rille formation. In this case, the nested rilles would be a natural consequence of the later stages of this eruption, as the effusion rate decreased, Cobra Head drained and the nested rille formed. Such a process seems much more likely than the alternative of a dike forming much later and propagating to the exact same location at a point inside Schröter's Valley. Similar nested sinuous rilles occur in Rimae Prinz area (figure 30e) and are interpreted to form by the same mechanism (Wilson and Head, 1980; Head and Wilson, 1980).

E. Dikes that propagate to the surface and produce effusive eruptions: Effusive eruptions occur when a dike penetrates to the surface and any gas and foam that had accumulated at the top of the dike while it was propagating has been vented. The morphology, width and extent of the flow depends on the dike width, effusion rate, lava cooling behavior, the total volume of magma erupted, and eruption episodicity. Very wide dikes take longer to cool and centralize to the widest place in the dike (Figure 6e) and tend to produce wider flows, narrower dikes cool and centralize more rapidly (Figure 12), and dikes that just penetrate to the surface can produce rows of cones, small domes and shorter flows (Figure 24). High effusion rate eruptions with long durations can produce thermal erosion at the vent and create circular source vents and sinuous rilles (Figures 9a, 13b). Very high effusion rates of moderate duration can produce extremely

long lava flows (Figure 11). Lava flow heat loss mechanisms (conduction to the substrate, radiation) (Figure 11b) cause progressive cooling and thickening of the chilled boundary layer. Slopes are an important factor in flow length, and forward flow motion ceases when magma supply is exhausted (Figure 12a) or cooling fronts penetrate to a sufficient thickness (cooling limited flow; Figure 12b).

1) Individual small lava flows: A variety of small lobate flow fronts have been observed in the maria and in the vicinity of linear features and other volcanic edifices. Typically these features are most readily detected near the terminator at low illumination geometries, and not easily connected to their source vents (Head and Lloyd, 1971; Lloyd and Head, 1972). A wide variety of these types of flows are well illustrated in Schultz (1976a; for example Plate 87a,b).

2) Small shield volcanoes: Lunar mare domes (Figure 19a,b) have been extensively mapped on the Moon. Head and Gifford (1980) documented more than 200 of these features, classified their locations and described two modes of occurrence: 1) low, flat, generally circular structures with convex-upward shapes, slopes less than about 5^{o}, and displaying summit craters, and 2) irregular structures often adjacent to highlands regions, rarely containing summit craters. Head and Gifford (1980) concluded that the first mode of occurrence (Figure 19a,b) had very strong similarities to terrestrial small shield volcanoes (small generally circular mounds in the 3 to 17 km diameter range, and up to several hundred meters high, low flank slopes, and typically with summit pits); their characteristics placed them in the range of smaller shields in terrestrial volcanic plains (e.g., Snake River Plains) and Icelandic shields (Head and Gifford, 1980). They showed that the domes interpreted to be small shields occurred predominantly in groupings in the nearside equatorial region (Cauchy area, northeast Tranquillitatis; Hortensius area, between Kepler and Copernicus; and in the Marius Hills). The characteristics of the lunar small shields were interpreted by Head and Gifford (1980) to be related to relatively low lava effusion rates favorable to shield building eruptions, in contrast to the larger flows seen elsewhere on the Moon (e.g., Schaber, 1973). Subsequent studies with LROC and LOLA data have documented many more small shield volcanoes, particularly in the Tranquillitatis region (e.g., Tye and Head, 2013; Figure 27a,b). Additional studies have undertaken spectrophotometric and morphometric analyses of lunar domes (Wohler et al.,

2006, 2007; Lena et al., 2007, 2008). Wohler et al (2006) devised a classification scheme based on a principal component analysis of the determined spectral and morphometric features in order to estimate lava viscosity, effusion rate, duration, rise speed and feeder dike dimensions. Wohler et al. (2007) found that many domes appeared to align along trends radial to ancient impact basins, leading them to interpret the domes to have "formed along crustal fractures generated by major impact events." Using LRO LOLA data, Tye and Head (2013) documented and characterized 115 mare domes in the eastern Tranquillitatis region located on a broad rise elevated up to 2.2 km above the surrounding mare plains (Figure 27a,b). Tye and Head (2013) described the rise as consisting of multiple summits, one of which consists of multiple small shields and another characterized by a linear scarp, and termed it a "lava plateau".

On the basis of the our analysis of the generation, ascent and eruption of magma (Wilson and Head, 2016a), we interpret the small shields to have formed in a manner similar to terrestrial small shields (Head and Gifford, 1980), built from relatively low effusion rate cooling-limited (Figure 12b) eruptions. Typically on Earth, such small shields result from episodic eruptions characterized by low effusion rates due to intermittent supply of magma from the shallow mantle or a shallow magma reservoir in the crust or larger edifice. On the Moon, however, due to the great depths of the source regions, magma is unlikely to be propagated to the surface in a series of relatively small batches, as is the case in Iceland, Hawai'i, and the Snake River Plains (Greeley, 1976; Head and Gifford, 1980). Instead, dikes are likely to arrive at the surface and undergo initial peak eruption rates, followed by a decrease in effusion rate with time (Figure 14). Small shield volcanoes are most likely to be produced in this environment, with initial fissure eruptions producing broad lava flows adjacent to the linear vent (Figure 11a), and then as the eruption decreases in flux (Figure 27c), lower effusion rate flows undergo cooling and become cooling limited, ceasing their advance. Production of a succession of cooling-limited flows in the 2-8 km length range would then contribute to the construction of the small shields. Variations in shield diameter could be readily understood in the context of small variations in magma cooling and cooling-limited flow lengths, and variations in shield heights could be linked to eruption duration (Figure 27c).

The similarity of spectral properties between the small shields and the surrounding plains (e.g., Wohler et al., 2006) is consistent with this interpretation.

3) Large shield volcanoes: Shield volcanoes ("a broad volcano built up from the repeated nonexplosive eruption of basalt to form a low dome or shield, usually having a large caldera at the summit"), of the type typically seen on the Earth, Mars and Venus (de Silva and Lindsay, 2015), are conspicuously absent on the Moon. Although numerous lunar volcanic complexes are observed (Rumker Hills, Marius Hills, several localized concentrations of small shields), none display the classic radiating flows, central calderas, and flanking rift zones typical, for example, of Hawai'i on Earth (de Silva and Lindsay, 2015; Branney and Acocella, 2015; Ryan, 1988), or Olympus Mons on Mars (Carr, 1974). Shield volcanoes are intimately associated with large central mantle upwellings of magma (often hot spots or plumes) and shallow magma reservoirs in which shallow magma storage and lateral redistribution leads to flanking rift zones, associated eruptions and central, often multiple caldera collapse (Walker, 1988; Zuber and Mouginis-Mark, 1992; Wilson et al., 2001).

Head and Wilson (1991) discussed the absence of large shield volcanoes and associated calderas on the Moon and attributed it to magma transport phenomena that are typical of the Moon, in contrast to the Earth (Figure 28). They showed that melt ascending from the mantle will stall at rheological traps or at the shallower density trap at the base of the low-density lunar crust (Figure 2) and that magma will then only reach the surface along dikes propagating from these deep reservoirs. As such, vents will be very infrequent and typically characterized by large-volume eruptions. These conditions favor the formation of sinuous rilles, single long flows, and widespread flow units, rather than the type of abundant small eruptions that are fed from a shallow magma reservoir associated with neutral buoyancy zones within a central volcanic edifice, often leading to caldera collapse. Head and Wilson (1991) thus interpreted the absence of large shield volcanoes and associated calderas on the Moon to be related to the fact that shallow neutral buoyancy zones and magma reservoirs are not favored, a conclusion supported by the most recent treatment of the generation, ascent and eruption of magma on the Moon (Wilson and Head, 2016a).

In contrast to this view, Spudis et al. (2013) surveyed the lunar maria using LRO

LROC and LOLA data and on the basis of the new topography redefined many of the previously known volcanic complexes and concentration of sinuous rilles, small shields, and cones (Marius Hills, Rumker, Prinz, Kepler, Hortensius, Cauchy, Gardner and Aristarchus) as shield volcanoes, following an earlier redefinition of the Marius Hills as a shield volcano (Spudis, 1996). While acknowledging that "large central vent shield volcanoes that characterize basaltic volcanism on the other terrestrial planets appeared to be absent" on the Moon, Spudis et al., (2013) used new altimetric data to show that "almost all of these volcanic complexes on the Moon occur on large regional topographic rises in the lunar maria." While the new topographic data better define the detailed topography of these complexes, and reveal broad rises associated with those in Tranquillitatis (see also Tye and Head, 2013), we prefer the traditional definition of these groups of features as "volcanic complexes" or "lava plateaus" because: 1) most are built on pre-existing highlands topography or highland plateaus, and 2) none show evidence for centralized calderas or groups of calderas typical of the terrestrial shields described above. We discuss the eruption conditions associated with these volcanic complexes in Section F.

4) Intermediate length, moderate effusion rate, cooling-limited flows and compound flow fields: Following dike emplacement and cooling of the marginal parts of the dike, effusion dominates over the widest part of the dike and centralizes flow (Figure 6e); eruption rates can lie in the range from 10^4 to 10^6 m^3 s^{-1} (Wilson and Head, 2016a) and eruptions that are in the lower part of this range, (~$1\text{-}2 \times 10^4$ m^3 s^{-1}) are predicted to produce *cooling-limited* flows (Figure 12b) commonly less than ~10-20 km wide, ~10 m thick and less than ~200 km in length. Eruption durations are likely to be 2-3 weeks, and heat loss mechanisms cause cooling to penetrate into the flow interior (Figure 11b), slowing its forward motion; when the Grätz number (Wilson and Head, 2016a) reaches ~300, the flow will stop advancing (Figure 12b,c). At this point, lava is still being extruded from the vent and either causes inflation and breakouts in the flow levees toward the vent in the still-warmest part of the flow (Figure 12b), or forms a new, often parallel, flow from the same vent. Each new flow emerging from the same eruptive phase will be emplaced in a similar cooling environment, and produce flows with similar aspect ratios (~10-20 km wide and often 200 km in length). This process will repeat

itself until the volume of magma in the eruption is exhausted (the *supply-limited* condition) (Figure 12a).

The final result of the process is the production of a *compound flow field* (Figure 29a), a series of cooling-limited flows whose general morphology will be related to preexisting topography. On a sloped surface, a compound flow field will often appear as a set of parallel flows of broadly similar lengths and widths, while on a flat surface, flows will form complex patterns often broadly radial to the vent area. In a broad depression, such as a large crater or intercrater area (Figure 12c), supply or cooling limited flows can become ponded, inflated, and superposed, leading to vertical accretion of lava flow deposits (Whitten and Head, 2013). Multiple compound flow fields can build broad rises and plateaus, such as the Marius Hills, Rumker Hills, and the East Tranquillitatis volcanic complex (Tye and Head, 2013). How many flows might constitute a compound flow field from a single eruptive phase? From theoretical considerations (Wilson and Head, 2016a), the volume of magma predicted to represent a basaltic eruption on the Moon lies in the range of 100-1000 km^3. If a typical cooling-limited flow is ~15 km wide, ~20 m thick and ~200 km in length (~60 km^3) (Figure 29c), then these total volumes would imply that the number of cooling limited flows in a compound flow field would be in the range of ~2-15. In the case of small mare shield volcanoes, the lower effusion rates of cooling-limited flows and the radial dispersal of a few hundred cooling-limited flows from the same vent is predicted to build up a 200 m high shield over a period of 3-6 months (Figure 27c).

Lunar compound flow fields have not been specifically reported in the literature but theoretical considerations (Wilson and Head, 2016a) predict that they should be common. One reason for their lack of detection is that the extrusion of multiple parallel and overlapping flow lobes will produce a regionally relatively flat mare topographic surface that does not show the prominent lobate flow boundary scarps typical of the discrete and distinctive young Imbrium lava flows (Schaber, 1973) (Figure 29c). Secondly, following flow field emplacement, regolith formation processes will tend to average out and subdue any topographic variation remaining between adjacent flows. Finally, because compound flow fields by definition derive from the same batch of extruded magma, they are not expected to show any mineralogical or spectral reflectance variation; while they may or

may not be different from a succeeding batch of magma, there is no reason to expect significant differences that might reveal the presence of individual flows in a compound flow field. Nonetheless, spectral reflectance variations are commonly observed in the lunar maria (see Hiesinger et al., 2011, for a synthesis), and the scale of the individual subunits mapped may provide a very general estimate of the scale of compound flow fields.

New data from the LOLA instrument has provided insight into the presence and nature of lunar mare compound flow fields (Kreslavsky et al., 2016; Qiao et al., 2016a). Detrended LOLA data have revealed the presence of compound flow fields in southwest Mare Imbrium (Figure 29b) with typical flows in the range of 10-20 km wide and 100-200 km in length, implying volumes of up to ~50 km^3. Flow field morphology (Kreslavsky et al., 2016; Qiao et al., 2016a; Figure 29b) illustrates well the role of preexisting topography in their emplacement. This example suggests that compound flow fields may represent a major new insight in the mode of formation and evolution of the lunar maria. Much of the lunar mare lava may have been emplaced in relatively low effusion rate, multiple cooling-limited flows (perhaps 10-20 in any one dike arrival event) producing previously unrecognized compound flow fields.

5) Very long, very high effusion rate, supply-limited flows: The boundaries of many mare lava flows have been blurred by regolith formation but a few of the flows in Mare Imbrium (Figure 29c) are sufficiently distinct morphologically and spectrally to measure their lengths and thicknesses (Schaber, 1973; Hiesinger et al., 2002; Bugiolacchi and Guest, 2008; Campbell et al., 2009; Garry, 2014) and to estimate the topographic slopes of the subflow surfaces (Rosenburg et al., 2011; Kreslavsky et al., 2013). The largest flow length described by Schaber (1973) was 1200 km. Wilson and Head (2016a) took as values representative of such flows a thickness of 20 m and a width of 20 km; using a length of 1200 km, they calculated an emplacement time of ~69 hours and a volume flux feeding the 20 km wide flow to be 1.9×10^6 m^3 s^{-1}. Flow motion was fully turbulent. Increasing the viscosity by a factor of 10 from 1 to 10 Pa s decreases the volume flux to 1.5×10^6 m^3 s^{-1} and increases the emplacement time to ~89 hours. Even for a more conservative flow length of 600 km, all of the flows are still fully turbulent. Wilson and Head (2016a) concluded that it was very difficult to avoid the conclusion that

mare lava flows having thicknesses of at least ~10 m were emplaced in eruptions having volume eruption rates of at least 10^4 and more commonly 10^5 to 10^6 m^3 s^{-1}. Flows in the latter part of this range are very unlikely to be cooling limited and are therefore *volume limited*, erupting at 10^5 to 10^6 m^3 s^{-1} until the supply of magma to the vent was exhausted. A supply-limited origin for the young Imbrium flows is supported by their morphology (Figure 29c) which shows little evidence for the types of breakouts expected in cooling limited flows (Figure 12b). That these high-volume, very high effusion rate flows are some of the youngest lunar flows (Schaber, 1973) is consistent with the deepening of magma source regions with time and the decreasing frequency and increasing magnitude of magma volume in dikes that were able to propagate to the surface (Figure 2). The volume of magma in the above 1200 km-long flow is ~500 km^3, consistent with the ~1000 km^3 upper end of the single dike volume range predicted by Wilson and Head (2016a).

6) Sinuous rilles: Lunar sinuous rilles are enigmatic features interpreted to have formed as the result of lava thermal and mechanical erosion into highland and mare surfaces (Hulme, 1973; Carr, 1974; Williams et al., 2000; Hurwitz et al., 2012, 2013). Specific sinuous rilles have been studied in detail over the past few decades (e.g., Greeley, 1976; Greeley and Spudis, 1978), but prior to Hurwitz et al. (2013), the most recent general survey was conducted in 1969 using Lunar Orbiter IV and V photographs (Oberbeck et al., 1971). Hurwitz et al. (2013) reported on a global study that updates the catalog of sinuous rilles, using high resolution SELENE and LRO image and topography data to provide detailed observations and measurements of the rilles observed across the lunar surface (Figure 30). They found more than 200 sinuous rilles, varying in length from 2 km to 566 km (median length 33.2 km) (Figure 30b), in width from 160 m to 4.3 km (median width 480 m) (Figure 30c), in depth from 4.8 m to 534 m (median depth 49 m) (Figure 30d), and in sinuosity index from 1.02 to 2.1 (median sinuosity 1.19).

In terms of global distribution (Figure 30a), Oceanus Procellarum contains 48% of the rilles mapped in the global survey, and these rilles are typically associated with the known centers of volcanism within the Procellarum-KREEP Terrain (PKT), the Aristarchus Plateau and the Marius Hills. Hurwitz et al. (2013) also constrained the timing of the formation of lunar sinuous rilles, using the assumptions that the incised unit

represents an upper age limit and the terminal or embaying unit represents a lower age limit. Their results indicate that the distribution of ages of rille formation is highly correlated with the emplacement ages of mare units. There is no apparent temporal variation in sinuous rille development, as the abundance of sinuous rilles mirrors the abundance of mare basalts. The majority of rilles are observed to have formed between 3.0 Ga and 3.8 Ga ago during peak mare volcanism (Figure 1c), and some of the features associated with the Aristarchus Plateau may have formed as recently as 1.0 Ga to 1.5 Ga ago.

Hurwitz et al. (2013) show that the documented observations can be used to assess how sinuous rilles formed, and the relative roles of thermal and mechanical erosion. For example, the range of slopes observed for all rilles (–1.41° to 0.51°) indicates that thermal erosion is likely to be dominant during the formation of the 78% of rilles that are observed to have formed in solidified mare basalt material. In addition, mechanical erosion is likely to have been a more significant process during the formation of the 25% of observed rilles that originate in the highlands where a thicker regolith is expected to have been more easily eroded (20% of the mapped rilles crossed from the highlands into the mare).

Hurwitz et al. (2012) further assessed two erosion regimes, mechanical and thermal, for the origin of a specific occurrence of sinuous rilles, Rima Prinz, investigating the precise mechanism responsible for channel formation (constructed versus eroded origins). Measurements of channel dimensions from LOLA were used as inputs to analytical models to constrain the origin of Rima Prinz, including lava compositions, mechanical and thermal erosion rates, eruption durations, and lava volumes required to form the feature. Hurwitz et al. (2012) found that Rima Prinz (and other large sinuous rilles) could have formed as the result of thermal erosion under the weak gravity and low slope conditions characteristic of these features. In addition, they found that lava composition can have significant effects on channel formation; results for the four lava compositions considered show that komatiite-like lava will erode a similarly composed substrate most efficiently whereas a high-Ti basalt will erode a similarly composed substrate least efficiently. The Hurwitz et al. (2012) model results and LOLA topography indicate that Rima Prinz may have formed over 0.4–2.2 Earth years, depositing 50–250 km^3 of lava

over a plausible deposit area of 2450 km^2. Resulting deposit thicknesses suggest that the lava that incised Rima Prinz (Figure 30e) was most likely similar in composition to a low-Ti basalt, an observation supported by mapping.

On the basis of our analysis (Wilson and Head, 2016a), we find that the critical factor in the formation of sinuous rilles is the duration of flow; effusion rates for sinuous rille eruptions are relatively high, and many flows are indeed turbulent, but extended flow durations are essential to the onset and maintenance of thermal erosion. Centralized thermal erosion is aided by the sustained flow thermally eroding the vent and raising the magmatic flux in later stages of the eruption (Figure 13). In some cases, as in nested sinuous rilles (Figures 5, 26f, 30e), both factors appear to be important: an initial high effusion rate eruption produces a turbulent lava pond surrounding the vent and eroding an outer depression (Figure 9a) and, as the eruption wanes, the wide part of the dike becomes thermally eroded to a circular shape, focusing the flux and forming the inner depression and nested sinuous rille (Figure 13b).

F. Dikes that propagate to the surface and produce volcanic complexes: Three concentrations of volcanic effusive source vents, Marius Hills, Rumker Hills, and Aristarchus Plateau/Prinz-Harbinger occur in central Oceanus Procellarum (Whitford Stark and Head, 1977; 1980) (Figure 31). Major questions raised by their presence include: 1) Are the complexes and their vents similar to each other or different in their character?, 2) What are the major factors that account for the styles of volcanism at each complex?, 3) What accounts for the unusual concentration of volcanic source vents in these individual areas?, 4) Are these volcanic vents the source of the majority of lavas in Oceanus Procellarum?, 5) Why are the concentrations located preferentially in Oceanus Procellarum?, 6) What are the implications for the generation, ascent and eruption of magma for the individual complexes and Oceanus Procellarum?, and 7) Why do these complexes appear here, but not elsewhere in the lunar maria?

Guest (1971) and Whitford-Stark and Head (1977) showed that each of the volcanic complexes differed in terms of their styles of eruption, a distinction that has been further documented by subsequent studies (Heather et al., 2003; Campbell et al., 2009; Besse et al., 2011; Lawrence et al., 2013; Spudis et al., 2013). The smallest and northernmost complex, Rumker Hills (Figure 31a) (Scott and Eggleton, 1973; Smith, 1974), occupies

about 5000 km^2, and is characterized by about 15 lunar volcanic domes (Head and Gifford, 1977), small shield volcanoes less than about 10 km in diameter spaced irregularly across the surface. The Rumker Hills complex rises about 1100 m above the surrounding mare surface, and is flooded and embayed by younger lavas (Whitford-Stark and Head, 1977, 1980). In contrast, the much larger (~40,000 km^2) centrally located Aristarchus Plateau/Prinz-Harbinger complex (Figure 31b) centers around a pre-mare highland plateau (Aristarchus) and protruding highland crater rims and mountains (Prinz and Harbinger), is dominated by large sinuous rilles and associated dark mantling deposits, and is surrounded and embayed by younger effusive lavas. The southernmost complex, Marius Hills (Figure 31c), is comparable in size to Aristarchus Plateau/Prinz-Harbinger (~35,000 km^2), stands hundreds of meters above the surrounding plains, and is dominated by a wide variety of volcanic features and styles including shallow and steep-sloped domes and cones, widely distributed across the surface, and sinuous rilles, located predominantly on the western margin.

Although the areal density of the volcanic features in these complexes is very high by lunar standards (one feature per 103-1525 km^2 depending on the complex; Whitford-Stark and Head, 1977), it is low compared with many terrestrial cone concentrations (one per 12-42 km^2; McGetchin and Settle, 1975, Settle, 1979). No distinctive alignment of vents was found by Whitford-Stark and Head (1977), and the relatively high density of vents was attributed to 1) varied rates of magma supply (causing dike solidification and new dike formation), and/or 2) variable degrees of crustal fracturing (with more highly fractured areas permitting multiple pathways to the surface). Explanations considered by Whitford-Stark and Head (1977) for the variations in vent morphology included: 1) magma viscosity, 2) temperature, 3) composition, 4) volatile content, 5) eruption duration, 6) eruption rate, and 7) episodicity (number of eruptions from the same vent). They concluded that the morphological differences could be due to varying eruption rates (high for sinuous rilles, low for domes) and different volatile contents and viscosities (to explain the dome and cone morphologic variations).

McCauley (1967) attributed the low domes in the Marius Hills to laccolith intrusions, the steep domes and rough lava flows to magma differentiation and the consequent increased silica content, and cones to late-stage pyroclastic eruptions. In contrast,

following the interpretations of Whitford-Stark and Head (1977), more recent studies have emphasized the role of variations in eruption conditions in explaining morphologic variations (Weitz and Head, 1999; Heather et al., 2003; Besse et al., 2011; Huang et al., 2011). More recently, Lawrence et al. (2013) used comprehensive new LRO observations to confirm that the range of volcanic features (from broad low domes to steep cones) represents a range of variable eruption conditions. Using LRO LROC, LOLA, Mini-RF and Diviner data, they characterized more than 150 domes and 90 cones in the Marius Hills. They documented changes in slope along the dome flanks, and the steep dome margins were correlated with thick (30 m), steep (~16^{o}) lobate lava flows, which often contained blocks at their ends. Cones were documented to be 0.5-2 km in diameter, to range from circular to elongate to breached, and often to have clusters of boulders and layered outcrops, with cone slopes (~16^{o}) much less than the angle of repose. Blocks (not associated with impact craters) were preferentially found at the end of lava flows (relatively smaller blocks) and on the cone flanks (relatively larger blocks). Cones were often breached in the downslope direction with the breaches commonly occupied by lava flows. Building on previous remote sensing studies showing that the Marius Hills features did not differ from a basaltic composition (Weitz and Head, 1999; Heather et al., 2003; Besse et al., 2011), Lawrence et al. (2013) used Diviner data to demonstrate that the dome and cone compositions were not silicic in nature, providing additional evidence against the differentiation hypothesis of McCauley (1967). In summary, Lawrence et al. (2013) interpreted the Marius Hills to be a volcanic complex consisting of domes, flows and cones whose morphology, morphometry and mineralogy were consistent with basaltic effusions, with domes being formed by rough, blocky lava flows, with typically thinner and shorter flows interpreted to indicate relatively lower effusion rates and increased late-stage viscosity. Many flows emerge from breached cones superposed on domes, indicating to Lawrence et al. (2013) that both cones and lobate flows formed synchronously during the last stages of Marius Hills volcanism. Layers and blocks in cone walls were interpreted to represent "intermittent effusions of lava and variable eruption conditions during terminal volcanism…" Lawrence et al. (2013) conclude that variations in cone, flow and dome morphology and changes in slope

along the flanks of the domes are most plausibly explained by "changes in viscosity due to effusion rate, temperature, and or degree of crystallization."

On the basis of our analysis of the generation, ascent and eruption of mare basalts (Wilson and Head, 2016a) we concur with the general interpretations of Lawrence et al. (2013). The morphologies of individual Marius Hills domes are consistent with low effusion-rate (between 100 and 1000 m^3 s^{-1}) eruptions producing cooling-limited flows up to a few km in length that accumulate to form the dome or cone (Figure 27d). This kind of activity could represent the final stages of emptying of dikes that earlier in their eruption had erupted much larger volumes at much greater volume fluxes to form sinuous rilles (Figure 14). To explain the total volume of the Marius Hills complex, which has a volume of order 10,000 km^3, at least 10 of the largest-volume dikes predicted by Wilson and Head (2016a) to be possible sources of mare volcanism would be needed, implying the same number of individual dike emplacement events in the region, and therefore a long-lived and large diapiric source region in the mantle. Kiefer (2013) has also suggested the emplacement of a sill at relatively shallow depths below the Marius Hills. A similar range of low eruption rates characterizes the individual domes forming the Rumker Hills. However, in this case the total volume of erupted lava in the entire complex is only of order 1500-2000 km^3, requiring only one or two of the largest expected dikes to have penetrated the crust in this area, with multiple eruption sites along the fissure vent system of any one dike.

The total volume of the Aristarchus volcanics is probably at least 20,000 km^3, and the greater diversity of activity at individual eruptive centers, requiring both high and low magma volatile contents and a range of volume eruption rates, again suggests that at least 10-20 major dikes arrived in this region.

In summary, addressing the set of initial questions about the three volcanic complexes in Oceanus Procellarum: 1) We find that the complexes differ from one another in their size, topography and mode of lava emplacement as exemplified by the type and sequence of volcanic vents and edifices. 2) We interpret the major factors that account for the different characteristics at each complex to be related to different eruption styles, primarily related to flux. The Aristarchus Plateau/Rima Prinz region is dominated by sinuous rilles, indicative of very high effusion rate turbulent flows, sustained eruptions

and associated pyroclastic deposits. Several sinuous rilles also characterize the Marius Hills, but the vast majority of the eruptions (domes, cones) imply much more modest effusion rates, relatively short cooling-limited flows, and small shields with modest associated pyroclastic activity producing spatter and cinder deposits and cones. In contrast, the small shield volcanoes dominating the Rumker Hills imply low-effusion rate cooling–limited flows building up a series of small shields, perhaps several at a time above a single dike. 3) On the basis of our analysis, the observed number and density of volcanic landforms and deposits in each complex could be produced from ~10-25 dike emplacement events above a single mantle diapiric source region and is not likely to represent a particularly unusual concentration of volcanic source vents. 4) On the basis of their relatively low effusion rates, the specific sources of domes and cones in the Rumker Hills and Marius Hills are not likely to represent the source of the majority of lavas in Oceanus Procellarum. The high effusion rates and sustained eruptions associated with the Aristarchus Plateau/Rima Prinz region are more likely to be responsible for contribution to the filling of Oceanus Procellaurm in that region. 5) These concentrations may be located preferentially in Oceanus Procellarum due to the fact that they are built on pre-existing topography (Aristarchuus/Prinz and Rumker Hills) and that they are not further buried by extensive filling, as is the case in many circular mare basins. If the effects of the Procellarum-KREEP Terrain (PKT; Joliff et al., 2000) extend to deeper mantle depths, this may also be a factor. Further research needs to be undertaken to establish whether the Procellarum Volcanic Complexes owe their origin to: a) very discrete and fertile mantle source regions, perhaps linked to the PKT, b) preservation by preferentially erupting onto pre-existing highland topography, c) the presence of shallow sills, or d) their occurrence in a shallow mare basin in contrast to the thicker mare fill in many other impact basins that would have buried such complexes.

G. Non-mare volcanic domes and complexes: Relation to basaltic volcanism: The very rare occurrence on the Moon of the morphologically and spectroscopically distinctive Gruithuisen (Figure 32a) and Mairan domes in northeast Oceanus Procellarum (Head and McCord, 1978; Glotch et al., 2011; Kusuma et al., 2012; Ivanov et al., 2015) and the farside domes between the craters Belkovich and Compton (Jolliff et al., 2011; Chauhan et al., 2015) (Figure 32b) implies the localized eruption of unusually viscous,

probably rhyolitic (Wilson and Head, 2003b), magma. Wilson and Head (2016a), using the improved crustal density and thickness estimates from GRAIL, and the morphologies of the Gruithuisen and Mairan domes to infer the rheological properties, eruption rates and eruption durations, concluded that, in all cases, eruptions from reservoirs trapped at the base of the crust were thermally viable. These calculations allow us to revisit the origin of these silicic extrusions. Options include 1) basal melting of the lunar crust or the lunar magma ocean residual layer by large volumes of under-plating basalt or 2) differentiation during cooling of large-volume basaltic magma bodies, again most likely to be located at or near the crust-mantle boundary density trap (Figure 15). Wilson and Head (2016a) showed that substantial volumes, (~5000 km^3) of basaltic magma could be emplaced as intrusions at or near the base of the crust under suitable circumstances. The silicic domes are inferred to have been formed ~3.8 Ga ago (Wagner et al., 2002, 2010; Ivanov et al., 2015) concurrently with early mare history (Figure 1c), and at a time when the lithosphere was relatively thin (Figures 2, 15), and buoyant mantle plumes were more likely to pond at or near the base of the crust. The volumes of the larger domes are ~300-500 km^3 (Wilson and Head, 2003b), an order of magnitude smaller than a possible 5000 km^3 basalt intrusion, and so partial melting of overlying crust and fractional crystallization of sill magma are both viable sources of the silicic melt on thermal grounds (Wilson and Head, 2016a). If fractional crystallization were the source mechanism, concentration of volatiles into residual melt could have enriched the melt in water, perhaps by a factor of ~10 over the ~1000 ppm found in some lunar samples by Hauri et al. (2011). Eruption of silicic melt with ~10,000 ppm, i.e. ~1 mass %, of water could have ejected pyroclastic material in explosive phases of the eruptions to distances of ~30 km (Wilson and Head, 2016a,b).

Jolliff et al. (2011) used LROC images, digital terrain models and spectral data from the Diviner lunar radiometer to assess the morphology and composition of an isolated farside thorium-rich area (the Compton–Belkovich volcanic complex, CBVC). They identified a central feature of elevated topography and relatively high reflectance 25 by 35 km across that includes a series of 1-6 km diameter domes, some with steeply sloping sides (Figure 32b). Using these combined data, Jolliff et al. (2011) interpreted these features as volcanic domes formed from viscous lava enriched in silica or alkali-

feldspar, indicative of compositionally evolved, rhyolitic volcanic materials. They interpreted the Compton–Belkovich thorium anomaly as a rare occurrence of non-basaltic volcanism on the lunar farside in an area far removed from the Procellarum-KREEP terrain. In contrast to the pre-mare or syn-early mare ages of the Gruithuisen domes (Wagner et al., 2002; Ivanov et al., 2015), Jolliff et al. (2011) interpreted the Compton-Belkovich feature to be Copernican in age on the basis of the sparse number of superposed craters observed on the feature and deposit, and preservation of the small dome features. A maximum age of Lower Imbrian is established from its superposition on the Lower Imbrian-aged Compton crater.

Jolliff et al (2011) interpret the CBVC to represent (Figure 32c) a shallow, KREEP-rich alkaline-silicic intrusive and volcanic complex, inferring that the magma source must have been in the crust (but relatively deep, as no similar material was excavated by surrounding impacts), but pointing out the low probability that a high-viscosity silicic magma could rise through a significant thickness of crust. In their formation scenario, they envision that a KREEP-rich basalt magma (derived from mafic magma or a KREEP pocket deep in the crust), intruded to shallow depth and ponded in the megaregolith creating a large sill. Extended differentiation of this sill produced late stage silicic melt that erupted to the surface to form the domes and related collapse features. Thus, Jolliff et al. (2011) interpret the CBVC to represent a young intrusion (perhaps as young as Copernican) from a deep crustal source.

The presence of the CBVC and the Jolliff et al. (2011) interpretation raise a series of questions: 1) Why is the CBVC located so far from the Procellarum-KREEP terrain? 2) What petrogenetic processes can produce silicic KREEP-related terrains so late in lunar history? 3) What was the source and depth of heat that drove melting? 4) Was the parent melt similar to KREEP basalt and if so, why is it present in the crust so late in lunar history? 5) How did the melt get from a significant depth to intrude to the near-surface and erupt to the surface? Potential solutions to the age conundrum have come from further analysis of the impact crater size frequency distribution and the state of feature degradation. Shirley et al. (2012, 2013) analyzed the detailed ages and stratigraphy and concluded that the CBVC was best fit by a 3.8 Ga isochron (for craters in the range of 600 m to 2 km) and they consider this as an upper limit for the CBVC age

(Shirley et al., 2013). The CSFD plots show complex patterns at diameters less than ~800 m, however, perhaps related to 1) partial resurfacing by nearby craters, 2) the potentially unusual properties of the regolith in the CBVC pyroclastic deposits, and/or 3) CBVC volcanic resurfacing activity in the <1 Ga period. Shirley et al. (2013) conclude that the degradation state of features in the CBVC is more consistent with a >3 Ga age for volcanic activity in the complex.

In summary, we find that the most likely scenario for the formation of the Gruithuisen silicic domes and the CBVC is that they formed from differentiation of mafic magma at a depth at, or close below, the base of the crust in a period of early lunar history when shallow subcrustal reservoirs and potential sills are predicted to have formed (Figure 15). In this scenario (Wilson and Head, 2016b), magmas rising from the mantle in this early period of lunar history preferentially stalled and differentiated, concentrating radioactive elements; dense basaltic dikes were favored to intrude into the overlying crust, while less dense silicic magmas could more readily ascend to the surface and form viscous extrusions (Gruithuisen domes; Figure 32a) or explosive eruptions (Compton-Belkovich volcanic complex; Figure 32b,c). We thus favor the deep basal/subcrustal origin for the magma reservoirs for both cases (Figure 15) and do not require the shallow near-surface magma reservoir proposed by Jolliff et al. (2011, 2012) for the CBVC (Figure 32c), instead finding that the low density of the magma, assisted by a potentially high volatile (OH) content (Bhattacharya et al., 2013; Petro et al., 2013), could readily assist magma ascent, and favor effusive and explosive eruptions (Wilson et al., 2014; Wilson and Head, 2016a,b).

H. Irregular Mare Patches (IMPs): Braden et al. (2014) described Ina (Figure 33a), an enigmatic surface formation in the central nearside (18.65^{o}N, 5.30^{o}E) (Whitaker, 1972; El Baz, 1973; Strain and El Baz, 1980; Garry et al., 2012) interpreted by many to represent very young mare volcanic activity (Figure 1c) (Schultz et al., 2006, suggested ~10 Ma). Using LRO Narrow Angle Camera images, digital terrain models and Wide Angle Camera color ratios Braden et al. (2014) found a total of 70 small topographic anomalies with irregular morphologies and textures similar to Ina (Figure 33a,c). Terming these *irregular mare patches* (IMPs), Braden et al. (2014) showed that IMPs were relatively small (100 m to 5 km maximum dimensions) and characterized by sharp,

meter-scale morphology with relatively few superposed impact craters >10 m in diameter. In a manner similar to previous studies of Ina, Braden et al. (2014) showed that IMPs were characterized by two morphologically distinct types of deposit (Figure 32b): 1) a rough surface textured, topographically uneven deposit displaying a range of block densities, and 2) a smooth deposit with a relatively uniform texture and almost no blocks. Contacts between the two deposits are characterized by an abrupt change in slope, with the smooth deposits exhibiting lobate margins and steep slopes at the contact. Braden et al. (2014) assessed stratigraphic relationships for all IMPs, showing that the smooth deposits are higher in elevation, and concluding that they are generally superposed on the rough deposits. They interpreted the morphology of IMPs to be consistent with small basaltic eruptions (Figure 33b), and for the three largest irregular mare patches, crater size-frequency distributions implied ages that are younger than 100 million years. These very young ages for mare-style volcanism occur a significant time after the established cessation of mare basalt volcanism (Figure 1c). The major flux occurred ~3.9 to 3.1 billion years ago (Hiesinger et al., 2011), and volcanism occurred as recently as ~2.9 billion years ago from crystallization ages (Borg et al., 2004) and around a billion years ago from stratigraphic relationships and crater size-frequency distribution data (Schultz and Spudis, 1983; Hiesinger et al., 2011; Haruyama et al., 2009; Morota et al., 2009, 2011; Pasckert et al., 2015) (Figure 1c).

How can such young ages for extrusive mare volcanism be reconciled with the overall thermal evolution of the Moon? What style of volcanism would be expected in such late-stage eruptions? Braden et al. (2014) envision the following processes for the formation of IMPs (Figure 33b): the uneven deposits lying lower than the surrounding much older mare deposits form due to the collapse of an eruptive vent or lava lake, producing blocky deposits that are relatively less mature than the regolith; the steep marginal slopes of the smooth deposits, their often lobate margins, and their low crater density all argue that these features are extrusive basaltic volcanic material flowing out over the uneven deposits, both units being products of the late Copernican effusive basaltic eruptions. Braden et al. (2014) point out that the features that they interpret to be very recent, late-Copernican small-volume extrusions of mare basalts argue for a lunar thermal history that permits mantle melting, magma ascent and eruptions essentially to

the present time, seemingly at odds with the general picture of thermal evolution of the Moon (e.g., Ziethe et al., 2009), the increasing difficulty of magma ascent to the surface (Wilson and Head, 20156a) and the voluminous eruptions that characterize the late-stage eruptions in Mare Imbrium (Schaber, 1973) and Oceanus Procellarum (Whitford-Stark and Head, 1977, 1980; Varatharajan et al., 2014)

Qiao et al. (2016b) explored another option for the formation of IMPs that does not require Late Copernican extrusive basaltic volcanism. Braden et al. (2014) mapped the global distribution of IMPs and found that some are associated with volcanic vents, domes, and depressions, and others are associated with linear rilles and older mare deposits. Qiao et al. (2016b) interpreted examples such as Sosigines (associated with linear rilles; Figure 33c) in the context of the presence of void space left by gas and foam in the top of dikes that intrude to the near surface and solidify (Figures 5a, 6a,b). In the Qiao et al. (2016b) scenario (Figure 33d), the diffusion of this gas to the surface, and the subsequent drainage of fine-grained regolith particles into the subsurface void space, lead to the formation of the IMPs. This process can account for the rough surface (regolith drainage optimized, and new fresh boulders being constantly exposed) and the intervening steep-slope margins of the smooth units (preferential regolith drainage at the margins of the uneven terrain). Mass balance calculations (Wilson et al., 2013) find that the predicted void spaces at the top of dikes can readily account for the missing volumes of regolith material by drainage. Similar processes may operate on more ancient lava flows that were emplaced in an inflationary mode, leaving near-subsurface void spaces which later form IMP-like features due to collapse and drainage of regolith (Garry et al., 2012; Qiao et al., 2016b). Others, such as the Ina feature, which occurs as the summit pit crater on a small lava shield (Figure 32a), are consistent with a two component origin as a drained lava lake (forming the mounds as kipukas, and the floor as a void-rich subsided lava lake crust) followed by differential development of regolith (normal development on the mounds, and abnormal development on the floor as seismic sieving causes small regolith particles to preferentially drain into the underlying voids, maintaining roughness and optical immaturity, and exposing boulders) (Qiao et al., 2016c). In all these cases, the basic mare deposits, and features with which the irregular mare patches are associated, date from the period of major mare volcanism, primarily in the Imbrian

period, and the IMP features themselves form passively by regolith drainage during the ensuing history (Qiao et al., 2016b,c).

IV. Lunar Mare Magmatism (Plutonism and Volcanism): Synthesis and Conclusions:

On the basis of our analysis of theoretical aspects of lunar mare basalt magma generation, ascent, intrusion and eruption (Wilson and Head, 2016a), and our assessment of the processes of intrusion and eruption as recorded in the geologic record (Figure 1), we now turn to a synthesis of predictions, observations and summary themes.

a) Mare basalt magma generation: Mare basalt magmas are generated in the mantle upon heating of sufficient intensity and duration to generate partial melts that can undergo collection into magma source regions (Figures 2, 4). The nature, distribution and duration of mare basalt magma heat sources are currently poorly understood (Shearer et al., 2006) but the consensus is that mare basalts were largely derived from the remelting of the solidified products of a deep magma ocean by relatively small degrees of partial melting (<10%), and that the mare basalt mantle source region was heterogeneous (e.g., Grove and Krawczynski, 2009; Hallis et al., 2014).

b) Diapiric rise of mare basalt sources: In early lunar history, mantle chemical and thermal variations produce density contrasts relative to the bulk mantle and cause larger buoyant regions to rise to produce melt-rich diapirs (Figure 2).

c) The role of chemical and mechanical traps in magma ascent and trapping: Depending on the stage in lunar thermal evolution (Figure 1c), buoyant melt-rich diapirs may rise to the base of the anorthositic crustal density trap (when the crust is thicker than the elastic lithosphere), or later in history to the base of the lithospheric rheological trap (when the thickening lithosphere exceeds the thickness of the crust) (Figures 2,3).

d) Melt segregation: As the diapiric rise of a basaltic magma source region slows and stalls, residual buoyancy, and continued production and arrival of diapiric material, enhances melt volume and overpressurizes the source regions (Figures 3,4).

f) Dike initiation processes: Increased overpressurization produces sufficient stress to cause brittle deformation of the elastic part of the overlying lithosphere and a

magma filled crack (a dike) initiates and propagates toward the surface as a convex upward, blade-shaped structure (Figure 4).

e) Volumes of magma generated: Dike size is dependent on the volume of magma released from a diapiric source region in a single event, less than a few percent of the source region volume, and for isolated dikes is likely to lie in the range 10^2 km^3 to 10^3 km^3. These volumes correspond to dikes with widths of 40-100 m and both vertical and horizontal extents of 60-100 km, ensuring that they can erupt through the nearside crust of the Moon but not through the thicker farside crust. Smaller volume isolated dikes will form intrusions in the crust centered on the density trap at the base of the crus (Figure 4).

e) Magma ascent: Continuous dikes and isolated dikes: A variety of factors can cause dikes to stall and solidify, becoming intrusions in the mantle and crust (Figure 5a); larger batches of magma released in a dike emplacement event are favored to reach the surface. Shallower magma sources may produce dikes that are continuous from the source region to the surface. Deeper source regions may propagate dikes that detach from the source region and ascend as discrete penny-shaped structures toward the surface. Shallow density traps, such as the low-density anorthositic crust, may further inhibit the rise of isolated dikes (Figure 2).

g) The role of global thermal evolution in magma ascent and eruption: As the Moon cools with time, the lithosphere thickens, source regions become less abundant and rheological traps become increasingly deep, and the state of stress in the lithosphere becomes increasingly contractional, inhibiting dike emplacement and surface eruptions (Figures 1,2).

h) The role of shallow preexisting crustal/lithospheric structure in dike propagation and magma ascent: Dike initiation occurs in magma source regions at great depth and the initial orientation of dikes is not influenced by surface or shallow crustal structure. As the dike propagates toward the surface, shallow crustal stress fields, related to surface topography or lithospheric loads, can influence its orientation, potentially causing rotation and reorientation or the development of an en echelon structure. Brecciated zones are unlikely to have any effects below the crack-closure depth (~25 km), but appear to encourage sill formation in sub-crater breccia zones in the uppermost crust. Impact basin radial and concentric structures are in themselves unlikely

to control the location and orientation of dikes due to the much deeper location of dike initiation, but mascons and topography-induced regional stress fields may influence the near-surface orientation of dikes during the final stages of their ascent from the mantle.

i) Factors in magma intrusion versus eruption: In contrast to dike volumes and propagation velocities in terrestrial mid-ocean ridge tectonic environments (Head et al., 1996), lunar dike propagation velocities are typically sufficiently high that shallow sill formation is not favored. In some cases, such as floor-fractured craters, low-density sub-crater floor breccia zones may influence rising dikes with relatively lower overpressures to form laccoliths (smaller craters) and sills (larger craters) (Figure 5b). The total predicted volume of magma in dikes, and the low predicted eruption frequency, does not favor the formation of larger regional-scale sills, such as might underlie regional volcanic complexes.

j) Dike emplacement physical and chemical processes: The predicted rates of magma rise and typical dike widths suggest that motion in the dikes will be turbulent rather than laminar. Following initial chilling of magma onto the dike walls, efficient heat transfer caused by turbulent flow can cause thermal erosion of the chill layer and then the mantle/crust country rock with potential mineralogic alteration of the anorthositic crust. Gross and Treiman (2011) interpreted pink spinel anorthosite (PSA; Pieters et al., 2011) as being due to the interaction of basaltic melts and the anorthositic lunar crust (for example, during dike emplacement), but experiments by Prissel et al. (2012) indicate that PSA spinel compositions are best explained via the interaction between Mg-suite parental melts and anorthositic crust. Indeed, earlier in lunar history (Figure 1c), when the thermal structure was different and magma composition and buoyancy of Mg-suite and early mare precursor magmas were different, intrusion and sills may have been more significant (Prissel et al., 2014, 2015; Sori et al., 2013).

k) The role of volatile generation and behavior in ascent and eruption: The Moon has traditionally been thought of as volatile-depleted, but the presence of pyroclastic deposits and the availability of improved analytical techniques revealing the presence magmatic volatiles in pyroclastic glasses has changed this picture. First, it has been shown that the low pressure environment in propagating dike crack-tips can cause gas formation at great depths during the dike ascent (Wilson and Head, 2003a), both by

exsolution of previously undetected volatiles (Saal et al., 2008; Wetzel et al., 2015) and carbon-metal oxide smelting reactions (Nicholis and Rutherford, 2009). Both processes can continue to produce significant shallow degassing and pyroclastic activity once an open pathway to the surface is established (Rutherford et al., 2015). Together, these factors strongly suggest that most magmas that reach the surface will be characterized by an initial vigorous phase of pyroclastic activity, and that pyroclastic activity should be common over a range of eruption geometries.

l) Predicted and observed surface deposits: Intruded dikes: Dikes that intrude into the deeper crust could produce magnetic anomalies if emplaced in the presence of a lunar magnetic field. Dikes emplaced onto the shallow crust may stall and produce crater chains due to active and passive gas venting, or if sufficiently shallow, may create a near-surface stress field to form linear and arcuate graben, often with pyroclastic and small-scale effusive eruptions.

m) Predicted and observed surface deposits: Explosive eruptions: Dikes penetrating to the surface can produce a wide range of explosive eruption types whose manifestations are modulated by lunar environmental conditions (Figures 5d-g, 9, 10)): terrestrial strombolian-style eruptions map to cinder/spatter cone-like constructs; hawaiian-style eruptions map to broad flat pyroclastic blankets; gas-rich ultraplinian-like venting cause extremely widespread dispersal of foam droplets (perhaps the source of isolated glass beads in the regolith from many sites; Delano, 1986); vulcanian-like eruptions caused by solidification of magma in the dike tip, buildup of gas pressure and explosive disruption, can form dark halo craters with mixed country rock (Head and Wilson, 1979); ionian-like eruptions can be caused by artificial gas build up in wide dikes, eruption and formation of a dark pyroclastic ring (Head et al., 2003); multiple eruptions from gas-rich fissures can form regional dark mantle deposits (Wilson et al., 2014); and long duration, relatively high effusion rate eruptions accompanied by continuing pyroclastic activity cause a central thermally eroded lava pond and channel, a broader pyroclastic ‘spatter’ edifice, an even broader pyroclastic glass deposit and, if the eruption last sufficiently long, an associated inner thermally eroded vent and sinuous rille channel.

n) Predicted deposits: Gas venting and polar accumulation: Gas venting during pyroclastic eruptions in the mare basalt eruption phase is a source for volatiles potentially cold-trapped in permanently shadowed polar regions. If volatiles (e.g. water) make up 100 ppm (0.01 mass %) of the estimated 10^7 km^3 of erupted lunar mare basalts (Head and Wilson, 1992), and if 1 % of this survived escape from the Moon (the speed of water molecules released at magmatic temperatures is ~1.7 km s^{-1}, ~70% of lunar escape velocity) then this would supply a global equivalent layer of about 0.6 mm if it condensed onto the surface and a layer 100 m thick on the floor (~20 km diameter) of a typical permanently shadowed crater such as Shackleton (Zuber et al., 2012). Shackleton's age is ~3.6 Ga, coincident with the middle of the peak period of mare emplacement, and thus volatiles from mare sources are likely to be even more abundant in older craters (Tye et al., 2015).

o) Predicted and observed surface deposits: Effusive eruptions: Deep magma sources and large dike volumes lead to predictions of a variety of effusive eruption styles that often differ from those on Earth (Figures 11-13). Lunar effusive eruptions are modulated by effusion rates, eruption durations, cooling and supply limitations to flow length, and pre-existing topography. Relatively low effusion rate, cooling-limited flows on relatively flat surfaces lead to small shield volcanoes; higher effusion rate, cooling-limited flows lead to compound flow fields, only recently recognized on the Moon (Kreslavsky et al., 2016; Qiao et al., 2016a); even higher effusion rate, long duration flows lead to thermal erosion of the vent, effusion rate enhancement, and thermal erosion of the substrate to produce sinuous rilles; extremely high effusion rates on slopes lead to rapid emplacement of volume-limited flows with lengths of many hundreds of kilometers; high effusion rates can lead to widespread flow inflation, and pre-existing topography (e.g., crater floors) can have a major influence on lava accumulation, cooling and potential fractionation.

p) Time history of a typical eruption: In virtually any eruption, as the dike reaches the surface it is at maximum overpressure and opens along a linear fracture produced by the convex upward dike penetrating the crust (Figure 6b). In a magma containing volatiles, initial venting of the free gas at the top of the dike leads to an ultraplinian eruption (Figures 5d,e) followed rapidly by a "lunar plinian" eruption as the

underlying foam collapses and its magmatic gas expands). This produces a widespread and thin pyroclastic glass/quenched bead deposit tens of kilometers in radius). Within minutes, the next phase involves the very high effusion rate outpouring of lava from the elongated vent, kilometers long and immediately responding to local slopes to form a flow (Figure 11a). Eruptions venting into a crater will tend to fill it; eruptions on a slope will form a flow, and those on a flat lava plain will respond to the subtleties of earlier volcanic flow topography. Continued volatile production (degassing/smelting reaction) in the shallow crust as new magma rapidly arrives means that the effusive eruption will be accompanied by lunar hawaiian-style activity, with a wide spread-angle fountain (no atmosphere), wide dispersal of pyroclasts ($1/6^{th}$ gravity), and a greater opacity (smaller pyroclasts) than terrestrial fountains (Head and Wilson, 1981). As the eruption continues, overpressure decreases, and effusion rate declines, but is centralized on the widest place in the dike, and eruption continues at these rates until magma is depleted from the source (volume-limited flows) (Figure 12a,b). At this point, likely to be rather abrupt, the flow stops advancing and progressively cools. If the flow is cooling-limited (lower effusion rate), then when the cooling limited length is reached, the magma will break out in the proximal part of the flow or at the vent along the wide place in the dike next to the cooling-limited flow, producing a compound flow field (Figure 29a). If the eruption goes on for a long time, the vent becomes circularized by thermal erosion of its walls, the surface lava flow narrows, and thermal erosion sets in at the base of the dominant flow unit to produce a sinuous rille (Figure 13).

q) Fate of magma in the dike at end of eruption: Eruptions end when the stress holding the dike open reaches zero (Figure 14). In the case of an eruption fed through a continuous dike connected to a large shallow magma reservoir (Figure 2) this is the excess pressure that had accumulated in the reservoir to initiate the eruption modified by the state of stress in the lithosphere. In the case of an isolated dike that has pinched off from a diapiric source deep in the mantle and is coming to rest centered on the crust-mantle interface, the excess pressure in the dike when it intersects the surface will be that inherited from its formation. This excess pressure will decay rapidly as magma is erupted from the dike. The eruption will end when the external lithostatic stress trying to close the dike is just balanced by the internal

pressure at the level of neutral buoyancy, and that internal pressure will be the combination of the effects of the negative buoyancy of the magma in the upper part of the dike located in the crust and the positive buoyancy of the magma in the lower part of the dike located in the mantle. Early in the period of mare volcanism the lithospheric stress was extensional and up to ~20 MPa (Solomon and Head, 1908). Dikes erupting from relatively shallow sources during this period will have locally relaxed the extensional stress as they opened and after decay of the excess source pressure will be kept open to widths of at least several tens of meters. Late in the period of mare volcanism (Figure 1c) the lithospheric stress was compressional, also up to ~20 MPa (Solomon and Head, 1980). The internal pressure in dikes from deep sources coming to rest centered on the crust mantle will be up to ~30 MPa (Wilson and Head, 2016a), leaving ~10 MPa net pressure to maintain dikes open to, on average, about half of the typical width of early-emplaced dikes. In all cases, even if the final net stress acting to keep a dike open is very small, there will be some finite thickness due to magma that has already chilled against the dike wall.

r) Nighttime eruptions: The extreme difference between daytime and nighttime surface temperatures and the long duration of both could cause significant variations in lava flow cooling rates (Figure 11b) and small perturbations to boundary zones in pyroclastic eruption clouds but many eruptions are likely to last considerably longer than two weeks so this effect will probably be averaged out and not detectable with current methods.

s) Implications for dike density in the lunar crust: The frequency distribution of dike emplacement events implies that a significant number of dikes should be intruded into the lunar crust, and may thus have an effect on overall crustal density. Earlier estimates of the density of dikes (Head and Wilson, 1992) can be updated by our current treatment: dike emplacement and solidification of a considerable volume of magma in the crust are favored early in lunar mare history due to shallower source region depths and the extensional state of stress in the lithosphere. In later lunar history, the net contractional state of stress implies that whatever dikes are intruded into the crust will be systematically thinner and probably less voluminous.

t) Dike orientation: Although some instances occur of aligned graben and fissures, there are also many cases where the strikes of intersecting or nearby graben are at high angles or even orthogonal to each other. This is not surprising if these features are formed by dikes originating at great depths. As long as a dike is nucleated from a diapiric partial melt region below the base of the elastic lithosphere, the horizontal stresses controlling its initial orientation are likely to be isotropic and the orientation will therefore be random. If a second dike leaves the same diapiric source, the emplacement of the first dike may have modified the stress distribution in such a way that the second dike is initiated in a vertical plane orthogonal, or at least at a large angle, to the first. Multiple events will likely lead to a distribution of orientations that are scattered over a wide range of orientations. It is only as dikes penetrate into the elastic lithosphere, where differential stresses can be maintained, that modifications to their original orientations, such as the production of *en echelon* patterns, can occur.

u) What is the role of impact craters and basins in initiating mare basalt eruptions?: Impact basins, with their large diameters, significant depths of excavation, and associated extensive mare fill deposits, have long been considered a potential factor in mare basalt generation, ascent and eruption (Elkins-Tanton and Hager, 2005). Analyses have shown, however, that the low pressure gradient on the Moon means that pressure-release mantle melting during basin collapse is not likely to be important and that resulting basin structure is too shallow to have a significant effect on ascent and eruption of magma (Ivanov and Melosh, 2003)). Furthermore, Whitten et al. (2011) analyzed ages of mare basalt deposits in the young 920 km Orientale Basin and found that the distribution of mare deposit ages spanned the total range of known mare basalt emplacement, and that there was little evidence for significant mare deposits formed coincident with the Orientale impact event. Elkins-Tanton et al. (2004) suggested that basin collapse might induce preferential convection below the basin floor, resulting in mare volcanism delayed by several hundred million years, but no specific surge was detected in the Orientale mare deposits by Whitten et al. (2011).

v) Very recent lunar mare volcanism?: Braden et al. (2014) mapped a total of 70 *irregular mare patches* (IMPs), small topographic mare-related anomalies with irregular morphologies and textures, and interpreted IMPs to be due to small recent

basaltic eruptions (younger than 100 million years for the three largest IMPs). We find that some IMPs, such as Ina and Sosigenes, do not require Late Copernican extrusive basaltic volcanism (Figure 1c), but instead, the presence of void space left by gas and foam in the top of dikes, and the subsequent drainage of fine-grained regolith particles into the subsurface void space, could lead to the formation of some IMPs (Figure 33d) (Qiao et al. , 2016b). For Ina (a summit pit crater on a small lava shield), Qiao et al. (2016c) envisioned a two component origin as a drained lava lake (forming the mounds as kipukas, and the floor as a void-rich subsided lava lake crust) followed by differential development of regolith (normal development on the mounds, and abnormal development on the floor as seismic sieving causes small regolith particles to preferentially drain into the underlying voids, maintaining roughness and optical immaturity, and exposing boulders). These processes are associated with the initial emplacement conditions and do not require extrusive volcanism in the last few millions of years (Qiao et al., 2016b,c).

w) Major factors in the history of mare volcanism: The surface geologic record of mare volcanism spans several billion years and the rapidly decreasing integrated flux of mare basalt is a result of continued cooling of the Moon, thickening of the lithosphere, and an increasingly contractional global state of stress progressively inhibiting generation, ascent and eruption of basaltic magma. The nearside-farside asymmetry in the distribution of mare basalt deposits is most plausibly explained by crustal thickness differences; intrusion is favored on the thicker farside crust and extrusion is favored on the thinner nearside crust. Regional and global thermal and broad geochemical anomalies (the Procellarum-KREEP Terrain) are additional factors. Testimony to a laterally and vertically heterogeneous mantle source region is amply seen in the differences in mare basalt titanium content as a function of space and time.

This improved paradigm for the generation, ascent, intrusion and eruption of basaltic magma provides the basis for the broader interpretation of the lunar volcanic record in terms of variations in eruption conditions in space and time, and their relation to mantle heterogeneity (Grove and Krawczynski, 2009) and a more detailed understanding of lunar thermal evolution.

Acknowledgements: We gratefully acknowledge the leadership and dedication displayed by members of the LRO mission and the Principal Investigators, staff and students involved in data acquisition and analysis for the LRO instruments. We further gratefully acknowledge funding to Co-Investigator JWH for participation in the LOLA Experiment Team (Grants NNX11AK29G and NNX13AO77G). Much of the synthesis work for this contribution was enabled by participation in the NASA Solar System Exploration Research Virtual Institute, through the SEEED (SSERVI Evolution and Environment of Exploration Destinations) cooperative agreement number NNA14AB01A at Brown University. Thanks are extended for Anne Côté for help in figure drafting and Lauren Jozwiak, Jay Dickson and Le Qiao for assistance in image figure preparation.

References:

Besse, S., Sunshine, J.M., Staid, M.I., Petro, N.E., Boardman, J.W., Green, R.O., Head III, J.W., Isaacson, P.J., Mustard, J.F., Pieters, C.M., 2011. Compositional variability of the Marius Hills volcanic complex from the Moon Mineralogy Mapper (M3). J. Geophys. Res. 116, E00G13, doi:10.1029/2010JE003725.

Bhattacharya, S., Saran, S., Dagar, A., Chauhan, P., Chauhan, M., Ajai, Kumar, A.S.K., 2013. Endogenic water on the Moon associated with non-mare silicic volcanism: Implications for hydrated lunar interior. Current Sci. 105, 685-691.

Bottke Jr., W.F., Richardson, D.C., Love, S.G., 1997. Can tidal disruption of asteroids make crater chains on the Earth and Moon? Icarus 126, 470-474.

Braden, S.E., Stopar, J.D., Robinson, M.S., Lawrence, S J., van der Bogert, C.H., Hiesinger, H., 2014. Evidence for basaltic volcanism on the Moon within the past 100 million years. Nature Geosci. 7, 787-791.

Branney, M., Acocella, V., 2015. Calderas. In: *Encyclopedia of Volcanoes*, H. Sigurdsson, Ed. in Chief, Academic Press, San Diego, 299-319.

Bugiolacchi, R., Guest, J.E., 2008. Compositional and temporal investigation of exposed lunar basalts in the Mare Imbrium region. Icarus 197, 1–18.

Campbell, B.A., Hawke, B.R., Campbell, D.B., 2009. Surface morphology of domes in the Marius Hills and Mons Rümker regions of the Moon from Earth-based radar

data, J. Geophys. Res. 114, E01001, doi: 10.1029/2008JE003253.

Carr, M.H., 1974. Tectonism aqnd volcanism of the Tharsis region of Mars. J. Geophys. Res. 79, 3943-3949.

Carter, I.M., Campbell, B.A., Hawke, B.R., Campbell, D.B., Nolan, M.C., 2009. Radar remote sensing of pyroclstic deposits in the southern Mare Serenitatis and Mare Vaporum regions of the Moon. J. Geophys. Res. 114, E11004, doi: 10.1029/2009JE003406.

Chauhan, M., Bhattacharya, S., Saran, S., Chauhan, P., Dagar, A., 2015. Compton-Belkovich volcanic complex (CBVC): An ash flow caldera on the Moon. Icarus 253, 115-129.

Crotts, A.P.S., 2008. Lunar outgassing, transient phenomena, and the return to the Moon:. I. Existing data. The Astrophysical Journal 687, 692-705.

de Silva, S., Lindsay, J.M., 2015. Primary volcanic landforms. In: *Encyclopedia of Volcanoes*, H. Sigurdsson, Ed. in Chief, Academic Press, San Diego, 273-297.

Delano, J.W., 1986. Pristine lunar glasses. J. Geophys. Res. 91, D201-D215.

Elkins-Tanton, L.T., Burgess, S., Yin, Q.-Z., 2011. The lunar magma ocean: Reconciling the solidification process with lunar petrology and geochronology. Earth Planet. Sci. Lett. 304, 326-336, doi: 10.1016/j.epsl.201.02.004.

Eppler, D., Heiken, G., 1975. Lunar crater chains of non-impact origin. *Proc. Lunar Sci. Conf. 6th*, 2571-2583.

Ernst, R.E., Buchan, K.L., West, T.D., Palmer H.C., 1996. Diabase (dolerite) dyke swarms of the world, first edition, Open File Rep. 3241, scale 1:35,000,000, Geol. Surv. of Can., Ottawa.

Fogel, R., Rutherford, M., 1995. Magmatic volatiles in primitive lunar glasses, I, FTIR and EPMA analyses of Apollo 15 green and yellow glasses and revision of the volatile-assisted fire-fountain theory. Geochim. Cosmochim. Acta 59, 201-215.

Foing, B.H., Racca, G.D., Marini, A., Evrard, E., Stagnaro, L., Almeida, M., Koschny, D., Frew, D., Zender, J., Heather, J., Grande, M., Huovelin, J., Keller, H.U., Nathues, A., Josset, J.L., Malkki, A., Schmidt, W., Noci, G., Birkl, R., Iess, L., Sodnik, Z., McManamon, P., 2006. SMART-1 mission to the Moon: Status, first results and goals. Advances in Space Research 37, 6-13.

Gaddis L.R., Pieters, C.M., Hawke, B.R., 1985. Remote sensing of lunar pyroclastic mantling deposits. Icarus 61, 461-489.

Gaddis, L., Rosanova, C., Hare, T,. Hawke, B.R., Coombs, C., Robinson, M.S., 1998. Small Lunar Pyroclastic Deposits: A new global perspective. Lunar Planet. Sci. 29, abstract 1710.

Gaddis, L.R., Hawke, B.R., Robinson, M.S., Coombs, C., 2000. Compositional analyses of small lunar pyroclastic deposits using Clementine multispectral data. J. Geophys. Res. 105, 4245-4262.

Gaddis, L.R., Staid, M.I., Tyburczy, J.A., Hawke, B.R., Petro, N.E., 2003. Compositional analyses of lunar pyroclastic deposits. Icarus 161, 262-280.

Garry, W.B., Robinson, M.S., Zimbelman, J.R., Bleacher, J.E., Hawke, B.R., Crumpler, L.S., Braden, S.E., Sato, H., 2012. The origin of Ina: Evidence for inflated lava flows on the Moon. J. Geophys. Res. 117, E00H31, doi: 10.1029/2011JE003981.

Garry, W.B., 2014. The Mare Imbrium flow field: Regional geologic context of the Chang'E 3 landing site. Lunar Planet. Sci. Conf. 45, abstract 2169.

Garry, W.B., Bleacher, J.E., 2011. Emplacement scenarios for Vallis Schroteri Artistarchus Plateau the Moon. In: Recent Advances and Current Research Issues in Lunar Stratigraphy, Ambrose, W.A., Williams, D.A., eds., Geological Society of America Special Paper 477, p. 77-93, doi: 10.1130/2011.2477(03).

Glotch, T.D., Hagerty, J.J., Lucey, P.G., Hawke, B.R., Giguere, T.A., Arnold, J.A., Williams, J.P., Jolliff, B.L., Paige, D.A., 2011. The Mairan domes: Silicic volcanic constructs on the Moon. Geophys. Res. Lett. 38, L21204, doi: 10.1029/2011GL049548.

Golombek, M.P., 1979. Structural analysis of lunar grabens and the shallow crustal structure of the Moon. J. Geophys. Res. 84, 4657-4666.

Goswami, J. N., Annadurai, M., 2009. Chandrayaan-1: India's first planetary mission to the Moon. Lunar Planet. Sci. Conf. 40, abstract 2571.

Greeley, R., 1976. Modes of emplacement of basalt terrains and an analysis of mare volcanism in in the Orientale Basin. Proc. Lunar Sci. Conf 7, 2747-2759.

Greeley, R., Spudis, P.D., 1978. Mare volcanism in the Herigonius region of the Moon. Lunar Planet. Sci. Conf. Proc. 9, 3333-3349.

Gross, J., Treiman, A.H., 2011. Unique spinel-rich lithology in lunar meteorite ALHA 81005: Origin and possible connection to M3 observations of the farside highlands. J. Geophys. Res. 116, E10009, doi:10.1029/2011JE003858.

Grove, T.L., Krawczynski, M.J., 2009. Lunar mare volcanism: Where did the magmas come from? Elements 5, 29-34, doi: 10.2113/gselements.5.1.29.

Guest, J. E., 1971. Centres of igneous activity in the maria. In: *Geology and Physics of the Moon*, edited by G. Fielder, 41-53, Elsevier, New York.

Gustafson, J.O., Bell III, J.F., Gaddis, L.R., Hawke, B.R., Giguere, T.A., 2012. Characterization of previously unidentified lunar pyroclastic deposits using Lunar Reconnaissance Orbiter Camera data. J. Geophys. Res. 117, E00H25, doi: 10.1029/2011JE003893.

Hall, J.L., Solomon, S.C., Head, J.W., 1981. Lunar floor-fractured craters: Evidence for viscous relaxation of crater topography. J. Geophys. Res. 86, 9537-9552, 1981.

Hallis, L.J., Anand, M., Strekopytov, S., 2014. Trace-element modeling of mare basalt parental melts: Implications for a hetroigeneous lunar mantle. Geochimica et Cosmochimica Acta 134, 289-316, doi: 10.1016/j.gca.2014.01.012.

Harris, A.J.L., Rowland, S.K., 2015. Lava flows and rheology. In: The Encyclopedia of Volcanoes, Elsevier Inc., 321-342.

Haruyama, J., Hioki, K., Shirao, M., Morota, T., Hiesinger, H., van der Bogert, C.H., Miyamoto, H., Iwasaki, A., Yokota, Y., Ohtake, H., Matsunaga, T., Hara, S., Nakanotani, S., Pieters, C.M., 2009. Possible lunar lava tube skylight observed by SELENE cameras. Geophys. Res. Lett. 36, L21206, doi:10.1029/2009GL040635.

Haruyama, J., K. Hioki, M. Shirao, T. Morota, H. Hiesinger, C. H. van der Bogert, H. Miyamoto, A. Iwasaki, Y. Yokota, H. Ohtake, T. Matsunaga, S. Hara, S. Nakanotani, and C. M. Pieters (2009),Possible lunar lava tube skylight observed by SELENE cameras, Geophys. Res. Lett., 36, L21206, doi:10.1029/2009GL040635.

Hauri, E.H., Weinreich, T., Saal, A.E., Rutherford, M.C., Van Orman, J.A., 2011. High pre-eruptive water contents preserved in lunar melt inclusions. Science 333, 213–215.

Hauri, E.H., Saal, A.E., Rutherford, M.J., Van Orman, J.A., 2015. Water in the Moon's interior: Truth and consequences. Earth Planet. Sci. Lett. 409, 252-264.

Hawke, B.R., Coombs, C.R., 1987. Remote sensing studies of the Rima Hyginus region of the Moon. Lunar Planet. Sci. 18, 407-408.

Hawke, B.R., Coombs, C.R., Gaddis, L.R., Lucey, P.G., Owensby, P.D., 1989. Remote sensing and geologic studies of localized dark mantle deposits on the Moon. Proc. Lunar Planet. Sci. Conf. 19, 255-268.

Head, J.W., 1974. Lunar dark-mantle deposits: Possible clues to the distribution of early mare deposits. Proc. Lunar Sci. Conf. 5, 207-222.

Head, J.W., 1976. Lunar volcanism in space and time. Reviews of Geophysics and Space Physics 14, 265-300.

Head, J.W., 1999. Surfaces and interiors of the terrestrial planets. In: The New Solar System, Beaty, J. K., Petersen, C. C., and Chaikin, A. (eds.), Cambridge University Press, p. 157-173.

Head, J.W., 2001. Lunar and planetary perspectives on the geological history of the Earth. Earth Moon Planets 85-86, 153-177.

Head, J.W., 2002. The Moon and terrestrial planets: Geology and geophysics. In: The Century of Space Science, Bleeker, J., et al., Editors, pp. 1295-1323, Kluwer Academic Publishers, Netherlands.

Head, J.W., Gifford, A., 1980. Lunar mare domes: Classification and modes of origin. The Moon and the Planets 22, 235-258.

Head, J.W., Lloyd, D.D., 1971. Near terminator photography, Apollo 14 Preliminary Science Report, NASA Spec. Publ. SP-272, 297-300.

Head, J.W., McCord, T.B., 1978. Imbrian-age highland volcanism on Moon - Gruithuisen and Mairan domes. Science 199, 1433-1436.

Head, J.W., Wilson, L., 1979. Alphonsus-type dark-halo craters: Morphology, morphometry, and eruption conditions. Proceedings of the Tenth Lunar and Planetary Science Conference (Supplement 11, Geochimica et Cosmochimica Acta) 3, Pergamon Press, New York, 1979, pp. 2861-2897.

Head, J.W., Wilson, L., 1980. The formation of eroded depressions around the sources of lunar sinuous rilles: Observations. Lunar Planet. Sci. 11, 426-428.

Head, J.W., Wilson, L., 1981. Lunar sinuous rille formation by thermal erosion: Eruption conditions, rates and durations. Lunar Planet. Sci. 12, 427-429.

Head, J.W., Wilson, L., 1986. Volcanic processes and landforms on Venus: Theory, predictions, and observations. J. Geophys. Res. 91, 9407-9446.

Head, J.W., Wilson, L., 1987. Lava fountain heights at Pu'u O'o, Kilauea, Hawaii: Indicators of amount and variations of exsolved magma volatiles. J. Geophys. Res. 92, 13,715-713,719.

Head, J.W., Wilson, L., 1989. Basaltic pyroclastic eruptions: Influence of gas-release patterns and volume fluxes on fountain structure and the formation of cinder cones, spatter cones, rootless flows, lava ponds and lava flows. Journal of Volcanology and Geothermal Research 37, 261-271.

Head, J.W., Wilson, L., 1991. Absence of large shield volcanoes and calderas on the Moon: Consequences of magma transport phenomena? Geophys. Res. Lett. 18, 2121-2124.

Head, J.W., Wilson, L., 1992a. Lunar mare volcanism: Stratigraphy, eruption conditions, and the evolution of secondary crusts. Geochim. Cosmochim. Acta 56, 2155-2175.

Head, J. W., Wilson, L. 1992b. Magma reservoirs and neutral buoyancy zones on Venus: Implications for the formation and evolution of volcanic landforms. J. Geophys. Res. 97, 3877-3903.

Head, J.W., Wilson, L., 1993. Lunar graben formation due to near-surface deformation accompanying dike emplacement. Planetary and Space Science 41, 719-727.

Head, J. W., Wilson, L., 2002. Mars: A review and synthesis of general environments and geological settings of magma—H2O interactions. In: Volcano–Ice Interaction on Earth and Mars, Geological Society, London, Special Publication, edited by J. L. Smellie and M. G. Chapman, pp. 27-57, The Geological Society of London, London.

Head, J.W., Wilson, L., 2003. Deep submarine pyroclastic eruptions: Theory and predicted landforms and deposits. Journal of Volcanology and Geothermal Research 121, 155-193.

Head, J.W., Wilson, L., 2007. Heat transfer in volcano-ice interactions on Mars: Synthesis of environments and implications for processes and landforms. Annals of Glaciology 45, 1-13.

Head, J. W., Wilson, L., 2015. Volcanism on Mercury. In: The Encyclopedia of

Volcanoes, edited by H. Sigurdsson, B. Houghton, H. Rymer, J. Stix and S. McNutt, pp. 701-716, Academic Press.

Head, J.W., Crumpler, L.S., Aubele, J.C., Guest, J., Saunders, R.S., 1992. Venus volcanism: Classification of volcanic features and structures, associations, and global distribution from Magellan data. J. Geophys. Res. 97, 13,153-113,197.

Head, J.W., Wilson, L., Smith, D.K., 1996. Mid-ocean ridge eruptive vent morphology and structure: Evidence for dike widths, eruption rates, and evolution of eruptions and axial volcanic ridges. J. Geophys. Res. 101, 28,265-228,280.

Head, J.W., Wilson, L., Weitz, C.M., 2002. Dark ring in southwestern Orientale Basin: Origin as a single pyroclastic eruption. J. Geophys. Res. 107 (E1), doi: 10.1029/2000JE001438.

Heather, D. J., Dunkin, S. K., Wilson, L., 2003. Volcanism on the Marius Hills plateau: Observational analyses using Clementine multispectral data. J. Geophys. Res. 108, 5017, doi: 101029/2002JE001938.

Hiesinger, H., Head, J.W., 2006. New views of lunar geoscience: An introduction and overview, In: Jolliff, B., Wiezcorek, M., (Eds), New Views of the Moon, Reviews in Mineralogy and Geochemistry 60, pp. 1-81.

Hiesinger, H., Head, J.W., Wolf, U., Jaumann, R., Neukum, G., 2002. Lunar mare basalt flow units: Thicknesses determined from crater size-frequency distributions. Geophys. Res. Lett. 29, doi: 10.1029/2002GL014847.

Hiesinger, H., Head, J.W., Wolf, U., Jaumann, R., Neukum, G., 2011. Ages and stratigraphy of lunar mare basalts: A synthesis. In: *Recent Advances and Current Research Issues in Lunar Stratigraphy*, edited by W. A. Ambrose and D. A. Williams, pp. 1-51, Geological Society of America Special Paper 477.

Hood, L.L., Zakharian, A., Halekas, J., Mitchell, D.L., Lin, R.P., Acuña, M.H., Binder, A.B., 2001. Initial mapping and interpretation of lunar crustal magnetic anomalies using Lunar Prospector magnetometer data. J. Geophys. Res. 106, 27,825–27,839, doi:10.1029/2000JE001366.

Horstman, K.C., Melosh, H.J., 1989. Drainage pits in cohesionless materials: Implications for surface of Phobos. J. Geophys. Res. 94, 12,433-12,441.

Huang, J., Xiao, L., He, X., Qaio, L., Zhao, J., Li, H., 2011. Geological characteristics and model ages of Marius Hills on the Moon. J. Earth Sci. 22, 601-609.

Hulme, G., 1973. Turbulent Lava Flow and the Formation of Lunar Sinuous Rilles. Modern Geology 4, 107-117.

Hurwitz, D.M., Head III, J.W., Wilson, L., Hiesinger, H., 2012. Origin of lunar sinuous rilles: Modeling effects of gravity, surface slope, and lava composition on erosion rates during the formation of Rima Prinz. J. Geophys. Res. 117, E00H14, doi: 10.1029/2011JE004000.

Hurwitz, D.M., Head III, J.W., Hiesinger, H., 2013. Lunar sinuous rilles: Distribution, characteristics, and implications for their origin. Planet. Space Sci. 79-80, 1-38, doi: 10.1016/j.pss.2012.10.019.

Ivanov, B.A., Melosh, H.J., 2003. Impacts do not initiate volcanic eruptions: Eruptions near the crater. Geology 31, 869-872.

Ivanov, M.A., Head, J.W., Bystrov, A., 2015. The lunar Gruithuisen silicic extrusive domes: Topographic configuration, morphology, ages, and internal structure. Submitted to the Icarus special issue on Lunar Reconnaissance Orbiter.

Jaupart, C., Vergniolle, S., 1989. The generation and collapse of a foam layer at the roof of a basaltic magma chamber. J. Fluid Mech. 203, 347-380.

Jolliff, B.L., Gillis, J.J., Haskin, L.A., Korotev, R.L., Wieczorek, M.A., 2000. Major lunar crustal terranes: Surface expressions and crust-mantle origins. J. Geophys. Res. 105, 4197-4216.

Jolliff, B.L., Wiseman, S.A., Lawrence, S.J., Tran, T.N., Robinson, M.S., Sato, H., Hawke, B.R., Scholten, F., Oberst, J., Hiesinger, H., van der Bogert, C.H., Greenhagen, B.T., Glotch, T.D., Paige, D.A., 2011. Non-mare silicic volcanism on the lunar farside at Compton-Belkovich. Nature Geosci. 4, 566-571.

Jolliff, B.L., Zanetti, M., Shirley, K.A., Accardo, N.J., Lauber, C., Robinson, M.S., Greenhagen, B.T., 2012. Compton-Belkovich volcanic complex. Lunar Planet. Sci. Conf. 43, abstract 2097.

Jozwiak, L.M., Head III, J.W., Zuber, M.T., Smith, D.E., Neumann, G.A., 2012. Lunar floor-fractured craters: Classification, distribution, origin and implications for

magmatism and shallow crustal structure. J. Geophys. Res. 117, E11005, doi: 10.1029/2012JE004134.

Jozwiak, L.M., Head III, J.W., Wilson, L., 2015. Lunar floor-fractured craters as magmatic intrusions: Geometry, modes of emplacement, associated tectonic and volcanic features, and implications for gravity anomalies. Icarus 248, 424-447, doi: 10.1016/j.icarus.2014.10.052.

Jozwiak, L.M., Head III, J.W., Neumann, G.A., Wilson, L., 2015. The effect of evolving gas distribution on shallow lunar magmatic intrusion density: Implications for gravity anomalies. Lunar Planet. Sci. Conf. 46, abstract 1580.

Kato, M., Sasaki, S., Tanaka, K., Iijima, Y., Takizawa, Y., 2008. The Japanese lunar mission SELENE: Science goals and present status. Advances in Space Research 42, 294-300.

Kiefer, W. S., 2013. Gravity constraints on the subsurface structure of the Marius Hills: The magmatic plumbing of the largest lunar volcanic dome complex, J. Geophys. Res. Planets, 118, 733–745, doi:10.1029/2012JE004111.

Klimczak, C., 2014. Geomorphology of lunar grabens requires igneous dikes at depth. Geology 42, 963-966, doi: 10.1130/G35984.1.

Kreslavsky, M.A., Head J.W., Neumann, G.A., Zuber, M.T., Smith, D.E., 2016. Mare-forming lava flows on the Moon revealed by detrended LOLA topography. Lunar Planet. Sci. Conf. 47, abstract 1331.

Kusuma, K.N., Sebastian, N., Murty, S.V.S., 2012. Geochemical and mineralogical analysis of Gruithuisen region on Moon using M^3 and DIVINER images. Planet. Space Sci. 67, 46-56.

Lawrence, S.J., Stopar, J.D., Hawke, B.R., Greenhagen, B.T., Cahill, J.T.S., Bandfield, J.L., Jolliff, B.L., Denevi, B.W., Robinson, M.S., Glotch, T.D., Bussey, D.B.J., Spudis, P.D., Giguere, T.A., Garry, W.B., 2013. LRO observations of morphology and surface roughness of volcanic cones and lobate lava flows in the Marius Hills. J. Geophys. Res. 118, 615-634, doi: 10.1002/jgre.20060.

Lena, Raffaello, Wöhler, C., Phillips, J., Wirths, M., Bregante, M.T., Geologic Lunar Research (GLR) group, 2007. Lunar domes in the Doppelmayer region:

Spectrophotometry, morphometry, rheology, and eruption conditions. Planet. Space Sci. 55, 1201-1217, doi: 10.1016/j.pss.2007.01.007.

Lena, Raffaello, Wöhler, C., Bregante, M.T., Lazzarotti, P., Lammel, S., 2008. Lunar domes in Mare Undarum: Spectral and morphometric properties, eruption conditions, and mode of emplacement. Planet. Space Sci. 56, 553-569, doi: 10.1016/j.pss.2007.11.010.

Li, C., Liu, J., Zuo, W., Tan, X., Wen, W., Li, H., 2015. The Chang'e 3 mission overview. Space Science Review 190, 85-101.

Lloyd, D.D., Head, J.W., 1972. Lunar surface properties as determined from earthshine and near-terminator photography. Proceedings of the Lunar Science Conference 3, 3127-3142.

Lucchitta, B.K., Watkins, J.A., 1978. Age of graben systems on the Moon. Lunar Planet. Sci. Conf. Proc. 9, v. 3, 3459-3472.

Mason, R., Guest, J.E., Cooke, G.N., 1976. An Imbrium pattern of graben on the Moon. Geologists' Association (London) Proceedings 87, pt. 2, 161-168.

McCauley, J.F., 1964. The Marius Hills volcanic complex. Astrogeol. Studies Ann. Prog. Rpt. July 1964-July 1965, U. S. Geol. Survey, Washington, DC, 115-122.

McCauley, J.F., 1967. Geologic map of the Hevelius region of the Moon: U.S. Geol. Surv. Map, I-491, scale 1:1,000,000.

McCord, T.B., Charette, M.P., Johnson, T.V., Lebofsky, L.A., Pieters, C., 1972. Spectrophotometry (0.3 to 1.1 μm) of visited and proposed Apollo lunar landing sites. Moon 5, 52-89.

McGetchin, T.R., Head, J.W., 1973. Lunar cinder cones. Science 180, 68-71.

McGetchin, T.R., Settle, M., 1975. Cinder cone separation distances: Implications for the depth of formation of gabbroic xenoliths. EOS, Transactions, American Geophysical Union 56, 1070.

McGetchin, T.R., Ulrich, G.W., 1973. Zenoliths in maars and diatremes with inferences for the Moon, Mars and Venus. J. Geophys. Res. 78, 1832-1853.

McGill, G.E., 1971. Attitude of fractures bounding straight and arcuate lunar rilles. Icarus 14, 53-58.

McGovern, P.J., Kiefer, W.S., Kramer, G.Y., Zuber, M.T., Andrews-Hanna, J.C., Head

III, J.W., 2014. Magma ascent at lunar impact basins: Effects of lithospheric tectonic stress gradients, brittle failure, and volatile generation. Lunar and Planetary Science Conference 45, abstract 2771.

Melosh, H.J., 2011. Planetary Surface Processes. Cambridge University Press, 534 pp.

Melosh, H.J., Schenk, P., 1993. Split comets and the origin chains on Ganymede and Callisto. Nature 365, 731-733, doi: 10.1038/365731a0.

Melosh, H.J., Whitaker, E.A., 1994. Lunar crater chains. Nature 369, 713-714.

Müller, A., Binder, A.B., 1983. Linear crater chains: Indication of a volcanic organ. The Moon and the Planets 28, 87-107.

Nicholis, M.G., Rutherford, M.J., 2009. Graphite oxidation in the Apollo 17 orange glass magma: Implications for the generation of a lunar volcanic gas phase. Geochim. Cosmochim. Acta 73, 5905–5917.

Oberbeck, V.R., Morrison, R.H., 1974. Laboratory simulation of the nerringbone pattern associated with lunar secondary crater chains. The Moon 9, 415-455.

Oberbeck, V.R., Greeley, R., Morgan, R.B., Lovas, M.J., 1971. Lunar rilles - a catalog and method of classification. NASA Technical Memorandum TM X-62,088.

Okubo, C.H., Martel, S.J., 1998. Pit crater formation on Kilauea volcano, Hawaii. J. Volcanology and Geothermal Res. 86, 1-18.

Petro, N.E., Isaacson, P.J., Pieters, C.M., Jolliff, B.L., Carter, L.M., Klima, R.L., 2013. Presence of OH/H_20 associated with the lunar Compton-Belkovich volcanic complex identified by the Moon Mineralogy Mapper (M^3). Lunar Planet. Sci. Conf. 44, abstract 2688.

Petrycki, J.A., Wilson, L., 1999a. Photographic observations of lunar nearside graben. Lunar Planet. Sci. 30, abstract 1333.

Petrycki, J.A., Wilson, L., 1999b. Volcanic features and age relationships associated with lunar graben. Lunar Planet. Sci. 30, abstract 1335.

Petrycki, J.A., Wilson, L., Head, J.W., 2004. The significance of the geometries of linear graben for the widths of shallow dike intrusions on the Moon. Lunar Planet. Sci. 35, abstract 1123.

Pieters, C.M., Boardman, J., Buratti, B.J., Chatterjee, A., Clark, R., Glavich, T., Green, R., Head, J.W., Isaacson, P.J., Malaret, E., McCord, T.B., Mustard, J.F., Petro, N.

E., Runyon, C., Staid, M., Sunshine, J., Taylor, L., Tompkins, S., Varanasi, P., White, M., 2009. The Moon Mineralogy Mapper (M^3) on Chandrayaan-1. Current Science 96, 500-505.

Pieters, C.M., Besse, S., Boardman, J., Buratti, B.J., Cheek, L., Clark, R.N., Combe, J.-P., Dhingra, D., Goswami, J.N., Green, R.O., Head III, J.W., Isaacson, P.J., Klima, R.L., Kramer, G.Y., Lundeen, S., Malaret, E., McCord, T.B., Mustard, J.F., Nettles, J.W., Petro, N.E., Runyon, C., Staid, M.I., Sunshine, J.M., Taylor, L.A., Thaisen, K., Tompkins, S., Whitten, J., 2011. Mg‐spinel lithology: A new rock type on the lunar farside. J. Geophys. Res. 116, E00G08, doi:10.1029/2010JE003727

Pike, R.J., 1976. Geologic map of the Rima Hyginus region of the Moon. U.S. Geol. Surv. Misc. Geol. Invest. Map, I-945.

Prissel, T.C., Parman, S.W., Jackson, C.R.M., Dhingra, D., Ganskow, G., Cheek, L.C., Rutherford, M.J., Hess, P.C., Pieters, C.M., 2012. Melt-wallrock reactions on the Moon: Experimental constraints on the formation of newly discovered Mg-spinel anorthosites. Lunar and Planetary Science Conference, abstract 2743.

Prissel, T.C., Parman, S.W., Jackson, C.R.M., Rutherford, M.J., Hess, P.C., Head III, J.W., Cheek, L.C., Dhingra, D., Pieters, C.M., 2014. Pink Moon: The petrogenesis of pink spinel anorthosites and implications concerning Mg-suite magmatism. Earth and Planetary Science Letters 403, 144-156.

Prissel, T.C., Whitten, J.L., Parman, S.W., Head, J.W., 2015. Buoyancy driven magmatic ascent of Mg-suite parental melts. Lunar Planet. Sci. Conf. 46, abstract 1158.

Purucker, M.E., Head III, J.W., Wilson, L., 2012. Magnetic signature of the lunar South Pole-Aitken Basin: Character, origin, and age. Journal of Geophysical Research 117, E05001, doi:10.1029/2011JE003922.

Qiao, L., Head, J. W., Wilson, L., Kreslavsky, M. A., Xiao, L., 2016a. Compound flow fields in southwest Mare Imbrium: Geomorphology, source regions and implications for basin filling. Lunar Planet. Sci. Conf. 47, abstract 2038.

Qiao, L., Head, J. W., Xiao, L., Wilson, L., Dufek, J., 2016b. Sosigenes lunar Irregular Mare Patch (IMP): Morphology, topography, sub-resolution roughness and implications for origin. Lunar Planet. Sci. Conf. 47, abstract 2002.

Qiao, L., Head, J. W., Wilson, L., Xiao, L., Dufek, J., 2016c. Ina Pit Crater on the Moon: Origin as a Drained Summit Lava Lake Modified by Seismic Sieving. Geology, in review.

Rampino, M.R., Volk, T., 1996. Multiple impact event in the Paleozoic: Collision with a string of comets or asteroids? Geophys. Res. Lett. 23, 49-52.

Reeves, C., 2000. The geophysical mapping of Mesozoic dyke swarms in southern Africa and their origin in the disruption of Gondwana. J. Afr. Earth Sci. 30, 499–513, doi:10.1016/S0899-5362(00)00035-X.

Robinson, M.S., Brylow, S.M., Tschimmel, M., Humm, D., Lawrence, S.J., Thomas, P.C., Denevi, B.W., Bowman-Cisneros, E., Zerr, J., Ravine, M.A., Caplinger, M.A., Ghaemi, F.T., Schaffner, J.A., Malin, M.C., Mahanti, P., Bartels, A., Anderson, J., Tran, T.N., Eliason, E.M., McEwen, A.S., Turtle, E., Jolliff, B.L., Hiesinger, H., 2010. Lunar Reconnaissance Orbiter Camera (LROC) instrument overview. Space Sci Rev 150, 81–124, doi: 10.1007/s11214-010-9634-2.

Rosenburg, M.A., Aharonson, O., Head, J.W., Kreslavsky, M.A., Mazarico, E., Neumann, G.A., Smith, D.E., Torrence, M.H., Zuber, M.T., 2011. Global surface slopes and roughness of the Moon from the Lunar Orbiter Laser Altimeter. J. Geophys. Res. 116, doi: 10.1029/2010je003716.

Rutherford, M.J., Papale, P., 2009. Origin of basalt fire-fountain eruptions on Earth versus the Moon. Geology 37 (3) 219-222.

Rutherford, M.J., Head, J.W., Saal, A.E., Wilson, L., Hauri, E., 2015. A revised model for the ascent and eruption of gas-saturated lunar picritic magma based on experiments and lunar sample data. Lunar Planet. Sci. Conf. 46, abstact 1446.

Ryan, M.P., 1988. The mechanics and three-dimensional internal structure of active magmatic systems: Kilauea volcano, Hawaii. J. Geophys. Res. 93, 4213-4248.

Saal, A.E., Hauri, E.H., Lo Cascio, M., Van Orman, J.A., Rutherford, M.C., Cooper, R.F., 2008. Volatile content of lunar volcanic glasses and the presence of water in the Moon's interior. Nature 454 (7201), 192-195.

Schaber, G.G., 1973. Lava flows in Mare Imbrium: Geologic evaluation from Apollo orbital photography. Proc. Lunar Planet. Sci. Conf. 4th, 73–92.

Schultz, P.H., 1976a. Moon Morphology, University of Texas Press, Austin, TX, 604 pp.

Schultz P.H., 1976b. Floor-fractured lunar craters. The Moon 15. 241-273.

Schultz, P.H., Spudis, P.D., 1983. Beginning and end of lunar mare volcanism. Nature 302, 233-236.

Schultz, P.H., Staid, M.I., Pieters, C.M., 2006. Lunar activity from recent gas release. Nature 444, 184-186.

Scott, D.H., 1973. Mare Serenitatis cinder cones and terrestrial analogs, in Apollo 17 Preliminary Science Report, 30–7-30–8, NASA, Washington, D.C.

Scott, D.H., Eggleton, R.E., 1973. Geologic map of the Rümker quadrangle of the Moon. U.S. Geol. Survey Map I-805.

Settle, M., 1979. The structure and emplacement of cinder cone fields. American Journal of Science 279, 1089-1107.

Shearer, C.K. and 15 others, 2006. Thermal and magmatic evolution of the Moon. In: New Views of the Moon, Reviews in Mineralogy & Geochemistry 60, 365-518.

Shirley, K.A., Zanetti, M., Jolliff, B., van der Bogert, C. H., Hiesinger, H., 2012. Crater size-frequency distribution measurements at the Compton-Belkovich volcanic complex. Lunar Planet. Sci. Conf. 43, abstract 2792.

Shirley, K.A., Zanetti, M., Jolliff, B., van der Bogert, C.H., Hiesinger, H., 2013. Crater size-frequency distribution measurements and age of the Compton-Belkovich volcanic complex. Lunar Planet. Sci. Conf. 44, abstract 2469.

Smith, D.E., Zuber, M.T., Neumann, G.A., Lemoine, F.G., Mazarico, E., Torrence, M.H., McGarry, J.F., Rowlands, D.D., Head III, J.W., Duxbury, T.H., Aharonson, O., Lucey, P.G., Robinson, M.S., Barnouin, O.S., Cavanaugh, J.F., Sun, X., Liiva, P., Mao, D., Smith, J.C., Bartels, A.E., 2010, Initial observations from the Lunar Orbiter Laser Altimeter (LOLA). Geophys. Res. Lett. 37, L18204, doi: 10.1029/2010GL043751.

Smith, E.I., 1974. Rümker Hills: A lunar volcanic dome complex. The Moon 10, 175-181.

Solomon, S.C., Head, J.W., 1979. Vertical movement in mare basins: Relation to mare emplacement, basin tectonics and lunar thermal history. Journal of Geophysical Research 84, 1667-1682.

Solomon, S.C., Head, J.W., 1980. Lunar mascon basins: Lava filling, tectonics, and evolution of the lithosphere. Rev. Geophys. Space Phys. 18, 107-141.

Sori, M.M., Zuber, M.T., Head III, J.W., Kiefer, W.S., 2013. GRAIL search for cryptomaria. Lunar and Planetary Science Conference, abstract 2755.

Spudis, P.D., 1996. The Once and Future Moon, pp. 117-118, Smithsonian Inst. Univ. Press, Washington, D.C.

Spudis, P.D., McGovern, P.J., Kiefer, W.S., 2013. Large shield volcanoes on the Moon. J. Geophys. Res. 118, 1063-1081, doi: 10.1002/jgre.20059.

Srnka, L.J., Hoyt, J.L., Harvey, J.V.S., McCoy, J.E., 1979. A study of the Rima Sirsalis lunar magnetic anomaly. Phys. Earth Planet. Inter. 20, 281–290, doi:10.1016/0031-9201(79)90051-7.

Stopar, J.D., Hawke, B.R., Lawrence, S.J., Robinson, M.S., Giguere, T.A., 2014. Basaltic cones: A relatively common and distinct style of lunar volcanism. Lunar Planet. Sci. Conf. 45, abstract 1425.

Strain, P.L., El-Baz, F., 1980. The geology and morphology of Ina. Lunar Planet. Sci. Conf. Proc. 11, v. 3, 2609-2446.

Suavet, C., Weiss, B.P., Cassata, W.S., Shuster, D.L., Gattacceca, J., Chan, L., Garrick-Bethell, I., Head III, J.W., Grove, T.L., Fuller, M.D., 2013. Persistence and origin of the lunar core dynamo. Proceedings of the National Academy of Sciences 110, doi: 10.1073/pnas.1300341110.

Taylor, S.R., 1989. Growth of planetary crusts. Tectonophysics 161, 147-156, doi: 10.1016/0040-1951(89)90151-0.

Thorey, C., Michaut, C., 2014. A model for the dynamics of crater-centered intrusion: Application to lunar floor-fractured craters. J. Geophys. Res. 119, 286-312, doi: 10.1002/2013JE004467.

Tye, A., and J. W. Head III (2013), Mare Tranquillitatis: Distribution of mare domes, relation to broad mare rise, and evidence of a previously unrecognized basin from LOLA altimetric data, Lunar and Planetary Science Conference, XLIV, abstract 1319.

Tye, A.R., Fassett, C.I., Head III, J.W., Mazarico, E., Basilevsky, A.T., Neumann, G.A., Smith, D.E., Zuber, M.T., 2015. The age of lunar south circumpolar craters

Haworth, Shoemaker, Faustini, and Shackleton: Implications for regional geology, surface processes, and volatile sequestration. Icarus 255, 70-77.

Wagner, R.J., Head, J.W., Wolf, U., Neukum, G., 2002. Stratigraphic sequence and ages of volcanic units in the Gruithuisen region of the Moon. Journal of Geophysical Research 107, 5104, doi: 10.1029/2002JE001844.

Wagner, R., Head, J. W., Wolf, U., Neukum, G., 2010. Lunar red spots: Stratigraphic sequence and ages of domes and plains in the Hansteen and Helmet regions on the lunar nearside. J. Geophys. Res., 115, E06015, doi:10.1029/2009JE003359.

Walker, G.P.L., 1988. Three Hawaiian calderas: An origin through loading by shallow instrusions? J. Geophys. Res. 93, 14,773-14,784.

Weitz, C., Head, J.W., 1999. Spectral properties of the Marius Hills volcanic complex and implications for the formation of lunar domes and cones. J. Geophys. Res. 104, 18,933-18,956.

Weitz, C.M., Head, J.W., Pieters, C.M., 1998. Lunar regional dark mantle deposits: Geologic, multispectral, and modeling studies. J. Geophys. Res.103, 22,725–22,759.

Weitz, C.M., Rutherford, M.J., Head, J.W., McKay, D.S., 1999. Ascent and eruption of a lunar high-titanium magma as inferred from the petrology of the 74001/2 drill core. Meteoritics and Planetary Science 34, 527-540.

Wetzel, D. T., Hauri, E. H., Saal, A. E., and Rutherford, M. J., 2015, Carbon content and degassing history of the lunar volcanic glasses. Nature Geosci. 8, 755–758, doi:10.1038/ngeo2511.

Wichman, R.W., Schultz, P.H., 1995. Floor-fractured craters in Mare Smythii and west of Oceanus Procellarum: Implications of crater modification by viscous relaxation and igneous intrusion models. Journal of Geophysical Research 100, 21,201-221,218.

Wichman, R.W., Schultz, P.H., 1996. Crater-centered laccoliths on the Moon: Modeling intrusion depth and magmatic pressure at the crater Taruntius. Icarus 122, 193-199.

Whitford-Stark, J.L., Head, J.W., 1977. The Procellarum volcanic complexes: Contrasting styles of volcanism. In: *Proceedings of the Eighth Lunar Science*

Conference (Supplement 8, *Geochimica et Cosmochimica Acta*), pp. 2705-2724, Pergamon Press, New York.

Whitford-Stark, J.L., Head, J.W., 1980. Stratigraphy of Oceanus Procellarum basalts: Sources and styles of emplacement. J. Geophs. Res. 85, 6579-6609.

Whitten, J.L., Head III, J.W., 2015a. Lunar cryptomaria: Physical characteristics, distribution, and implications for ancient volcanism. Icarus 247, 150-171, doi: 10.1016/j.icarus.2014.09.031.

Whitten, J.L., Head III, J.W., 2015b. Lunar cryptomaria: Mineralogy and composition of ancient volcanic deposits. Planet. Space Sci. 106, 67-81, doi: 10.1016/j.pss.2014.11.027.

Whitten, J.L., Head III, J.W., 2013. Detecting volcanic resurfacing of heavily cratered terrain: Flooding simulations on the Moon using Lunar Orbiter Laser Altimeter (LOLA) data. Planetary and Space Science 85, 24-37, doi: 10.1016/j.pss.2013.05.013.

Whitten, J., Head III, J.W., Staid, M.I., Pieters, C.M., Mustard, J.F., Clark, R., Nettles, J.W., Klima, R.L., Taylor, L.A., 2011. Lunar mare deposits associated with the Orientale impact basin: New insights into mineralogy, history, mode of emplacement, and relation to Orientale Basin evolution from Moon Mineralogy Mapper (M^3) data from Chandrayaan-1. J. Geophys. Res. 116, doi: 10.1029/2010JE003736.

Wichman, R.W., Schultz, P.H., 1995. Floor-fractured craters in Mare Smythii and west of Oceanus Procellarum: Implications of crater modification by viscous relaxation and igneous intrusion models. J. Geophys. Res. 100(E10), 21,201-21,218.

Wichman, R.W., Wood, C.A., 1995. The Davy Crater Chain: Implications for tidal disruption in the Earth-Moon system and elsewhere. Geophys. Res. Lett. 22, 583-586.

Wieczorek, M.A., Zuber, M.T. Phillips, R.J., 2001. The role of magma buoyancy on the eruption of lunar basalts. Earth Planet. Sci. Lett. 185, 71-83, doi: 10.1016/S0012-821X(00)00355-1.

Wieczorek, M.A., Jolliff, B.L., Khan, A., Pritchard, M.E., Weiss, B.P., Williams, J.G., Hood, L.L. Righter, K., Neal, C.R., Shearer, C.K., McCallum, I.S., Tompkins, S.,

Hawke, B.R., Peterson, C., Gillis, J.J., Bussey, B., 2006. The constitution and structure of the lunar interior. In: Jolliff, B., Wiezcorek, M., (Eds), New Views of the Moon, Reviews in Mineralogy and Geochemistry 60, pp. 221-364.

Wilhelms, D.E., 1968. Geologic map of the Mare Vaporum quadrangle of the Moon. U.S. Geol. Surv. Misc. Invest. Map, I-548.

Wilhelms, D.E., 1987. *The geologic history of the Moon*. U.S. Geol. Surv., Prof. Paper 134.

Wilhelms, D.E., Hodges, C.A., 1978. Plate 56. In: Apollo Over the Moon: A View from Orbit. Masursky, H., Colton, G.W., El-Baz, F. (Eds.). NASA SP-362, Washington, DC.

Williams, D.A., Fagents, S.A., Greeley, R., 2000. A reevaluation of the emplacement and erosional potential of turbulent, low-viscosity lavas on the Moon. J. Geophys. Res. 105, 20,189–20,206.

Wilson, L., Head, J.W., 1980. The formation of eroded depressions around the sources of lunar sinuous rilles: theory. Lunar Planet. Sci. 11, 1260-1262.

Wilson, L., Head, J.W., 1981. Ascent and eruption of basaltic magma on the Earth and Moon. J. Geophys. Res. 86, 2971-3001.

Wilson, L., Head, J.W., 1988. Nature of local magma storage zones and geometry of conduit systems below basaltic eruption sites: Pu'u O'o, Kilauea, East Rift, Hawaii example. J. Geophys. Res. 93, 14,785-714,792.

Wilson, L., Head, J.W., 1994. Mars: Review and analysis of volcanic eruption theory and relationships to observed landforms. Reviews of Geophysics 32, 221-263.

Wilson, L., Head, J.W., 2003a. Deep generation of magmatic gas on the Moon and implications for pyroclastic eruptions. Geophys. Res. Lett. 30 (12), 1605, doi: 10.1029/2002GL016082.)

Wilson, L., Head, J.W., 2003b. Lunar Gruithuisen and Mairan domes: Rheology and mode of emplacement. J. Geophys. Res. 108, doi 10.1029/2002JE001909.

Wilson, L., Head, J.W., 2007a. An integrated model of kimberlite ascent and eruption. Nature 447 (7140), 53-57, doi:10.1038/nature05692.)

Wilson, L., Head, J., 2007b. Explosive volcanic eruptions on Mars: Tephra and accretionary lapilli formation, dispersal and recognition in the geologic record.

Journal of Volcanology and Geothermal Research 163, 83-97, doi: 10.1016/j.jvolgeores.2007.03.007.

Wilson, L., Head, J.W., 2007c. Heat transfer in volcano-ice interactions on Earth. Annals of Glaciology 45, 83-86.

Wilson, L., Head, J.W., 2008. Volcanism on Mercury: A new model for the history of magma ascent and eruption. Geophysical Research Letters 35, L23205, doi: 10.1029/2008GL035860.

Wilson, L., Head III, J.W., 2016a. Generation, ascent and eruption of magma on the Moon: New insights into source depths, magma supply, intrusions and effusive/explosive eruptions (Part 1: Theory). Icarus, in press, doi:10.1016/j.icarus.2015.12.039.

Wilson, L., Hawke, B.R., Giguere, T.A., Petrycki, E.R., 2011. An igneous origin for Rima Hyginus and Hyginus crater on the Moon. Icarus 215, 584-595.

Wilson, L., J. W. Head III, and A. R. Tye (2014), Lunar regional pyroclastic deposits: Evidence for eruption from dikes emplaced into the near-surface crust. Lunar and Planetary Science Conference, XLV, abstract 1223.

Wilson, L., Head, J.W., 2016b. Explosive volcanism associated with the silicic Compton-Belkovich volcanic complex: Implications for magma water content. Lunar Planet. Sci. Conf. 47, abstract 1564.

Wöhler, C., Lena, R., Lazzarotti, P., Phillips, J., Wirths, M., Pujic, Z., Geologic Lunar Research (GLR) Group, 2006. A combined spectrophotometric and morphometric study of the lunar mare dome fields near Cauchy, Arago, Hortensius, and Milichius. Icarus 183, 237-264, doi: 10.1016/j.icarus.2006.03.003.

Wöhler, C., Lena, R., Lazzarotti, P., Phillips, J., 2007. Formation of lunar mare domes along crustal fractures: Rheologic conditions, dimensions of feeder dikes, and the role of magma evolution. Icarus 189, 279-307, doi: 10.1016/j.icarus.2007.01.011.

Yingst, R.A., Head, J.W., 1997. Volumes of lunar lava ponds in South Pole-Aitken and Orientale basins: Implications for eruption conditions, transport mechanisms and magma source regions. J. Geophys. Res. 102, 10,909-10,931.

Zisk, S.H., Hodges, C.A., Moore, H.J., Shorthill, R.W., Thompson, T.W., Whitaker, E.A., Wilhelms, D.E., 1977. The Aristarchus-Harbinger region of the Moon:

Surface geology and history from recent remote sensing observations. The Moon 17, 59-99.

Zuber, M.T., Mouginis-Mark, P.J., 1992. Caldera subsidence and magma chamber depth of the Olympus Mons volcano, Mars. J. Geophys. Res. 97, 18,295-18,307.

Zuber, M.T., Smith, D.E., Zellar, R.S., Neumann, G.A., Sun, X., Katz, R.B., Kleyner, I., Matuszeski, A., McGarry, J.F., Ott, M.N., Ramos-Izquierdo, L.A. Rowlands, D.D., Torrence, M.H., Zagwodzki, T.W., 2010. The Lunar Reconnaissance Orbiter Laser Ranging Investigation. Space Sci. Rev. 150, 63–80, doi: 10.1007/s11214-009-9511-z.

Zuber, M.T., Head III, J.W., Smith, D.E., Neumann, G.A., Mazarico, E., Torrence, M.H., Aharonson, O., Tye, A.R., Fassett, C.I., Rosenburg, M.A., Melosh, H.J., 2012. Constraints on brightening and volatile distribution within Shackleton crater at the lunar south pole. Nature 486, 378–381, doi: 10.1038/nature11216.

Zuber, M.T., Smith, D.E., Watkins, M.M., Asmar, S.W., Konopliv, A.S., Lemoine, F.G., Melosh, H.J., Neumann, G.A., Phillips, R.J., Solomon, S.C., Wieczorek, M.A., Williams, J.G., Goossens, S.J., Kruizinga, G., Mazarico, E., Park, R.S., Yuan, D.-N., 2013. Gravity field of the Moon from the Gravity Recovery and Interior Laboratory (GRAIL) mission. Science 339, doi: 10.1126/science.1231507.

Figure Captions:

Figure 1. Mare volcanism and secondary crust formation in the context of lunar history. a) Types of planetary crusts (modified after Head, 1999; conceptual framework from Taylor, 1989). b) Global map showing the distribution of lunar mare basalts (purple) and cryptomaria (light green) (Whitten et al., 2015a,b)**.** Basemap is LOLA hillshade, equidistant cylindrical projection. c) Chronology of magmatic-volcanic events in lunar history. (1) Elkins-Tanton et al. (2011); (2) Shearer et al. (2015); (3) Nyquist and Shih (1992); (4) Shearer et al. (2006); (5) Stoffler and Ryder (2006); (6)Wagner et al.

(2002; 2010); (7) Whitten et al. (2015a,b); (8) Hiesinger et al. (2011); (9) Borg et al. (2004); (10) Hurwitz et al. (2013); (11) Jolliff et al. (2011); (12) Braden et al. (2014); (13) Schultz et al. (2006); (14) Solomon and Head (1980).

Figure 2. Cross-sectional portrayal of the balance of forces in diapir formation and rise, brittle fracturing and dike propagation, and their relationship to changes in style during lunar thermal evolution.

Figure 3. Generation, ascent and eruption of lunar mare basalt magma. Relationships of rising diaper, accumulation of magma in the melt zone, and factors leading to eruption.

Figure 4. Major factors in dike initiation and rise.

Figure 5. Factors influencing the stalling and evolution of dikes emplaced in the crust. a) Factors influencing the stalling of a rising dike. b) Factors influencing emplacement of a shallow intrusion and formation of laccoliths and sills. c) Structure of a dike as it approaches the surface and stalls at shallow depths. d) Initial gas venting to the surface of a stalled dike. e) Stalled dike vents gas to the surface forming a lunar ultraplinian-type eruption. f) Convection in wide stalled dike builds up excess gas and pressure, gas vents to the surface, forms Ionian-type eruption (after Head et al., 2003). g) Stalled dike solidifies in upper part, resulting gas buildup causes explosive disruption of solidified cap and country rock, producing a lunar vulcanian-style eruption.

Figure 6. Lunar dike geometry upon approach to the surface, stalling and penetrating to the surface. a) Dike tip approaches surface (blade-shaped cross-sectional view). b) Dike tip approaches surface and penetrates to surface (penny-shaped cross-sectional view). c) Dike tip stalls in shallow crust, but at greater depths, resulting in crater-chain formation (map view). d) Dike tip stalls in shallow crust, but at shallower depths, resulting in graben formation (map view). e) Dike tip propagates to surface, erupts to form lava flow (map view).

Figure 7. Behavior of gas/foam-filled dike tip upon arrival at the surface. a) Choked flow. b) Unchoked (pressure-balanced) flow. c) General relationships for gas venting on the Moon.

Figure 8. Detailed cross-section of the geometry of dike and graben formation. a) absence of volcanics is associated with a narrow dike that does not approach close to the surface and produces a shallow and wide graben, relative to b) presence of volcanics is

associated with a wide dike that approaches closer to the surface and produces a deeper and narrower graben. See Petrycki et al. (2004).

Figure 9. Lunar Hawaiian-style eruption fire-fountain structure and deposits. a) Details of fountain structure and consequences of accumulation. b) Types of pyroclastic beads predicted and observed in lunar samples and relationship to cooling rate (after Weitz et al., 1998, 1999). c) Relationship of eruption plume optical density accumulation rate and pyroclastic bead type (after Weitz et al., 1998, 1999).

Figure 10. Lunar strombolian-style eruption structure.

Figure 11. Effusive eruptions. a) General nature of lunar steady effusive volcanic eruptions producing lava flows. b) Lava flow heat loss mechanisms from a simple lava flow on any planet having an atmosphere. Either natural or forced convection will eventually dominate the radiation and conduction processes. Solid crust thickness will increase with time and hence distance from the vent. The motion of the flow lobe will cease when cooling fronts have penetrated to a significant fraction of its thickness. On planetary bodies without an atmosphere, convective heat loss is absent and radiation from the upper surface dominates heat loss.

Figure 12. Limits to lava flow length. a) Volume-limited flow in which the lava flow advances until the magma supply is depleted. b) Cooling-limited flow in which the forward advance of the lava flow ceases due to cooling, resulting in breakouts in the proximal and medial flow regions. c) Preexisting topography causes lava flow to pond in crater or depression. Vertical accumulation inflates flow and deforms/disrupts uppermost cooling thermal boundary layer. Flow thickness can exceed hundreds of meters, prolonging cooling.

Figure 13. Evolution of vent structure from linear to circular, and the effects on magma flux and formation of sinuous rilles. a) Initial stage in dike penetration to the surface. b) Continued peak flux thermally erodes wide place in dike to circular shape, favoring higher fluxes and sinuous rille formation.

Figure 14. The evolutionary behavior of dikes during eruptions.

Figure 15. The relationship of the crust and elastic lithosphere in early lunar history and the effects on dike propagation and environments for the production of evolved magmas.

Figure 16. Synthesis block diagram of mare basalt dikes approaching, stalling, intruding and erupting on the Moon.

Figure 17. Mendeleev Crater Chain on the floor of the farside Mendeleev Crater (6.50^{o}N, 139.13^{o}E). WAC M118939946M**.**

Figure 18. Small crater chains in southern Mare Serenitatis (18.26^{o}N, 26.10^{o}E). Kaguya TCO_MAPe04_N21E024N18E027SC.

Figure 19. Lunar domes interpreted as small shield volcanoes. a) Tobias Mayer small shield volcano (13.15^{o}N, 31.03^{o}W); note elongate central vent and small graben to southeast on the other side of the highland massif, probably part of the same dike at depth, and subsequent sinuous rille flowing around dome. Kaguya TC_TCO_MAPe04_N15E327N12E330SC. b) Small shield volcano, Milicius Pi (10.08^{o}N, 31.25^{o}W); note central vent and rough margins, interpreted to be the distal parts of cooling-limited flows. Kaguya TC_TCO_MAPe04_N12E327N09E330SC.

Figure 20. Hyginus Rille (7.76^{o}N, 6.26^{o}E): Two graben, each containing pit craters, extend from the central depression. LROC WAC mosaic.

Figure 21. Rimae Parry graben and row of cones and pyroclastic deposits (white arrows) along the western rille (7.26^{o}S, 16.69^{o}W). Kaguya TC_TCO_MAPe04_S06E342S09E345SC.

Figure 22. Global Distribution of linear and arcuate rilles interpreted as graben with and without evidence for associated volcanic features. Red dots show rilles with evidence of volcanic associations, bright green dots show rilles with no evidence of volcanism. After Petrycki and Wilson (1999a,b) and Petrycki et al. (2004). Distribution of lunar mare basalts (purple) and cryptomaria (light green) (Whitten et al., 2015a,b)**.** Basemap is LOLA hillshade, equidistant cylindrical projection.

Figure 23. Lunar floor-fractured craters (FFCs). a) Global distribution of floor-fractured craters (Jozwiak et al., 2012). On the basis of crater floor shape and structure, those FFCs greater than 40 km diameter (black dots) are interpreted to be sills, and those less than 40 km (white dots) are interpreted to be laccoliths (Jozwiak et al., 2015). b) Morphology, topography and structure of the crater Vitello, 42.5 km in diameter (30.42^{o}S, 37.55^{o}W), and LOLA topographic profile. c) Morphology, topography and structure of the crater Humboldt, 207 km in diameter (56.92^{o}N, 81.54^{o}E) and LOLA

topographic profile. d) Block diagram showing three steps in the relationship of magma intrusion and sill and laccolith structure and interpreted magma intrusion evolution.

Figure 24. Cones and lines of cones with associated structures. a) Row of pyroclastic cones on the floor of the 33 km diameter highland crater Palisa (9.50^{o}S, 7.21^{o}W). Crater floor is highland plains but the linear chain of small domes is interpreted to have been emplaced by a dike just penetrating to the surface and degassing to produce small cones and related local pyroclastic accumulations. Inset shows cone detail. Kaguya TC image TCO_MAPeLsugE35/S12, E354SC. b) Secchi X linear rilles (0.41^{o}S, 43.01^{o}W) (trending NE-SW) and row of dark pyroclastic cones (trending NW-SE). Kaguya TC_TCO_MAPe04_N00E042S03E045SC. c) Milichius Pi row of cones (10.74^{o}N, 31.74^{o}W) along subdued graben. Kaguya TC_TCO_MAPe04_N12E327N09E330SC. d) Row of pyroclastic cones along a linear feature and adjacent and cross-cutting graben and crater chains (18.84^{o}N, 27.60^{o}E). The northern cone is elongate and breached (Isis) and the southern cone is more symmetrical (Osiris). Note sinuous rille extending along the eastern margin of the image. Southernmost Mare Serenitatis. Kaguya TCO_MAPe04_N21E027N18E030SC. e) Positive linear ridge along an aligned feature (18.61^{o}N, 31.96^{o}W) that also includes vents (to the NE in the hills, with some possible associated late-stage stubby flows) and a narrow graben-like structure further to the NE. This linear feature is interpreted to be magma extruded rather passively from the dike in the waning stages of the eruption as the dike walls were closing (see Figure 14). LROC WAC M116520192M.

Figure 25. Large, 154 km diameter pyroclastic ring in the southwestern part of the Orientale Basin along the Montes Rook ring (29.51^{o}S, 97.77^{o}W). Note the elongate 7.5 km by 16 km central depression, interpreted to be the vent for this Ionian-style eruption (Head et al., 2002). LROC WAC mosaic.

Figure 26: Examples of lunar pyroclastic deposits. a) Global distribution of lunar pyroclastics (after Gaddis et al., 2003) (red dots; with size ranging from small to large with size of dot). Also shown is the distribution of lunar mare basalts (purple) and cryptomaria (light green) (Whitten et al., 2015a,b). Basemap is LOLA hillshade, equidistant cylindrical projection. b) Model of gas formation in rising dike tip (after Wilson and Head, 2003a). c) Dark halo craters along fractures and graben on the floor of

Alphonsus crater (12.77°S, 1.79°W). Kaguya TC TCO_MAPe_S12E57S15E360SC. d) Regional dark mantle deposits in the Sinus Aestuum region (6.15°N, 7.63°W). LROC WAC. e) Regional dark mantle deposits in the Rima Bode region (12.67°N, 3.19°W). LROC WAC mosaic. f) Nested sinuous rille (Cobra Head and Schroter's Valley) at the Aristarchus Plateau (24.88°N, 49.27°W). Top, WAC image mosaic. Bottom, LOLA altimetric profile.

Figure 27. Small shield volcanoes. a) Small shield volcano groupings and density in Mare Tranquillitatis (Tye and Head, 2013). b) Regional distribution of small shield volcanoes in Mare Tranquillitatis (Tye and Head, 2013). c) Diagrammatic representation of sequence of events in the building of small lunar shield volcanoes.

Figure 28. Large shield volcanoes with calderas on the Earth (top) and reasons for the lack of similar features on the Moon (bottom) (modified from Head and Wilson, 1991).

Figure 29. Compound lava flow fields. a) Modes of formation of compound flow fields. b) Examples of compound flow fields and extensive single flows in southwest Mare Imbrium (35.54°N, 18.79°W). Detrended LOLA data (Kreslavsky and Head, 2015). c) Extensive single flows in southwest Mare Imbrium (28.02°N, 29.92°W). Apollo AS15-M-1559.

Figure 30. Distribution and characteristics of lunar sinuous rilles. a) Global distribution of lunar sinuous rilles (after Hurwitz et al., 2013). Distribution of lunar mare basalts (purple) and cryptomaria (light green) (Whitten et al., 2015a,b)**.** Basemap is LOLA hillshade, equidistant cylindrical projection. b) Size frequency distribution of sinuous rille length (after Hurwitz et al., 2013). c) Size frequency distribution of sinuous rille width (after Hurwitz et al., 2013). d) Size frequency distribution of sinuous rille depth (after Hurwitz et al., 2013). e) Nested sinuous rille at Rima Prinz (26.37°N, 43.73°W). Complementary illumination geometry with Kaguya TC (left; TCO_MAPe04_N27E315N24E318SC) and LROC WAC mosaic (right) reveal inner and marginal structure of the feature.

Figure 31. Volcanic complexes on the Moon. LOLA topography over LOLA hillshade. a) Rumker Hills. b) Aristarchus Plateau-Rimae Prinz/Harbinger Mountains. c) Marius Hills.

Figure 32. Silicic domes and Compton-Belkovich volcanic complex. a) Gruithuisen Gamma (center) (36.64^{o}N, 40.72^{o}W). Kaguya TC image TCO_MAPm04_N39E318N36E321SC. b) Compton-Belkovich volcanic complex (CBVC) topography. WAC GLD100 draped over WAC visible image (61.1^{o} N, 99.5^{o} E). From Jolliff et al. (2011). c) Block diagram of the Compton-Belkovich volcanic complex (CBVC) as interpreted by Jolliff et al. (2011).

Figure 33. Irregular Mare Patches (IMPs) on the Moon (Braden et al., 2014). a) The Ina feature (18.66^{o}N 5.30^{o}E); feature is ~ 2 x 3 km; North is up. LROC NAC M118008722LE. b) Block diagram showing the major features and characteristics and their interpretation as described by Braden et al. (2014). c) Oblique view of the Sosigenes structure and the Irregular Mare Patch (IMP) on the floor (8.33^{o}N, 19.07^{o}E) in western Mare Tranquillitatis. View is looking toward the west; the depression is ~ 7.2 km long and 2.8 km wide. LROC NAC M11081179DLR) d) Interpretation of the Sosigenes IMP by a mechanism of regolith sifting and drainage into subsurface void space (see also, Qiao et al, 2016b).

Table 1. Parameters of lunar hawaiian-style eruptions. The maximum pyroclast range R_f is given as a function of the released volatile content, *n*, expressed as equivalent amount of CO. Then for each of a series of values of the erupted volume flux, F_e, values are given for the thickness, *X*, of the optically thin outer shell of the fire fountain from which heat can be lost; the radial distance from the vent, (R_f - *X*), of the optically thick region within which clasts are so densely packed that they cannot radiate heat and so fall to the ground at magmatic temperatures to coalesce into a lava pond; and the Reynolds number, *Re*, of the motion of the lava in the pond: values of *Re* greater than 2000 (shown in bold face) imply turbulence and the possibility of thermal erosion of the base of the pond to form a sinuous rille source depression. Values underlined and in italics correspond to hot pond radii larger than those seen on the Moon and imply that volatile contents in rille-forming eruptions are less than ~700 ppm.

Table 1

Table 1. Parameters of lunar hawaiian-style eruptions. The maximum pyroclast range R_f is given as a function of the released volatile content, n, expressed as equivalent amount of CO. Then for each of a series of values of the erupted volume flux, F_e, values are given for the thickness, X, of the optically thin outer shell of the fire fountain from which heat can be lost; the radial distance from the vent, (R_f - X), of the optically thick region within which clasts are so densely packed that they cannot radiate heat and so fall to the ground at magmatic temperatures to coalesce into a lava pond; and the Reynolds number, *Re*, of the motion of the lava in the pond: values of *Re* greater than 2000 (shown in bold face) imply turbulence and the possibility of thermal erosion of the base of the pond to form a sinuous rille source depression. Values underlined and in italics correspond to hot pond radii larger than those seen on the Moon and imply that volatile contents in rille-forming eruptions are less than ~700 ppm.

		F_e = 50 m^3/s			F_e = 250 m^3/s			F_e = 500 m^3/s			F_e = 1000 m^3/s			F_e = 10,000 m^3/s			F_e = 100,000 m^3/s		
		cold shell	hot radius	hot pool	cold shell	hot radius	hot pool	cold shell	hot radius	hot pool	cold shell	hot radius	hot pool	cold shell	hot radius	hot pool	cold shell	hot radius	hot pool
n/ppm	R_f/m	X/m	(R_f - X)/m	*Re*	X/m	(R_f - X)/m	*Re*	X/m	(R_f - X)/m	*Re*	X/m	R_f - X)/m	*Re*	X/m	(R_f - X)/m	*Re*	X/m	(R_f - X)/m	*Re*
100	326	90	235	445	**18**	**308**	**2226**	**9**	**317**	**4452**	**5**	**321**	**8904**	**0**	**325**	**89039**	**0**	**326**	**890390**
150	489	249	240	297	50	439	1484	**25**	**464**	**2968**	**12**	**476**	**5936**	**1**	**487**	**59359**	**0**	**488**	**593593**
200	651	510	141	223	102	549	1113	**51**	**600**	**2226**	**26**	**626**	**4452**	**3**	**649**	**44519**	**0**	**651**	**445195**
250	814	891	0	178	178	636	890	89	725	1781	**45**	**770**	**3562**	**4**	**810**	**35616**	**0**	**814**	**356156**
300	977	1406	0	148	281	696	742	141	836	1484	**70**	**907**	**2968**	**7**	**970**	**29680**	**1**	**976**	**296797**
400	1303	2887	0	111	577	725	556	289	1014	1113	**144**	**1158**	**2226**	**14**	**1288**	**22260**	**1**	**1301**	**222597**
500	1629	5043	0	89	1009	620	445	504	1124	890	252	1376	1781	**25**	**1603**	**17808**	**3**	**1626**	**178078**
600	1954	7955	0	74	1591	363	371	795	1159	742	398	1556	1484	**40**	**1914**	**14840**	**4**	**1950**	**148398**
700	2280	11695	0	64	2339	0	318	1169	1110	636	585	1695	1272	***58***	***2221***	***12720***	***6***	***2274***	***127199***
800	2606	16329	0	56	3266	0	278	1633	973	556	816	1789	1113	***82***	***2524***	***11130***	***8***	***2597***	***111299***
900	2931	21920	0	49	4384	0	247	2192	739	495	1096	1835	989	***110***	***2822***	***9893***	***11***	***2920***	***98932***
1000	3257	28526	0	45	5705	0	223	2853	404	445	1426	1831	890	***143***	***3114***	***8904***	***14***	***3243***	***89039***
1200	3908	44998	0	37	9000	0	185	4500	0	371	2250	1659	742	***225***	***3683***	***7420***	***22***	***3886***	***74199***
1400	4560	66154	0	32	13231	0	159	6615	0	318	3308	1252	636	***331***	***4229***	***6360***	***33***	***4527***	***63599***
1600	5211	92372	0	28	18474	0	139	9237	0	278	4619	593	556	***462***	***4749***	***5565***	***46***	***5165***	***55649***
1800	5863	123999	0	25	24800	0	124	12400	0	247	6200	0	495	***620***	***5243***	***4947***	***62***	***5801***	***49466***
2000	6514	161366	0	22	32273	0	111	16137	0	223	8068	0	445	***807***	***5707***	***4452***	***81***	***6433***	***44519***
3000	9771	444674	0	15	88935	0	74	44467	0	148	22234	0	297	***2223***	***7548***	***2968***	***222***	***9549***	***29680***
4000	13028	912827	0	11	182565	0	56	91283	0	111	45641	0	223	***4564***	***8464***	***2226***	***456***	***12572***	***22260***
5000	16285	1594642	0	9	318928	0	45	159464	0	89	79732	0	178	*7973*	*8312*	*1781*	***797***	***15488***	***17808***
7500	24428	4394318	0	6	878864	0	30	439432	0	59	219716	0	119	*21972*	*2456*	*1187*	***2197***	***22230***	***11872***
10000	32570	9020660	0	4	1804132	0	22	902066	0	45	451033	0	89	*45103*	*0*	*890*	***4510***	***28060***	***8904***

Figure 1abc

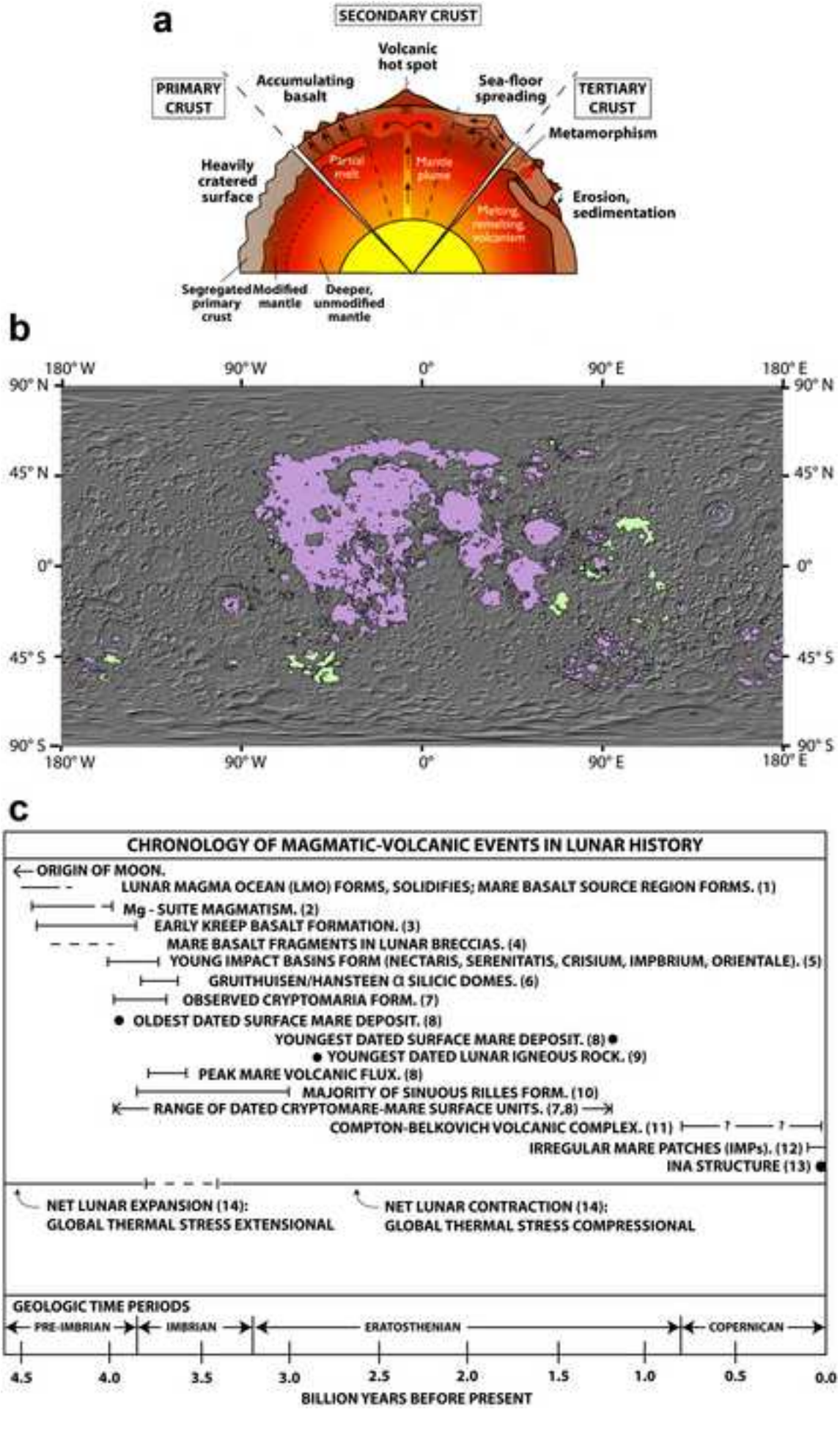
a
SECONDARY CRUST
Volcanic hot spot
PRIMARY CRUST
Accumulating basalt
Sea-floor spreading
TERTIARY CRUST
Metamorphism
Heavily cratered surface
Partial melt
Mantle plume
Erosion, sedimentation
Melting, remelting, volcanism
Segregated primary crust
Modified mantle
Deeper, unmodified mantle
b
180° W
90° W
0°
90° E
180° E
90° N
45° N
0°
45° S
90° S
c
CHRONOLOGY OF MAGMATIC-VOLCANIC EVENTS IN LUNAR HISTORY
ORIGIN OF MOON.
LUNAR MAGMA OCEAN (LMO) FORMS, SOLIDIFIES; MARE BASALT SOURCE REGION FORMS. (1)
Mg - SUITE MAGMATISM. (2)
EARLY KREEP BASALT FORMATION. (3)
MARE BASALT FRAGMENTS IN LUNAR BRECCIAS. (4)
YOUNG IMPACT BASINS FORM (NECTARIS, SERENITATIS, CRISIUM, IMPBRIUM, ORIENTALE). (5)
GRUITHUISEN/HANSTEEN Cl SILICIC DOMES. (6)
OBSERVED CRYPTOMARIA FORM. (7)
OLDEST DATED SURFACE MARE DEPOSIT. (8)
YOUNGEST DATED SURFACE MARE DEPOSIT. (8)
YOUNGEST DATED LUNAR IGNEOUS ROCK. (9)
PEAK MARE VOLCANIC FLUX. (8)
MAJORITY OF SINUOUS RILLES FORM. (10)
RANGE OF DATED CRYPTOMARE-MARE SURFACE UNITS. (7,8)
COMPTON-BELKOVICH VOLCANIC COMPLEX. (11)
IRREGULAR MARE PATCHES (IMPs). (12)
INA STRUCTURE (13)
NET LUNAR EXPANSION (14): GLOBAL THERMAL STRESS EXTENSIONAL
NET LUNAR CONTRACTION (14): GLOBAL THERMAL STRESS COMPRESSIONAL
GEOLOGIC TIME PERIODS
PRE-IMBRIAN
IMBRIAN
ERATOSTHENIAN
COPERNICAN
4.5
4.0
3.5
3.0
2.5
2.0
1.5
1.0
0.5
0.0
BILLION YEARS BEFORE PRESENT

Figure 2

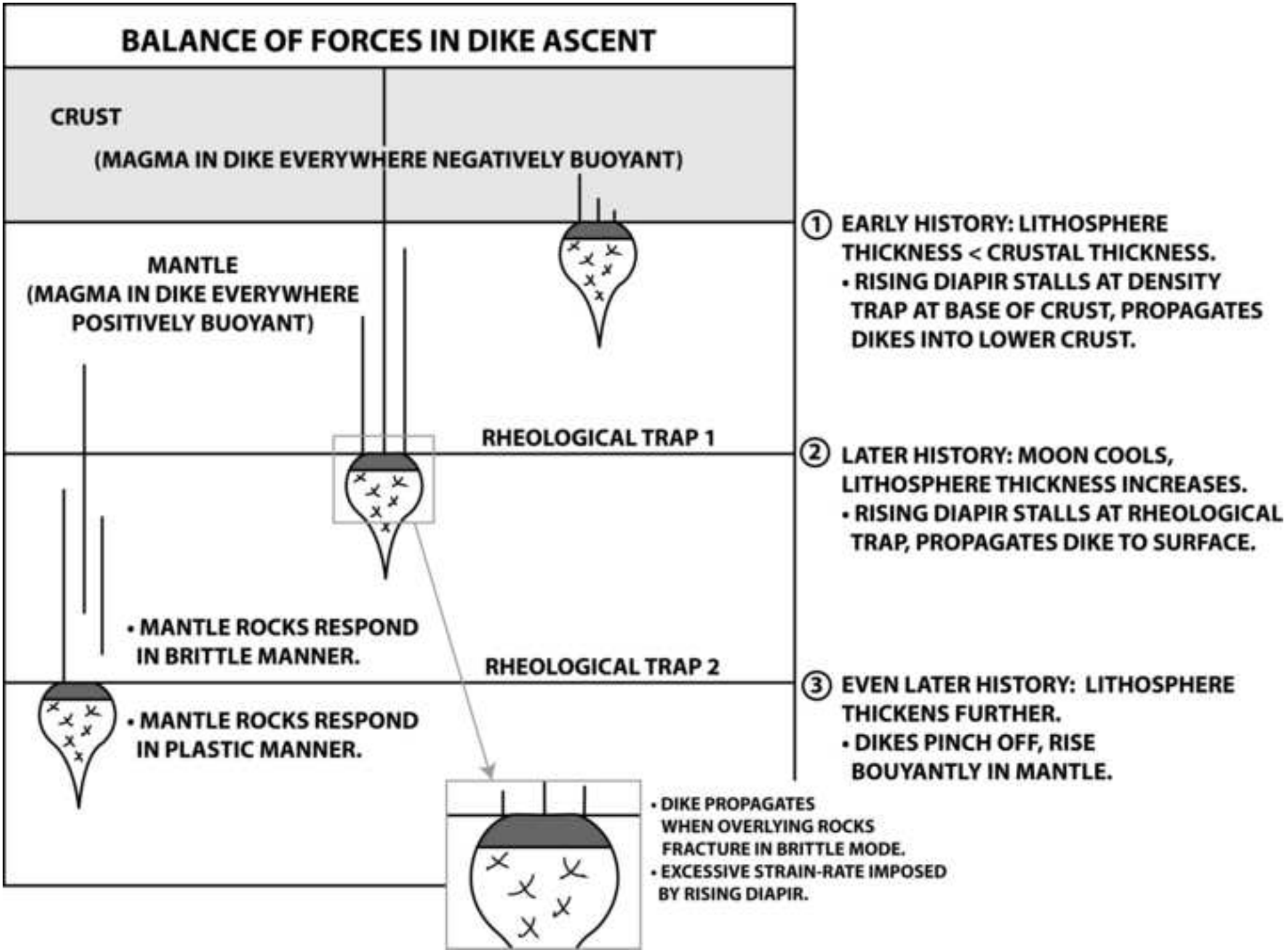
BALANCE OF FORCES IN DIKE ASCENT
CRUST
(MAGMA IN DIKE EVERYWHERE NEGATIVELY BUOYANT)
MANTLE
(MAGMA IN DIKE EVERYWHERE POSITIVELY BUOYANT)
RHEOLOGICAL TRAP 1
RHEOLOGICAL TRAP 2
• MANTLE ROCKS RESPOND IN BRITTLE MANNER.
• MANTLE ROCKS RESPOND IN PLASTIC MANNER.
① EARLY HISTORY: LITHOSPHERE THICKNESS < CRUSTAL THICKNESS.
• RISING DIAPIR STALLS AT DENSITY TRAP AT BASE OF CRUST, PROPAGATES DIKES INTO LOWER CRUST.
② LATER HISTORY: MOON COOLS, LITHOSPHERE THICKNESS INCREASES.
• RISING DIAPIR STALLS AT RHEOLOGICAL TRAP, PROPAGATES DIKE TO SURFACE.
③ EVEN LATER HISTORY: LITHOSPHERE THICKENS FURTHER.
• DIKES PINCH OFF, RISE BOUYANTLY IN MANTLE.
• DIKE PROPAGATES WHEN OVERLYING ROCKS FRACTURE IN BRITTLE MODE.
• EXCESSIVE STRAIN-RATE IMPOSED BY RISING DIAPIR.

Figure 3

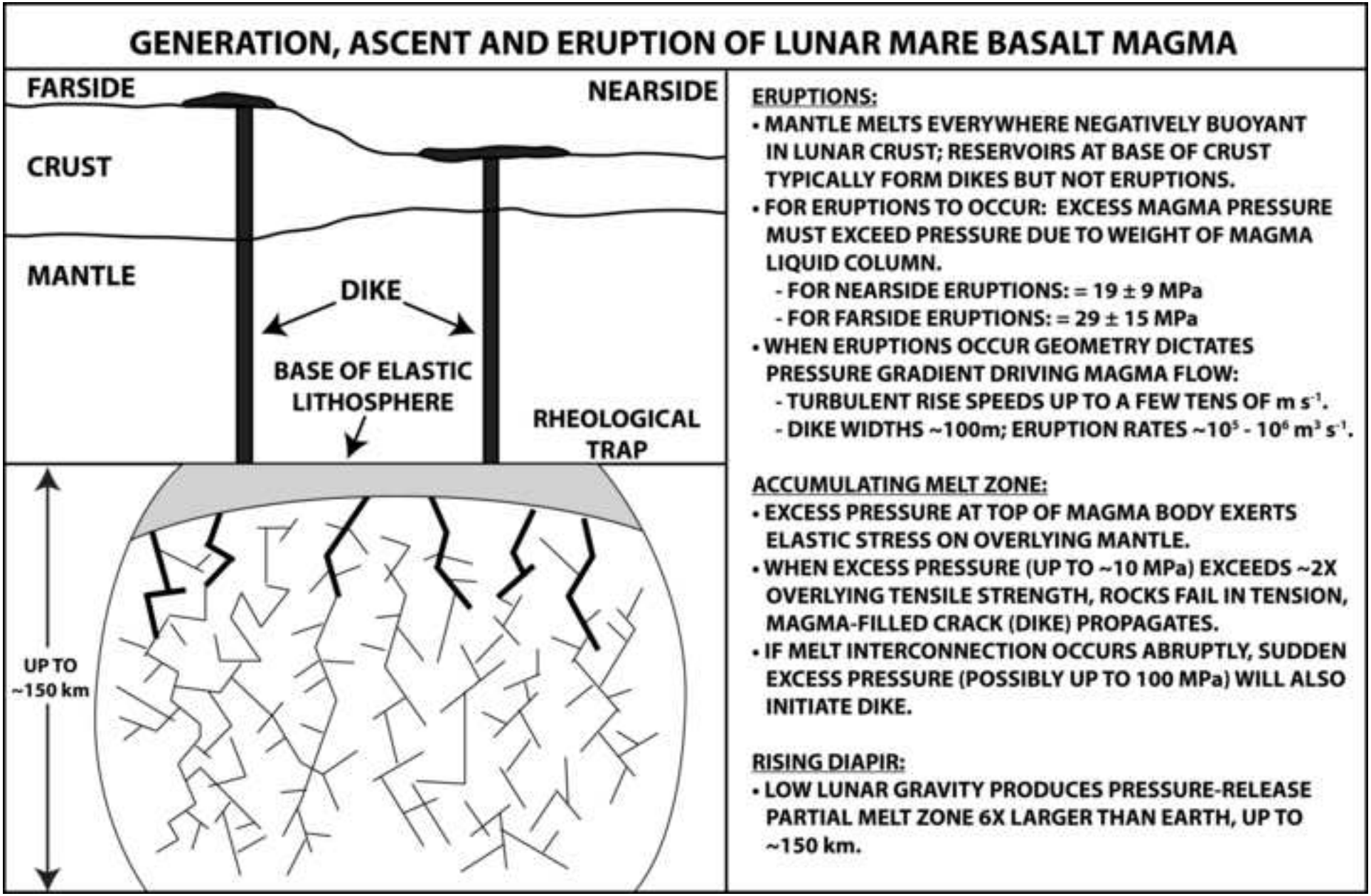
GENERATION, ASCENT AND ERUPTION OF LUNAR MARE BASALT MAGMA
FARSIDE
NEARSIDE
CRUST
MANTLE
DIKE
BASE OF ELASTIC LITHOSPHERE
RHEOLOGICAL TRAP
UP TO ~150 km
ERUPTIONS:
• MANTLE MELTS EVERYWHERE NEGATIVELY BUOYANT IN LUNAR CRUST; RESERVOIRS AT BASE OF CRUST TYPICALLY FORM DIKES BUT NOT ERUPTIONS.
• FOR ERUPTIONS TO OCCUR: EXCESS MAGMA PRESSURE MUST EXCEED PRESSURE DUE TO WEIGHT OF MAGMA LIQUID COLUMN.
- FOR NEARSIDE ERUPTIONS: = 19 ± 9 MPa
- FOR FARSIDE ERUPTIONS: = 29 ± 15 MPa
• WHEN ERUPTIONS OCCUR GEOMETRY DICTATES PRESSURE GRADIENT DRIVING MAGMA FLOW:
- TURBULENT RISE SPEEDS UP TO A FEW TENS OF m s-1.
- DIKE WIDTHS ~100m; ERUPTION RATES ~10^5 - 10^6 m^3 s^-1.
ACCUMULATING MELT ZONE:
• EXCESS PRESSURE AT TOP OF MAGMA BODY EXERTS ELASTIC STRESS ON OVERLYING MANTLE.
• WHEN EXCESS PRESSURE (UP TO ~10 MPa) EXCEEDS ~2X OVERLYING TENSILE STRENGTH, ROCKS FAIL IN TENSION, MAGMA-FILLED CRACK (DIKE) PROPAGATES.
• IF MELT INTERCONNECTION OCCURS ABRUPTLY, SUDDEN EXCESS PRESSURE (POSSIBLY UP TO 100 MPa) WILL ALSO INITIATE DIKE.
RISING DIAPIR:
• LOW LUNAR GRAVITY PRODUCES PRESSURE-RELEASE PARTIAL MELT ZONE 6X LARGER THAN EARTH, UP TO ~150 km.

Figure 4

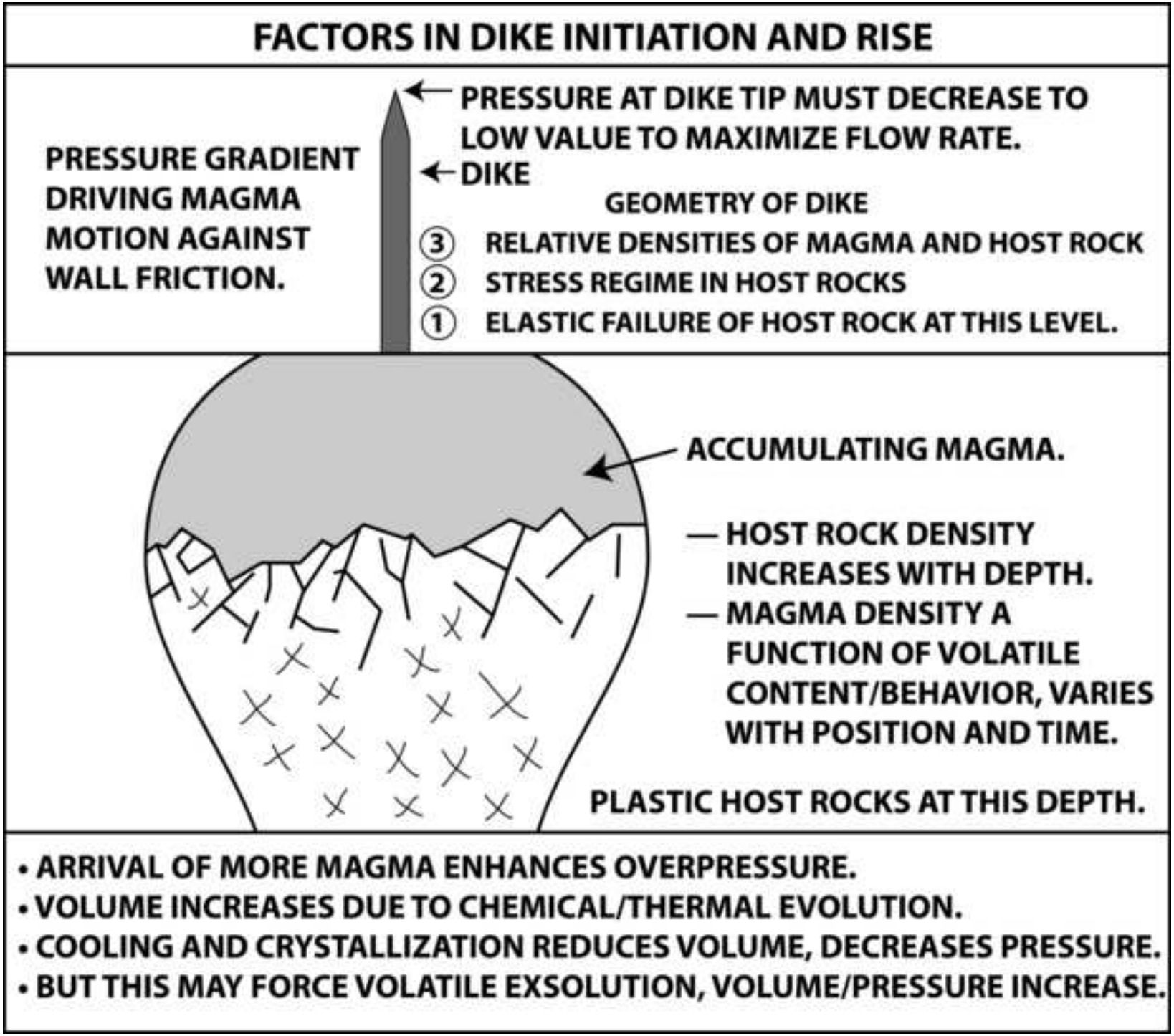
FACTORS IN DIKE INITIATION AND RISE
PRESSURE AT DIKE TIP MUST DECREASE TO LOW VALUE TO MAXIMIZE FLOW RATE.
DIKE
PRESSURE GRADIENT DRIVING MAGMA MOTION AGAINST WALL FRICTION.
GEOMETRY OF DIKE
3 RELATIVE DENSITIES OF MAGMA AND HOST ROCK
2 STRESS REGIME IN HOST ROCKS
1 ELASTIC FAILURE OF HOST ROCK AT THIS LEVEL.
ACCUMULATING MAGMA.
— HOST ROCK DENSITY INCREASES WITH DEPTH.
— MAGMA DENSITY A FUNCTION OF VOLATILE CONTENT/BEHAVIOR, VARIES WITH POSITION AND TIME.
PLASTIC HOST ROCKS AT THIS DEPTH.
• ARRIVAL OF MORE MAGMA ENHANCES OVERPRESSURE.
• VOLUME INCREASES DUE TO CHEMICAL/THERMAL EVOLUTION.
• COOLING AND CRYSTALLIZATION REDUCES VOLUME, DECREASES PRESSURE.
• BUT THIS MAY FORCE VOLATILE EXSOLUTION, VOLUME/PRESSURE INCREASE.

Figure 5abc

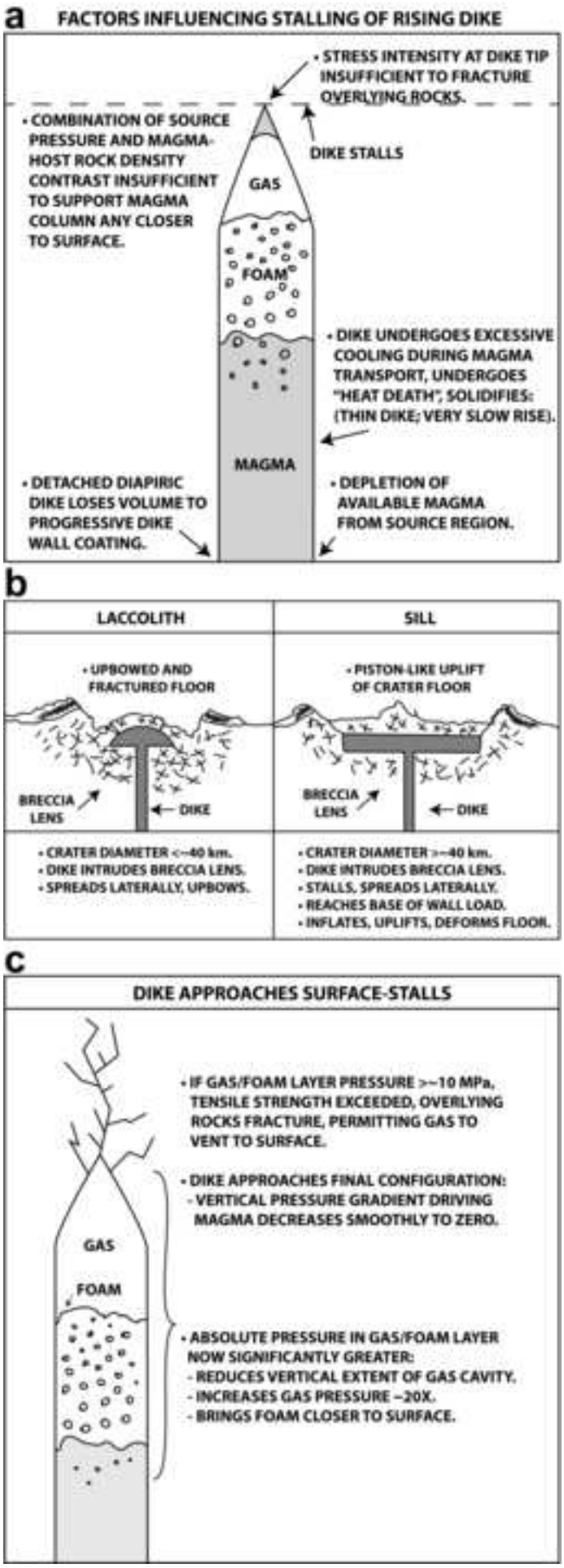
a
FACTORS INFLUENCING STALLING OF RISING DIKE
• STRESS INTENSITY AT DIKE TIP INSUFFICIENT TO FRACTURE OVERLYING ROCKS.
• COMBINATION OF SOURCE PRESSURE AND MAGMA-HOST ROCK DENSITY CONTRAST INSUFFICIENT TO SUPPORT MAGMA COLUMN ANY CLOSER TO SURFACE.
DIKE STALLS
GAS
FOAM
• DIKE UNDERGOES EXCESSIVE COOLING DURING MAGMA TRANSPORT, UNDERGOES "HEAT DEATH", SOLIDIFIES: (THIN DIKE; VERY SLOW RISE).
MAGMA
• DETACHED DIAPIRIC DIKE LOSES VOLUME TO PROGRESSIVE DIKE WALL COATING.
• DEPLETION OF AVAILABLE MAGMA FROM SOURCE REGION.
b
LACCOLITH
SILL
• UPBOWED AND FRACTURED FLOOR
• PISTON-LIKE UPLIFT OF CRATER FLOOR
BRECCIA LENS
DIKE
BRECCIA LENS
DIKE
• CRATER DIAMETER <~40 km.
• DIKE INTRUDES BRECCIA LENS.
• SPREADS LATERALLY, UPBOWS.
• CRATER DIAMETER >~40 km.
• DIKE INTRUDES BRECCIA LENS.
• STALLS, SPREADS LATERALLY.
• REACHES BASE OF WALL LOAD.
• INFLATES, UPLIFTS, DEFORMS FLOOR.
c
DIKE APPROACHES SURFACE-STALLS
• IF GAS/FOAM LAYER PRESSURE >~10 MPa, TENSILE STRENGTH EXCEEDED, OVERLYING ROCKS FRACTURE, PERMITTING GAS TO VENT TO SURFACE.
• DIKE APPROACHES FINAL CONFIGURATION:
- VERTICAL PRESSURE GRADIENT DRIVING MAGMA DECREASES SMOOTHLY TO ZERO.
GAS
FOAM
• ABSOLUTE PRESSURE IN GAS/FOAM LAYER NOW SIGNIFICANTLY GREATER:
- REDUCES VERTICAL EXTENT OF GAS CAVITY.
- INCREASES GAS PRESSURE ~20X.
- BRINGS FOAM CLOSER TO SURFACE.

Figure 5de

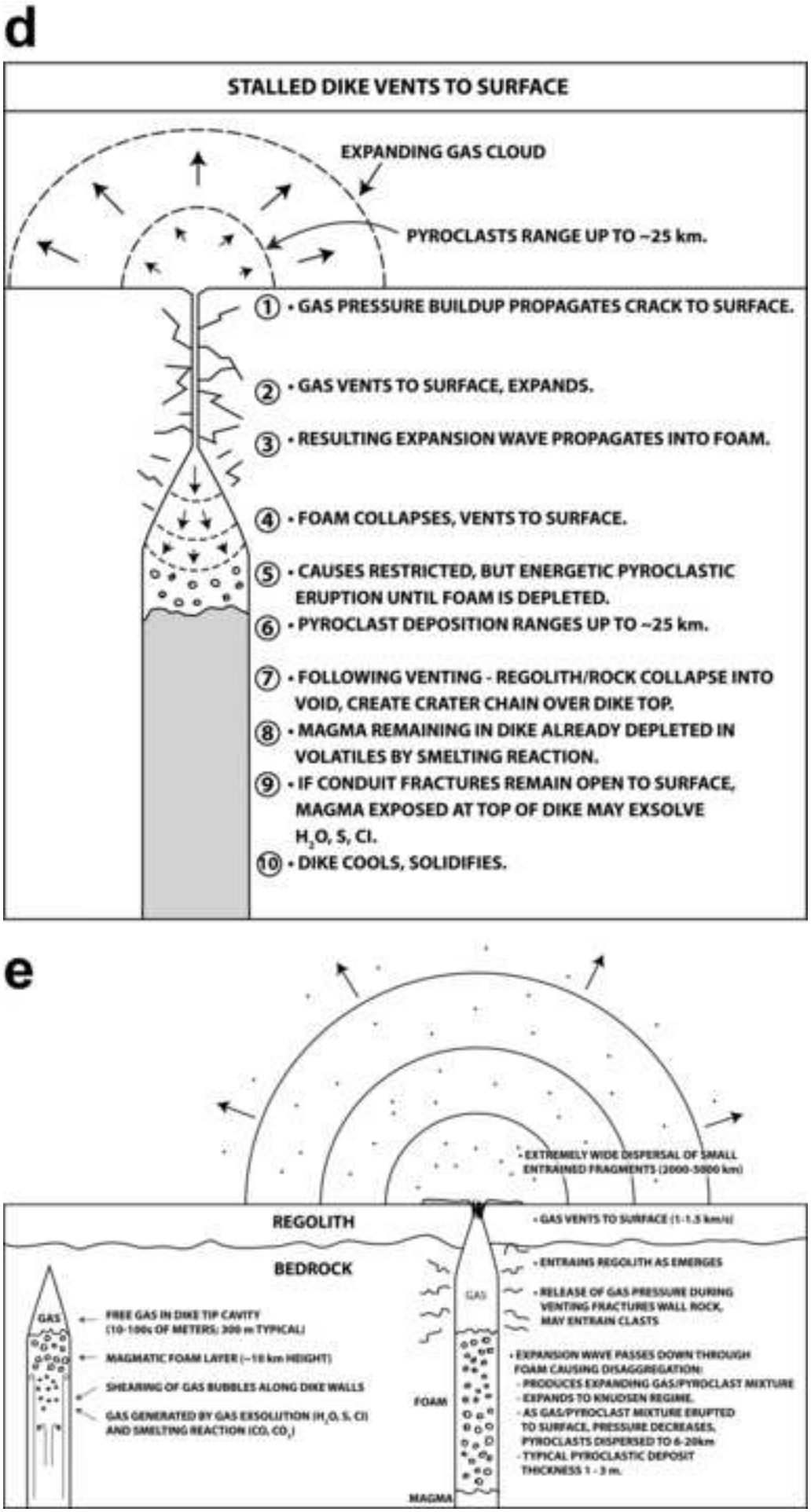
d
STALLED DIKE VENTS TO SURFACE
EXPANDING GAS CLOUD
PYROCLASTS RANGE UP TO ~25 km.
① • GAS PRESSURE BUILDUP PROPAGATES CRACK TO SURFACE.
② • GAS VENTS TO SURFACE, EXPANDS.
③ • RESULTING EXPANSION WAVE PROPAGATES INTO FOAM.
④ • FOAM COLLAPSES, VENTS TO SURFACE.
⑤ • CAUSES RESTRICTED, BUT ENERGETIC PYROCLASTIC ERUPTION UNTIL FOAM IS DEPLETED.
⑥ • PYROCLAST DEPOSITION RANGES UP TO ~25 km.
⑦ • FOLLOWING VENTING - REGOLITH/ROCK COLLAPSE INTO VOID, CREATE CRATER CHAIN OVER DIKE TOP.
⑧ • MAGMA REMAINING IN DIKE ALREADY DEPLETED IN VOLATILES BY SMELTING REACTION.
⑨ • IF CONDUIT FRACTURES REMAIN OPEN TO SURFACE, MAGMA EXPOSED AT TOP OF DIKE MAY EXSOLVE H_2O, S, Cl.
⑩ • DIKE COOLS, SOLIDIFIES.
e
• EXTREMELY WIDE DISPERSAL OF SMALL ENTRAINED FRAGMENTS (2000-5000 km)
REGOLITH
BEDROCK
• GAS VENTS TO SURFACE (1-1.5 km/s)
• ENTRAINS REGOLITH AS EMERGES
• RELEASE OF GAS PRESSURE DURING VENTING FRACTURES WALL ROCK, MAY ENTRAIN CLASTS
GAS
FREE GAS IN DIKE TIP CAVITY (10-100s OF METERS; 300 m TYPICAL)
MAGMATIC FOAM LAYER (~10 km HEIGHT)
SHEARING OF GAS BUBBLES ALONG DIKE WALLS
GAS GENERATED BY GAS EXSOLUTION (H_2O, S, Cl) AND SMELTING REACTION (CO, CO_2)
GAS
FOAM
MAGMA
• EXPANSION WAVE PASSES DOWN THROUGH FOAM CAUSING DISAGGREGATION:
- PRODUCES EXPANDING GAS/PYROCLAST MIXTURE
- EXPANDS TO KNUDSEN REGIME.
- AS GAS/PYROCLAST MIXTURE ERUPTED TO SURFACE, PRESSURE DECREASES, PYROCLASTS DISPERSED TO 6-20km
- TYPICAL PYROCLASTIC DEPOSIT THICKNESS 1 - 3 m.

Figure 5fg

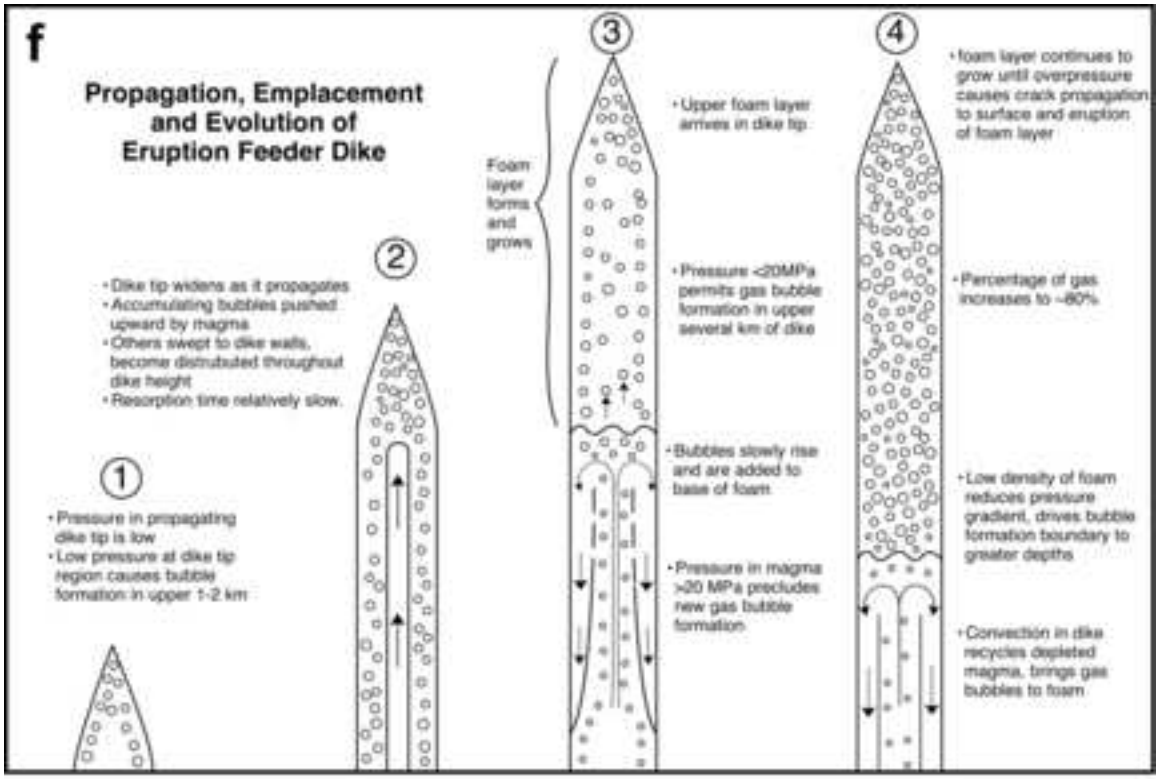
f
Propagation, Emplacement and Evolution of Eruption Feeder Dike
1
• Pressure in propagating dike tip is low
• Low pressure at dike tip region causes bubble formation in upper 1-2 km
2
• Dike tip widens as it propagates
• Accumulating bubbles pushed upward by magma
• Others swept to dike walls, become distributed throughout dike height
• Resorption time relatively slow.
3
Foam layer forms and grows
• Upper foam layer arrives in dike tip
• Pressure <20MPa permits gas bubble formation in upper several km of dike
• Bubbles slowly rise and are added to base of foam
• Pressure in magma >20 MPa precludes new gas bubble formation
4
• foam layer continues to grow until overpressure causes crack propagation to surface and eruption of foam layer
• Percentage of gas increases to ~80%
• Low density of foam reduces pressure gradient, drives bubble formation boundary to greater depths
• Convection in dike recycles depleted magma, brings gas bubbles to foam

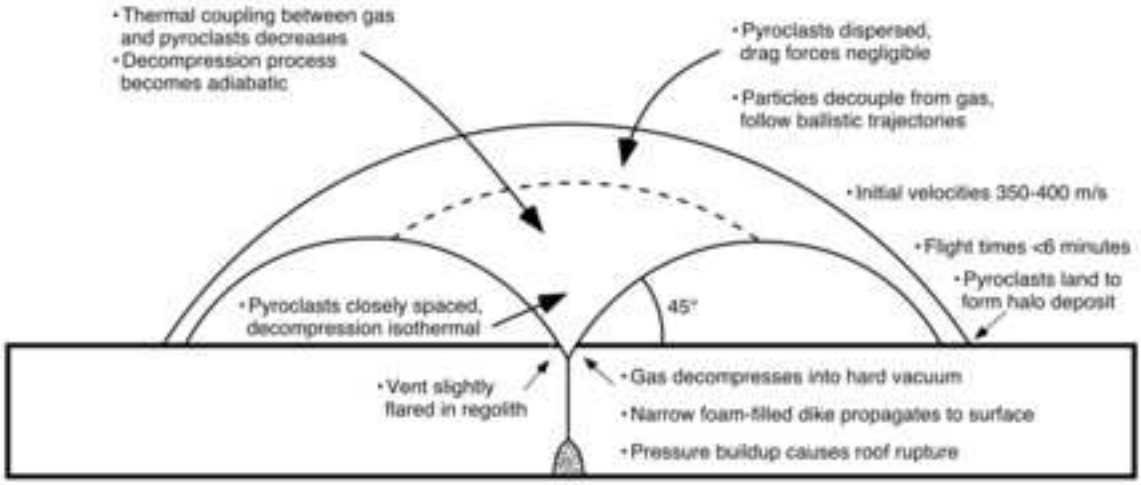
• Thermal coupling between gas and pyroclasts decreases
• Decompression process becomes adiabatic
• Pyroclasts dispersed, drag forces negligible
• Particles decouple from gas, follow ballistic trajectories
• Initial velocities 350-400 m/s
• Flight times <6 minutes
• Pyroclasts land to form halo deposit
• Pyroclasts closely spaced, decompression isothermal
45°
• Vent slightly flared in regolith
• Gas decompresses into hard vacuum
• Narrow foam-filled dike propagates to surface
• Pressure buildup causes roof rupture

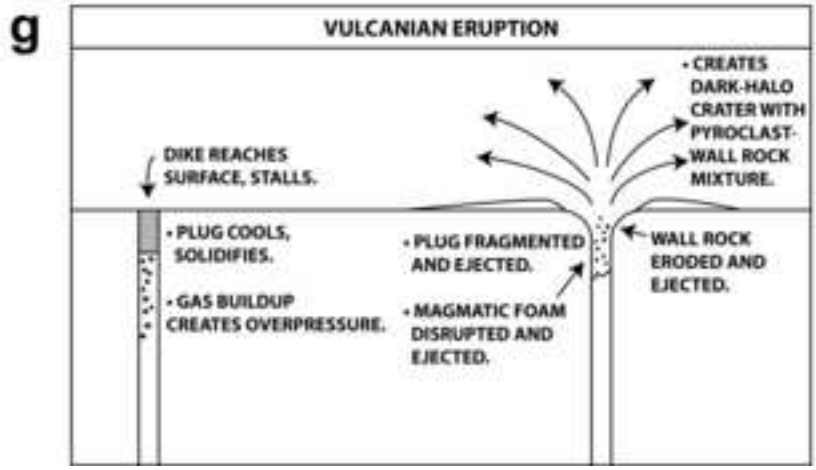
g
VULCANIAN ERUPTION
• CREATES DARK-HALO CRATER WITH PYROCLAST-WALL ROCK MIXTURE.
DIKE REACHES SURFACE, STALLS.
• PLUG COOLS, SOLIDIFIES.
• GAS BUILDUP CREATES OVERPRESSURE.
• PLUG FRAGMENTED AND EJECTED.
• MAGMATIC FOAM DISRUPTED AND EJECTED.
WALL ROCK ERODED AND EJECTED.

Figure 6a-d

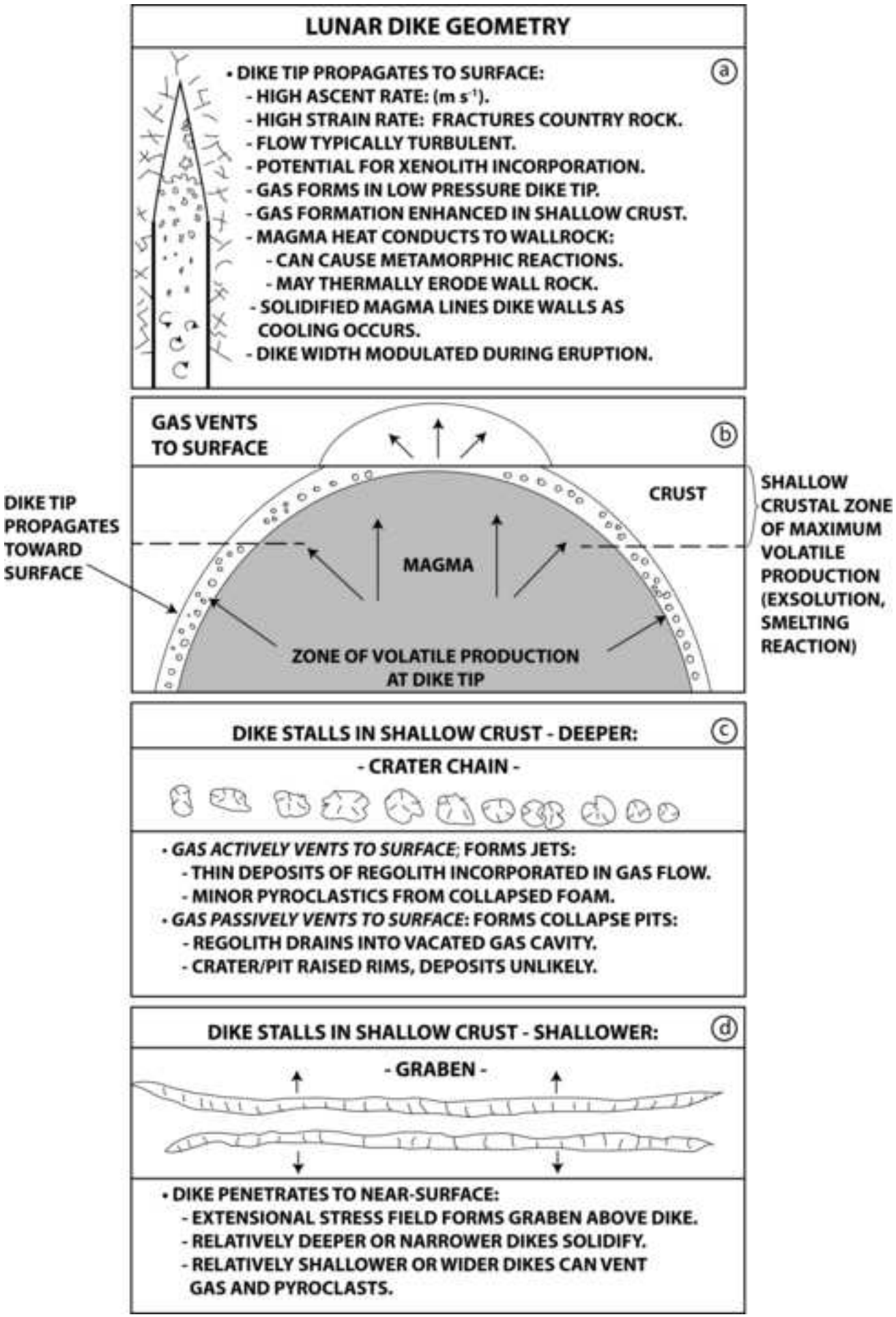
LUNAR DIKE GEOMETRY
a
• DIKE TIP PROPAGATES TO SURFACE:
- HIGH ASCENT RATE: (m s^{-1}).
- HIGH STRAIN RATE: FRACTURES COUNTRY ROCK.
- FLOW TYPICALLY TURBULENT.
- POTENTIAL FOR XENOLITH INCORPORATION.
- GAS FORMS IN LOW PRESSURE DIKE TIP.
- GAS FORMATION ENHANCED IN SHALLOW CRUST.
- MAGMA HEAT CONDUCTS TO WALLROCK:
- CAN CAUSE METAMORPHIC REACTIONS.
- MAY THERMALLY ERODE WALL ROCK.
- SOLIDIFIED MAGMA LINES DIKE WALLS AS COOLING OCCURS.
- DIKE WIDTH MODULATED DURING ERUPTION.
b
GAS VENTS TO SURFACE
CRUST
SHALLOW CRUSTAL ZONE OF MAXIMUM VOLATILE PRODUCTION (EXSOLUTION, SMELTING REACTION)
DIKE TIP PROPAGATES TOWARD SURFACE
MAGMA
ZONE OF VOLATILE PRODUCTION AT DIKE TIP
DIKE STALLS IN SHALLOW CRUST - DEEPER:
c
- CRATER CHAIN -
• GAS ACTIVELY VENTS TO SURFACE; FORMS JETS:
- THIN DEPOSITS OF REGOLITH INCORPORATED IN GAS FLOW.
- MINOR PYROCLASTICS FROM COLLAPSED FOAM.
• GAS PASSIVELY VENTS TO SURFACE: FORMS COLLAPSE PITS:
- REGOLITH DRAINS INTO VACATED GAS CAVITY.
- CRATER/PIT RAISED RIMS, DEPOSITS UNLIKELY.
DIKE STALLS IN SHALLOW CRUST - SHALLOWER:
d
- GRABEN -
• DIKE PENETRATES TO NEAR-SURFACE:
- EXTENSIONAL STRESS FIELD FORMS GRABEN ABOVE DIKE.
- RELATIVELY DEEPER OR NARROWER DIKES SOLIDIFY.
- RELATIVELY SHALLOWER OR WIDER DIKES CAN VENT GAS AND PYROCLASTS.

Figure 6e

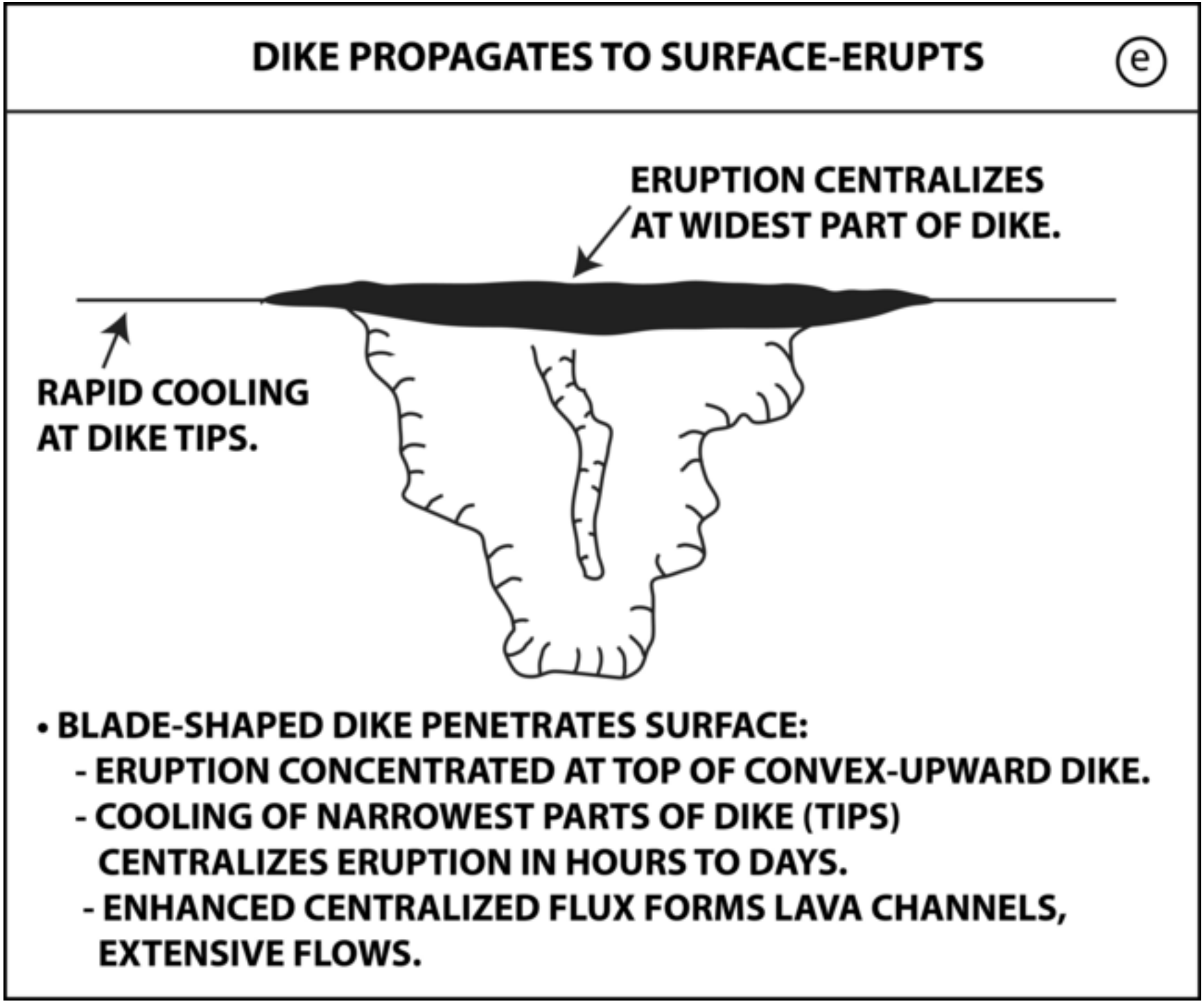
DIKE PROPAGATES TO SURFACE-ERUPTS
e
ERUPTION CENTRALIZES
AT WIDEST PART OF DIKE.
RAPID COOLING
AT DIKE TIPS.
• BLADE-SHAPED DIKE PENETRATES SURFACE:
- ERUPTION CONCENTRATED AT TOP OF CONVEX-UPWARD DIKE.
- COOLING OF NARROWEST PARTS OF DIKE (TIPS)
CENTRALIZES ERUPTION IN HOURS TO DAYS.
- ENHANCED CENTRALIZED FLUX FORMS LAVA CHANNELS,
EXTENSIVE FLOWS.

Figure 7abc

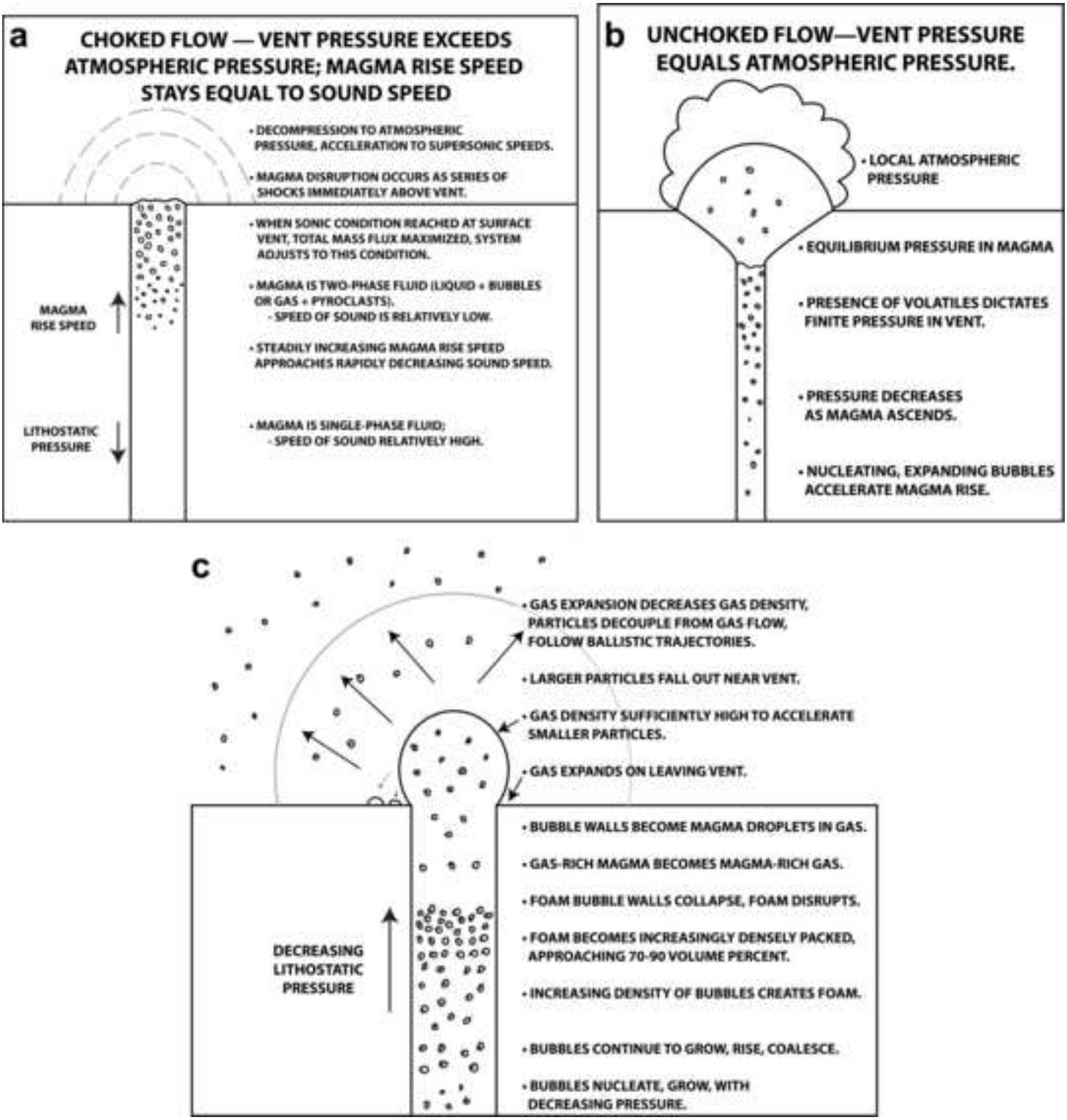
a
CHOKED FLOW — VENT PRESSURE EXCEEDS ATMOSPHERIC PRESSURE; MAGMA RISE SPEED STAYS EQUAL TO SOUND SPEED
• DECOMPRESSION TO ATMOSPHERIC PRESSURE, ACCELERATION TO SUPERSONIC SPEEDS.
• MAGMA DISRUPTION OCCURS AS SERIES OF SHOCKS IMMEDIATELY ABOVE VENT.
• WHEN SONIC CONDITION REACHED AT SURFACE VENT, TOTAL MASS FLUX MAXIMIZED, SYSTEM ADJUSTS TO THIS CONDITION.
• MAGMA IS TWO-PHASE FLUID (LIQUID + BUBBLES OR GAS + PYROCLASTS).
- SPEED OF SOUND IS RELATIVELY LOW.
• STEADILY INCREASING MAGMA RISE SPEED APPROACHES RAPIDLY DECREASING SOUND SPEED.
• MAGMA IS SINGLE-PHASE FLUID;
- SPEED OF SOUND RELATIVELY HIGH.
MAGMA RISE SPEED
LITHOSTATIC PRESSURE
b
UNCHOKED FLOW—VENT PRESSURE EQUALS ATMOSPHERIC PRESSURE.
• LOCAL ATMOSPHERIC PRESSURE
• EQUILIBRIUM PRESSURE IN MAGMA
• PRESENCE OF VOLATILES DICTATES FINITE PRESSURE IN VENT.
• PRESSURE DECREASES AS MAGMA ASCENDS.
• NUCLEATING, EXPANDING BUBBLES ACCELERATE MAGMA RISE.
c
• GAS EXPANSION DECREASES GAS DENSITY, PARTICLES DECOUPLE FROM GAS FLOW, FOLLOW BALLISTIC TRAJECTORIES.
• LARGER PARTICLES FALL OUT NEAR VENT.
• GAS DENSITY SUFFICIENTLY HIGH TO ACCELERATE SMALLER PARTICLES.
• GAS EXPANDS ON LEAVING VENT.
• BUBBLE WALLS BECOME MAGMA DROPLETS IN GAS.
• GAS-RICH MAGMA BECOMES MAGMA-RICH GAS.
• FOAM BUBBLE WALLS COLLAPSE, FOAM DISRUPTS.
• FOAM BECOMES INCREASINGLY DENSELY PACKED, APPROACHING 70-90 VOLUME PERCENT.
• INCREASING DENSITY OF BUBBLES CREATES FOAM.
• BUBBLES CONTINUE TO GROW, RISE, COALESCE.
• BUBBLES NUCLEATE, GROW, WITH DECREASING PRESSURE.
DECREASING LITHOSTATIC PRESSURE

Figure 8

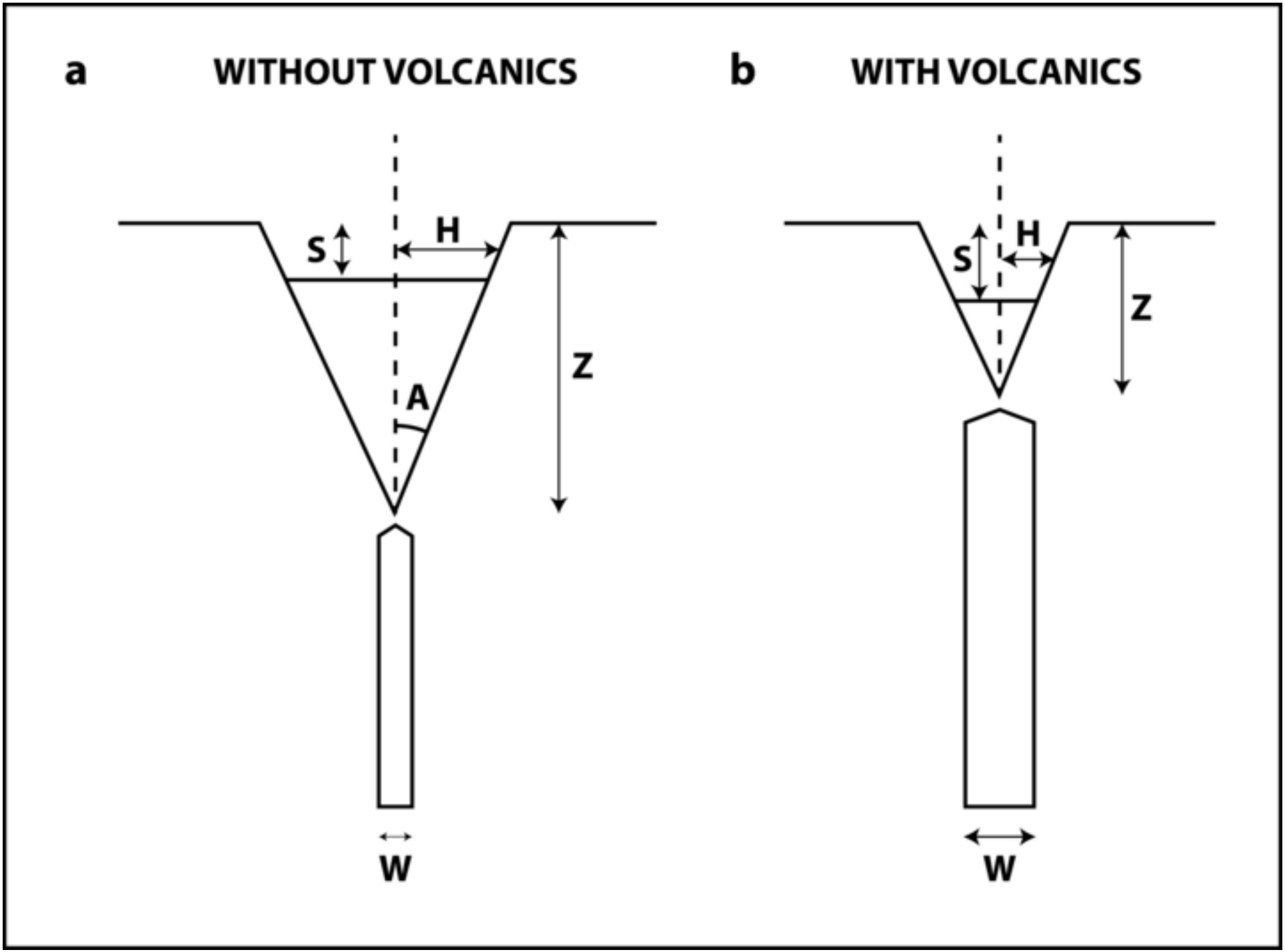

Figure 9abc

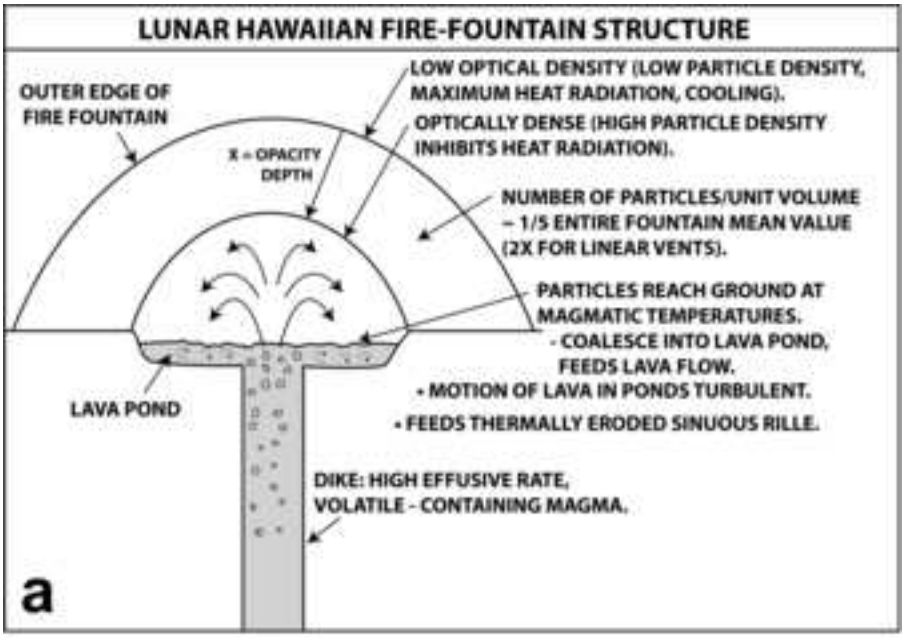
LUNAR HAWAIIAN FIRE-FOUNTAIN STRUCTURE
OUTER EDGE OF FIRE FOUNTAIN
LOW OPTICAL DENSITY (LOW PARTICLE DENSITY, MAXIMUM HEAT RADIATION, COOLING).
OPTICALLY DENSE (HIGH PARTICLE DENSITY INHIBITS HEAT RADIATION).
X = OPACITY DEPTH
NUMBER OF PARTICLES/UNIT VOLUME = 1/5 ENTIRE FOUNTAIN MEAN VALUE (2X FOR LINEAR VENTS).
PARTICLES REACH GROUND AT MAGMATIC TEMPERATURES.
- COALESCE INTO LAVA POND, FEEDS LAVA FLOW.
• MOTION OF LAVA IN PONDS TURBULENT.
• FEEDS THERMALLY ERODED SINUOUS RILLE.
LAVA POND
DIKE: HIGH EFFUSIVE RATE, VOLATILE - CONTAINING MAGMA.
a

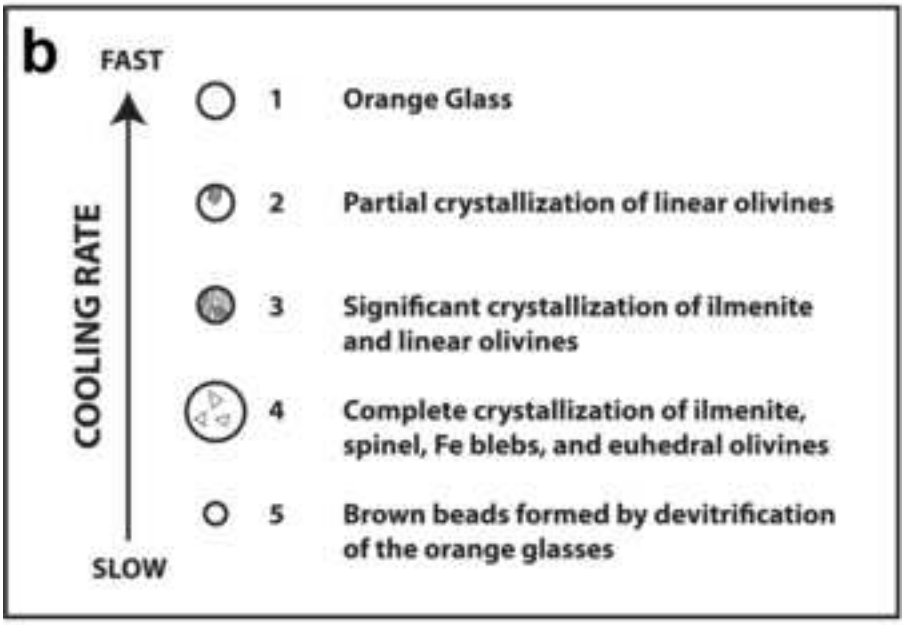
b
FAST
COOLING RATE
SLOW
1 Orange Glass
2 Partial crystallization of linear olivines
3 Significant crystallization of ilmenite and linear olivines
4 Complete crystallization of ilmenite, spinel, Fe blebs, and euhedral olivines
5 Brown beads formed by devitrification of the orange glasses

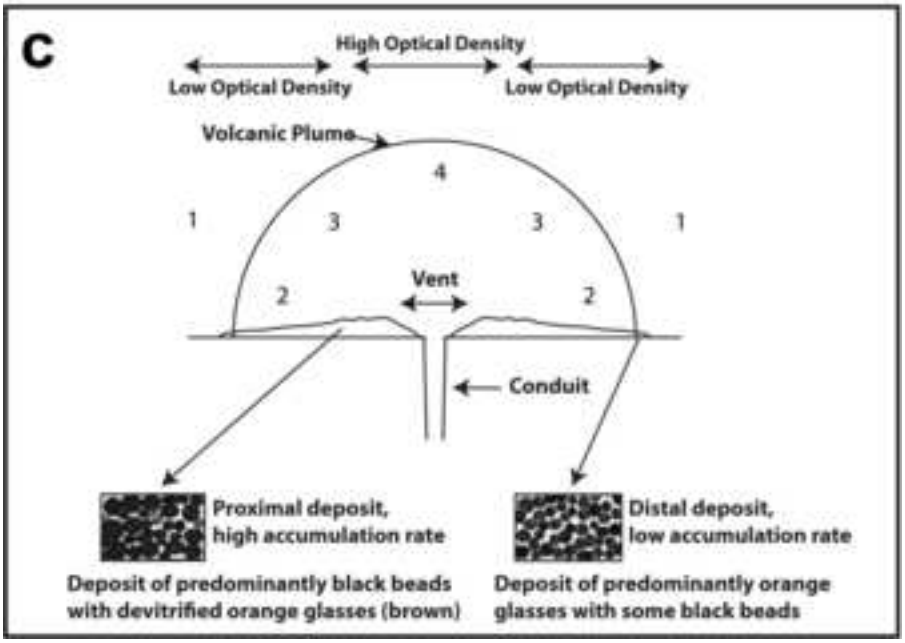
c
High Optical Density
Low Optical Density
Low Optical Density
Volcanic Plume
4
1
3
3
1
2
Vent
2
Conduit
Proximal deposit, high accumulation rate
Distal deposit, low accumulation rate
Deposit of predominantly black beads with devitrified orange glasses (brown)
Deposit of predominantly orange glasses with some black beads

Figure 10

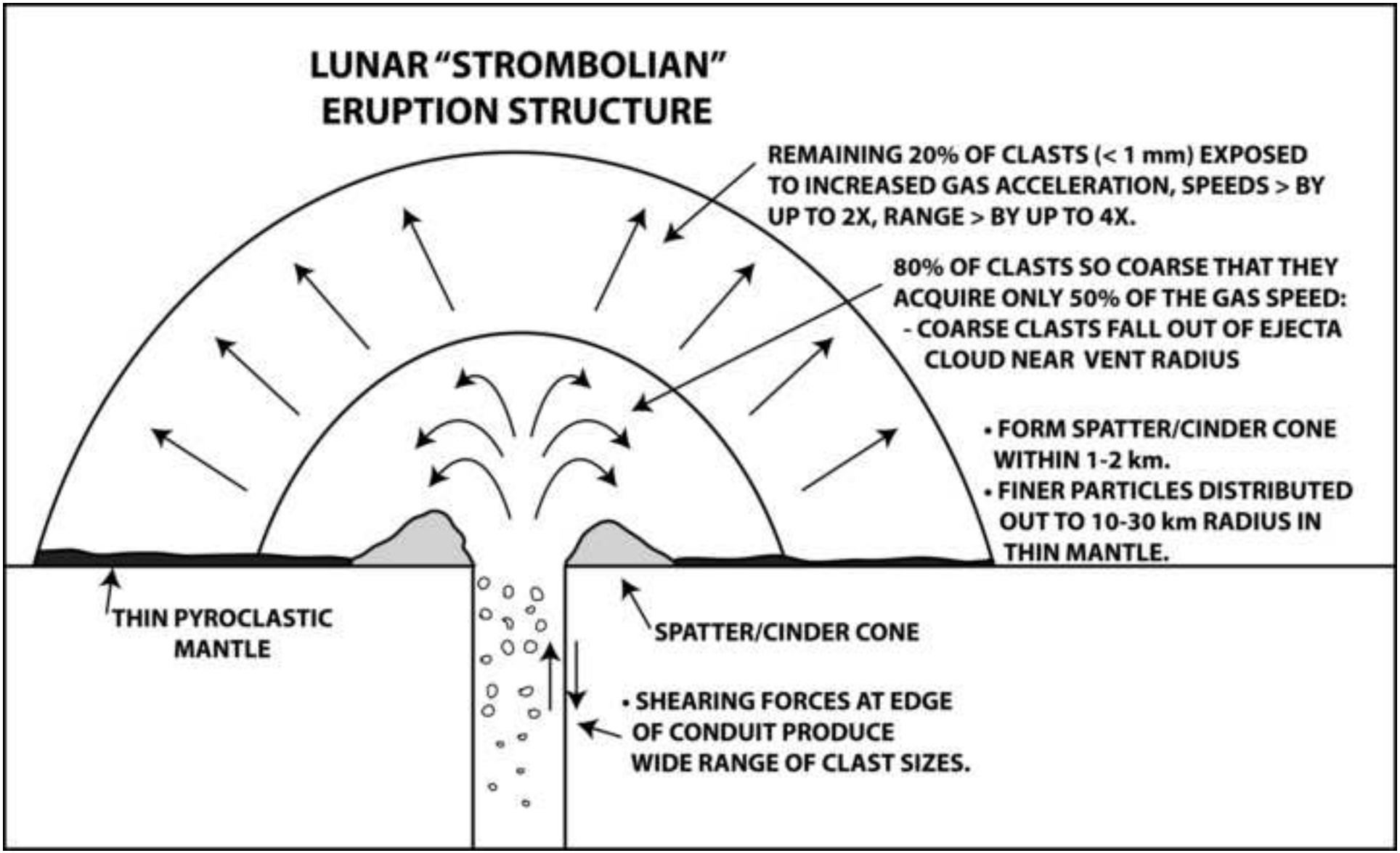
LUNAR "STROMBOLIAN"
ERUPTION STRUCTURE
REMAINING 20% OF CLASTS (< 1 mm) EXPOSED TO INCREASED GAS ACCELERATION, SPEEDS > BY UP TO 2X, RANGE > BY UP TO 4X.
80% OF CLASTS SO COARSE THAT THEY ACQUIRE ONLY 50% OF THE GAS SPEED:
- COARSE CLASTS FALL OUT OF EJECTA CLOUD NEAR VENT RADIUS
• FORM SPATTER/CINDER CONE WITHIN 1-2 km.
• FINER PARTICLES DISTRIBUTED OUT TO 10-30 km RADIUS IN THIN MANTLE.
THIN PYROCLASTIC MANTLE
SPATTER/CINDER CONE
• SHEARING FORCES AT EDGE OF CONDUIT PRODUCE WIDE RANGE OF CLAST SIZES.

Figure 11ab

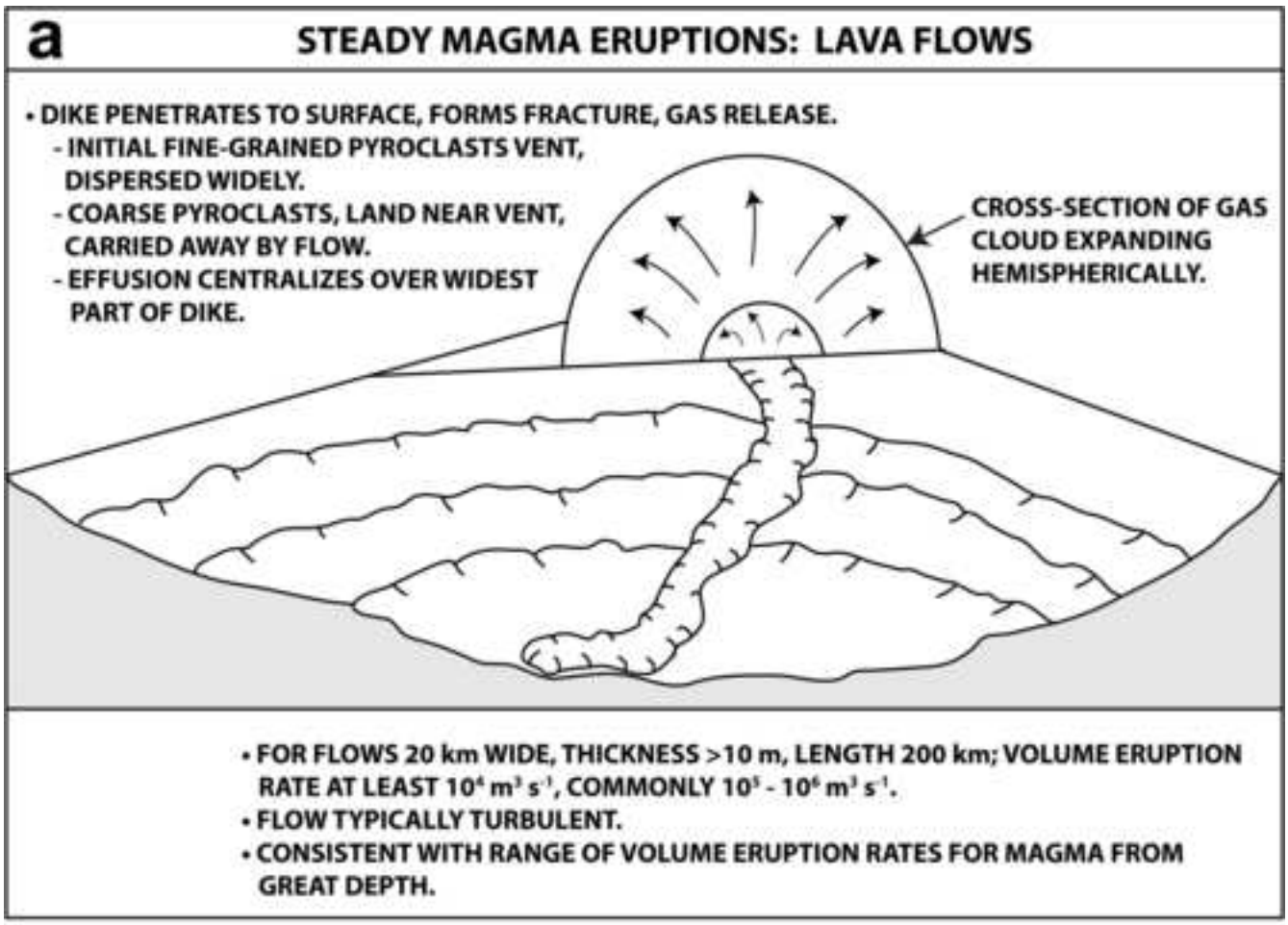
a
STEADY MAGMA ERUPTIONS: LAVA FLOWS
• DIKE PENETRATES TO SURFACE, FORMS FRACTURE, GAS RELEASE.
- INITIAL FINE-GRAINED PYROCLASTS VENT, DISPERSED WIDELY.
- COARSE PYROCLASTS, LAND NEAR VENT, CARRIED AWAY BY FLOW.
- EFFUSION CENTRALIZES OVER WIDEST PART OF DIKE.
CROSS-SECTION OF GAS CLOUD EXPANDING HEMISPHERICALLY.
• FOR FLOWS 20 km WIDE, THICKNESS >10 m, LENGTH 200 km; VOLUME ERUPTION RATE AT LEAST 10^4 m^3 s^{-1}, COMMONLY 10^5 - 10^6 m^3 s^{-1}.
• FLOW TYPICALLY TURBULENT.
• CONSISTENT WITH RANGE OF VOLUME ERUPTION RATES FOR MAGMA FROM GREAT DEPTH.

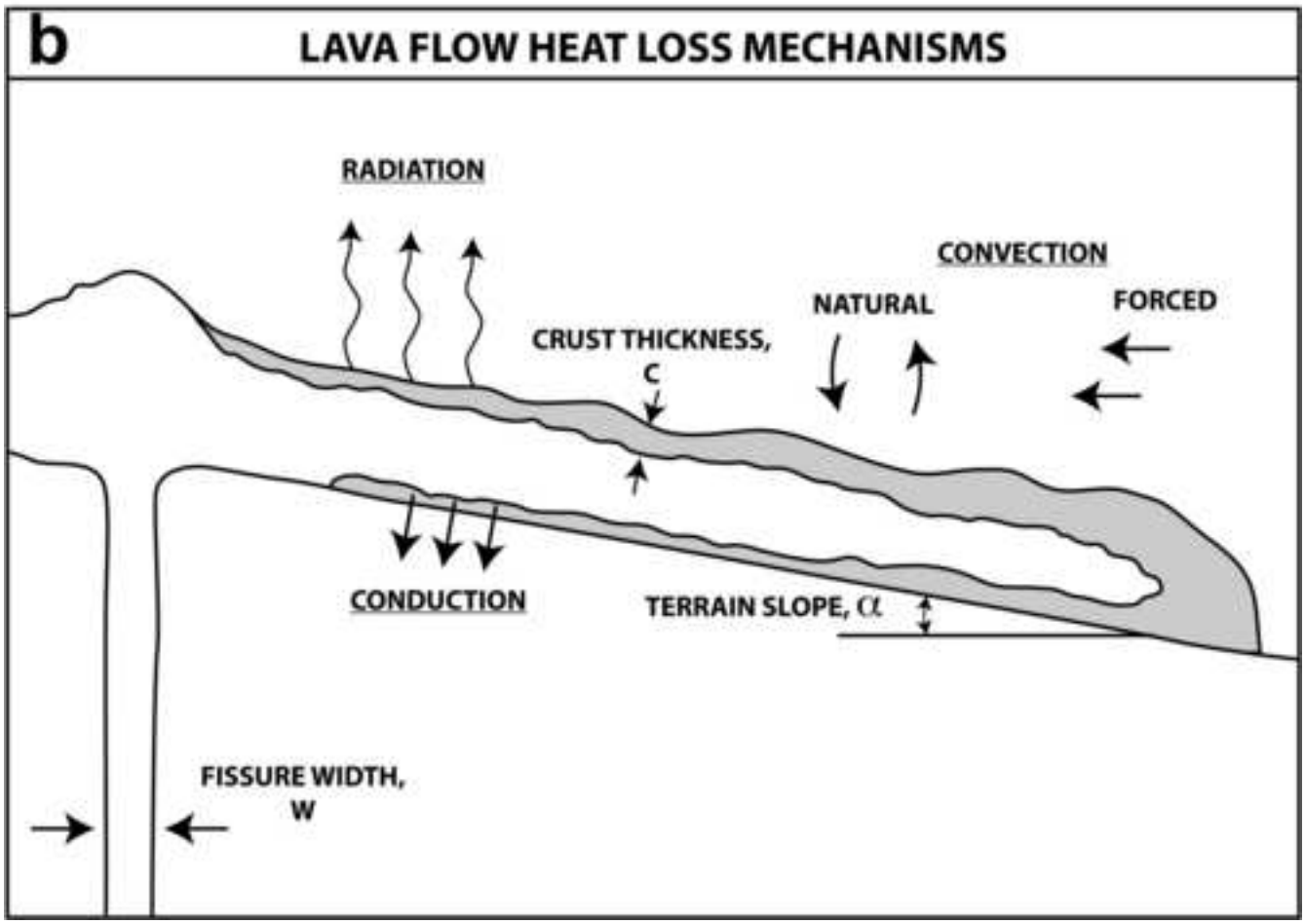
b
LAVA FLOW HEAT LOSS MECHANISMS
RADIATION
CONVECTION
NATURAL
FORCED
CRUST THICKNESS, C
CONDUCTION
TERRAIN SLOPE, α
FISSURE WIDTH, W

Figure 12abc

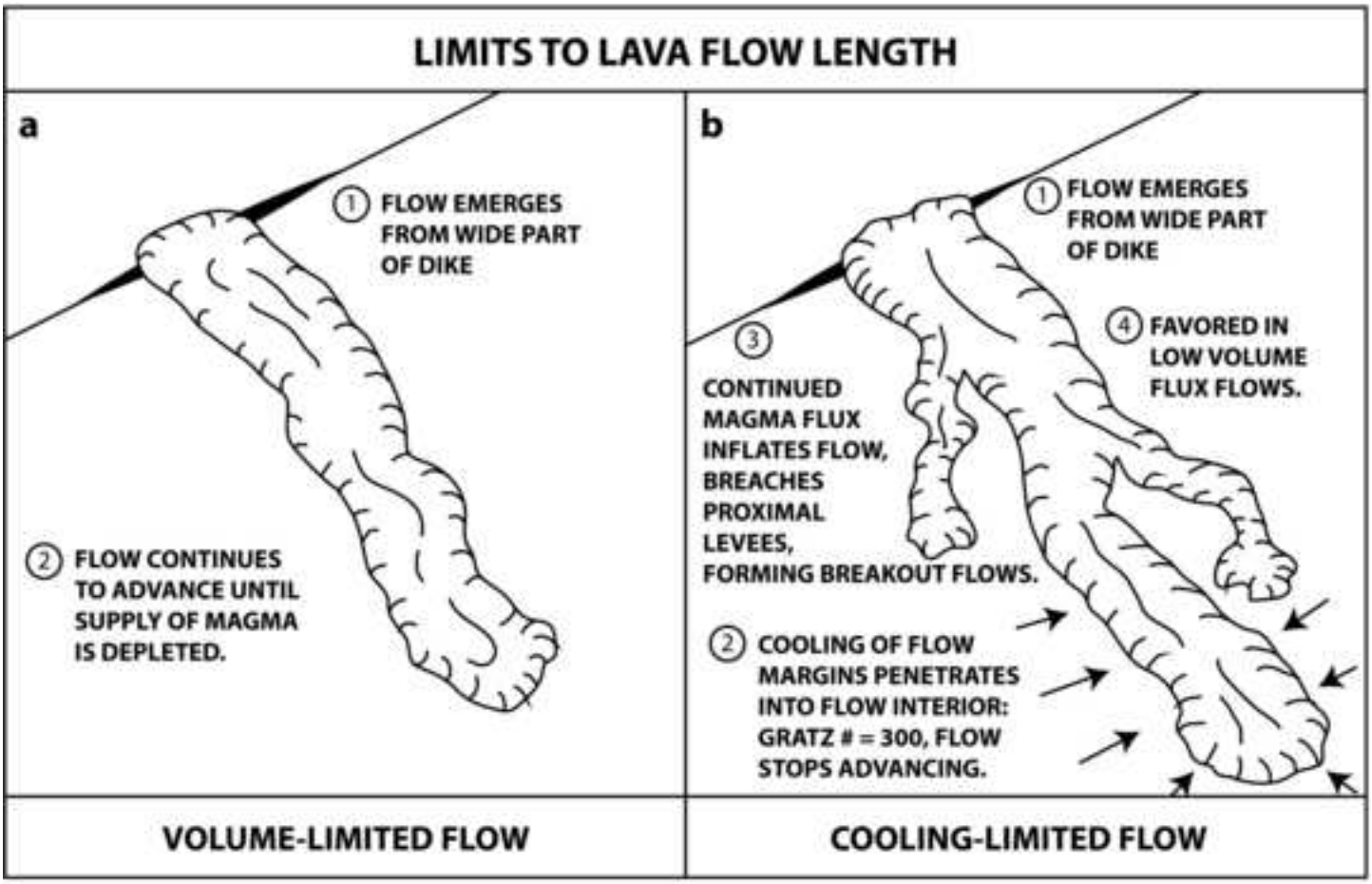

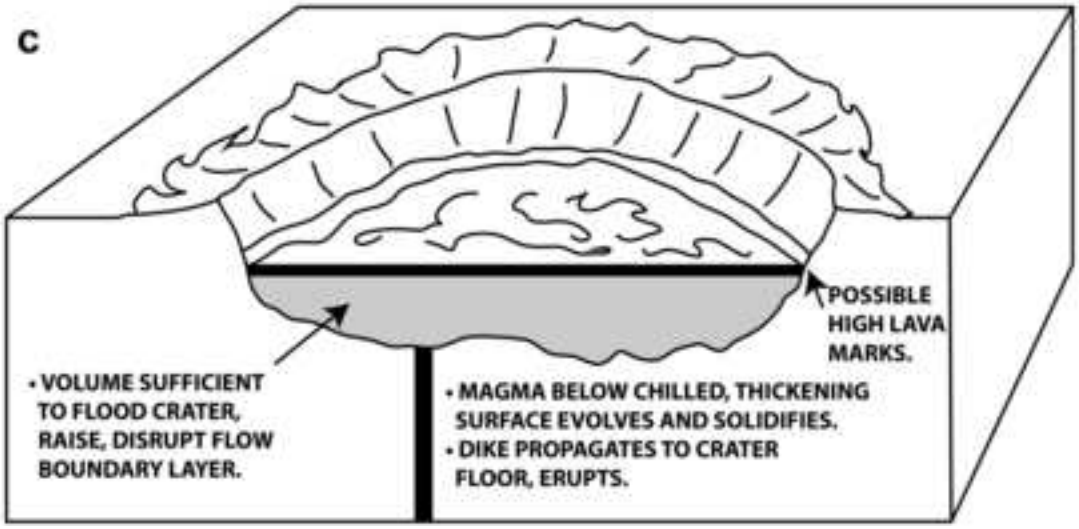

Figure 13ab

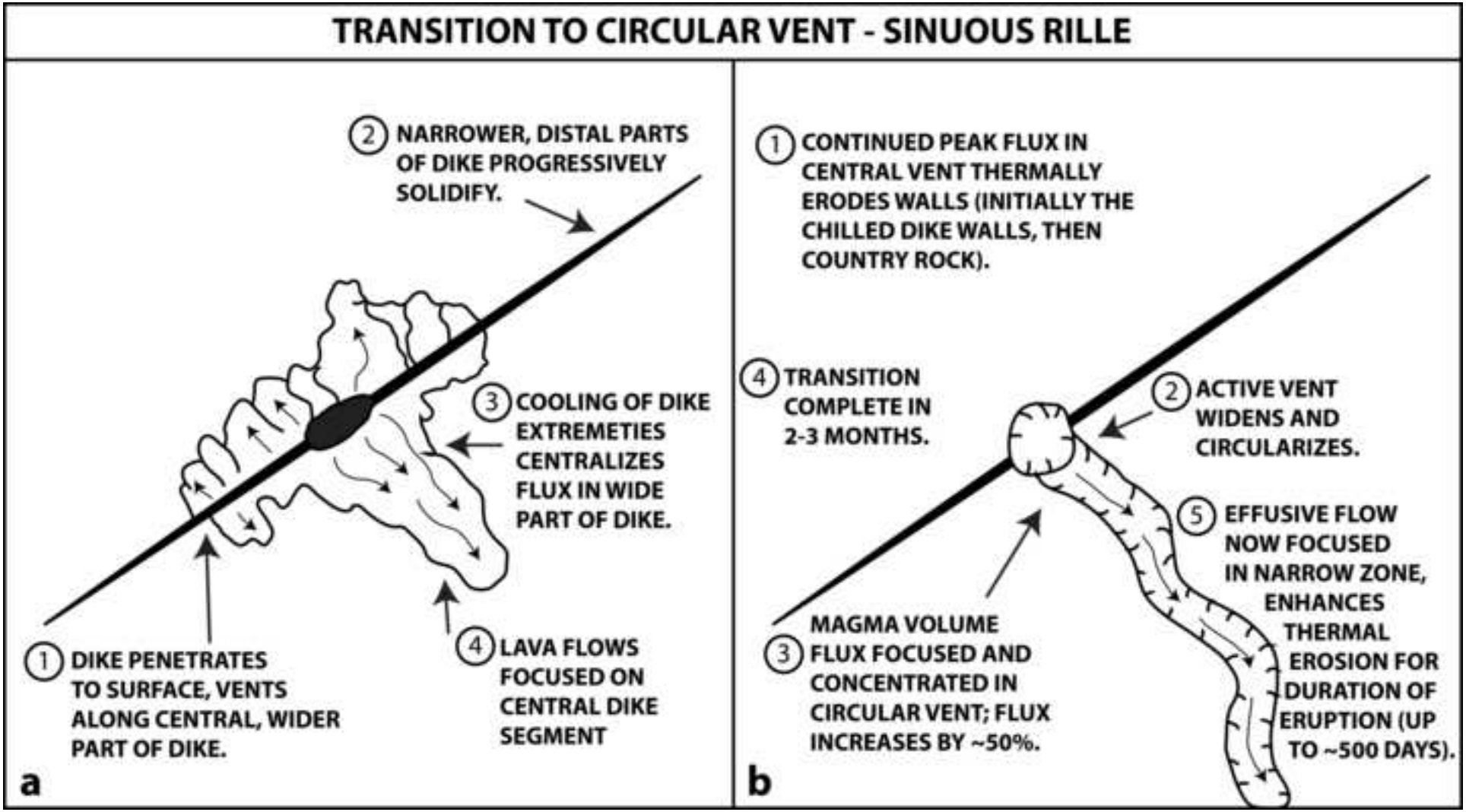
TRANSITION TO CIRCULAR VENT - SINUOUS RILLE
2 NARROWER, DISTAL PARTS OF DIKE PROGRESSIVELY SOLIDIFY.
3 COOLING OF DIKE EXTREMETIES CENTRALIZES FLUX IN WIDE PART OF DIKE.
1 DIKE PENETRATES TO SURFACE, VENTS ALONG CENTRAL, WIDER PART OF DIKE.
4 LAVA FLOWS FOCUSED ON CENTRAL DIKE SEGMENT
a
1 CONTINUED PEAK FLUX IN CENTRAL VENT THERMALLY ERODES WALLS (INITIALLY THE CHILLED DIKE WALLS, THEN COUNTRY ROCK).
4 TRANSITION COMPLETE IN 2-3 MONTHS.
2 ACTIVE VENT WIDENS AND CIRCULARIZES.
5 EFFUSIVE FLOW NOW FOCUSED IN NARROW ZONE, ENHANCES THERMAL EROSION FOR DURATION OF ERUPTION (UP TO ~500 DAYS).
3 MAGMA VOLUME FLUX FOCUSED AND CONCENTRATED IN CIRCULAR VENT; FLUX INCREASES BY ~50%.
b

Figure 14

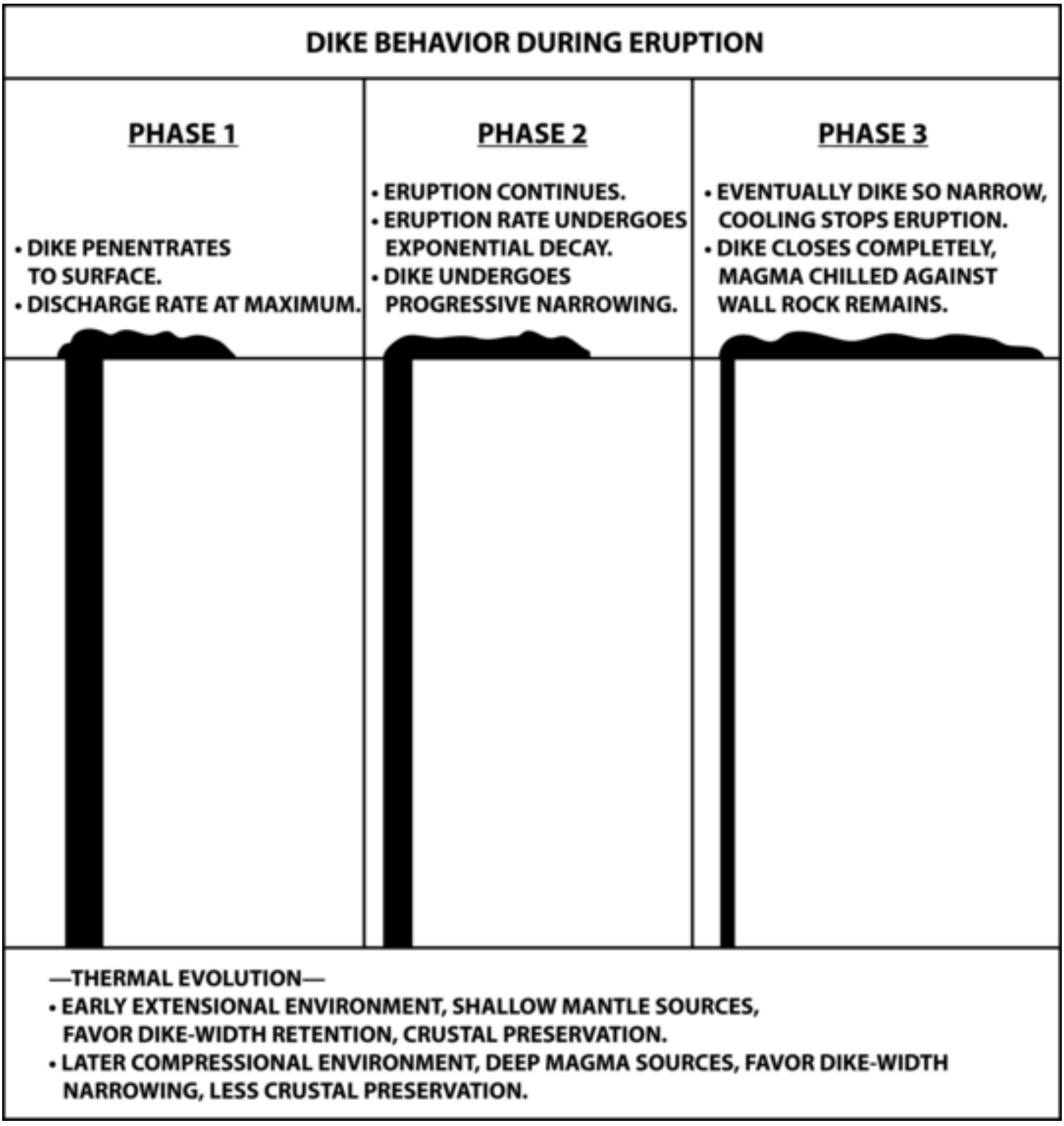
DIKE BEHAVIOR DURING ERUPTION
PHASE 1
• DIKE PENENTRATES TO SURFACE.
• DISCHARGE RATE AT MAXIMUM.
PHASE 2
• ERUPTION CONTINUES.
• ERUPTION RATE UNDERGOES EXPONENTIAL DECAY.
• DIKE UNDERGOES PROGRESSIVE NARROWING.
PHASE 3
• EVENTUALLY DIKE SO NARROW, COOLING STOPS ERUPTION.
• DIKE CLOSES COMPLETELY, MAGMA CHILLED AGAINST WALL ROCK REMAINS.
—THERMAL EVOLUTION—
• EARLY EXTENSIONAL ENVIRONMENT, SHALLOW MANTLE SOURCES, FAVOR DIKE-WIDTH RETENTION, CRUSTAL PRESERVATION.
• LATER COMPRESSIONAL ENVIRONMENT, DEEP MAGMA SOURCES, FAVOR DIKE-WIDTH NARROWING, LESS CRUSTAL PRESERVATION.

Figure 15

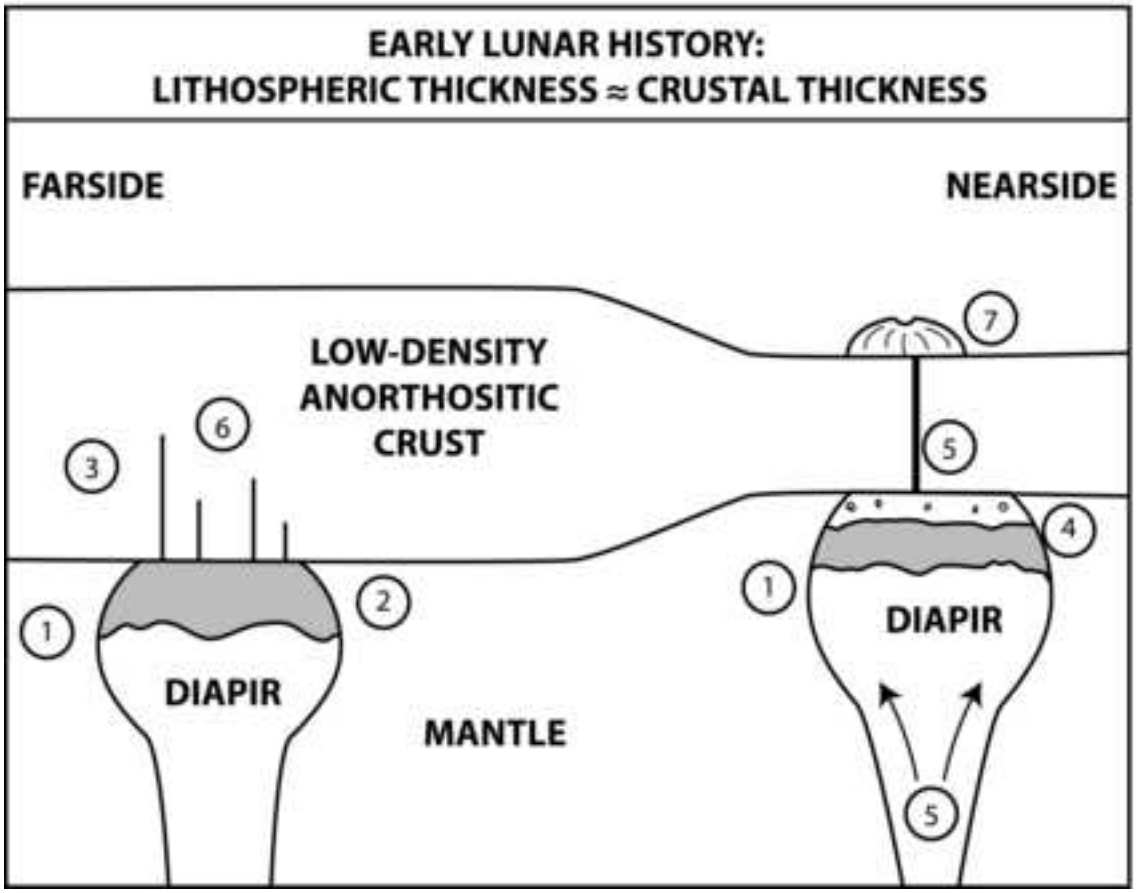

1. DIAPIRS RISE TO BASE OF CRUST: PRESSURE RELEASE MELTING CREATES MAGMA RESERVOIR.
2. EXCESS PRESSURE LOW IN MAGMA RESERVOIRS: DUE TO SHALLOW DEPTHS OF SUB-CRUSTAL RESERVOIR, RELATIVELY LOW DENSITY OF OVERLYING CRUST.
3. DIKES UNLIKELY TO BREACH SURFACE.
4. MAGMA RESERVOIR STABLE AT BASE OF CRUST:
   - ENCOURAGES DIFFERENTIATION OF MAGMA RESERVOIR.
   - FAVORS HEATING, METAMORPHISM AND MELTING OF OVERLYING CRUST.
5. RESERVOIR OVERPRESSURIZATION DUE TO DIFFERENTIATION/METAMORPHISM AND DIAPIRIC REPLENISHMENT FROM DEPTH.
6. DENSER BASALTIC MAGMAS FORM DIKES IN LOWER CRUST.
7. LESS DENSE SILICIC MAGMAS PROPAGATE DIKES TO SURFACE, FORM STEEP-SIDED DOMES.

Figure 16

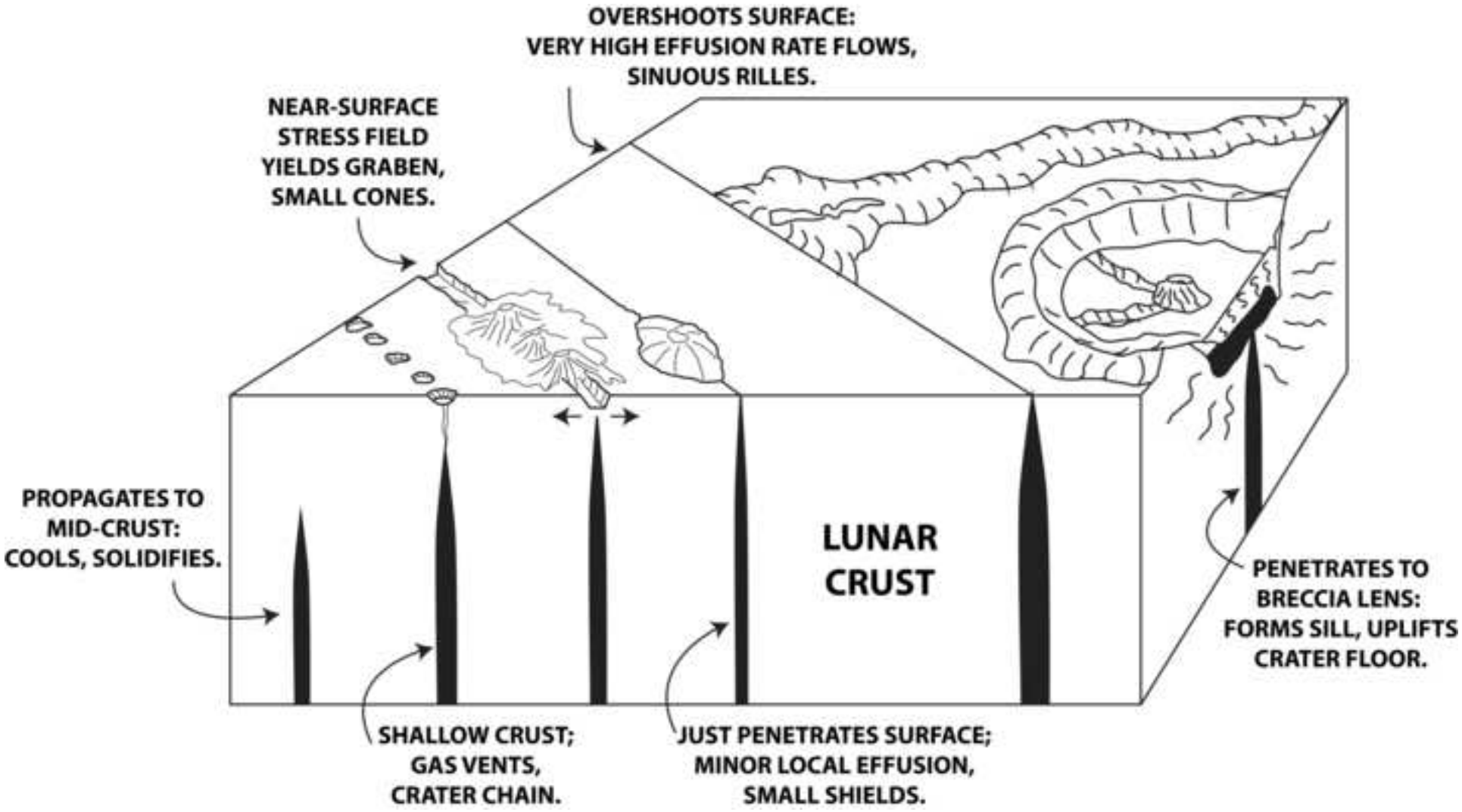
OVERSHOOTS SURFACE:
VERY HIGH EFFUSION RATE FLOWS,
SINUOUS RILLES.
NEAR-SURFACE
STRESS FIELD
YIELDS GRABEN,
SMALL CONES.
PROPAGATES TO
MID-CRUST:
COOLS, SOLIDIFIES.
LUNAR
CRUST
PENETRATES TO
BRECCIA LENS:
FORMS SILL, UPLIFTS
CRATER FLOOR.
SHALLOW CRUST;
GAS VENTS,
CRATER CHAIN.
JUST PENETRATES SURFACE;
MINOR LOCAL EFFUSION,
SMALL SHIELDS.

Figure 17

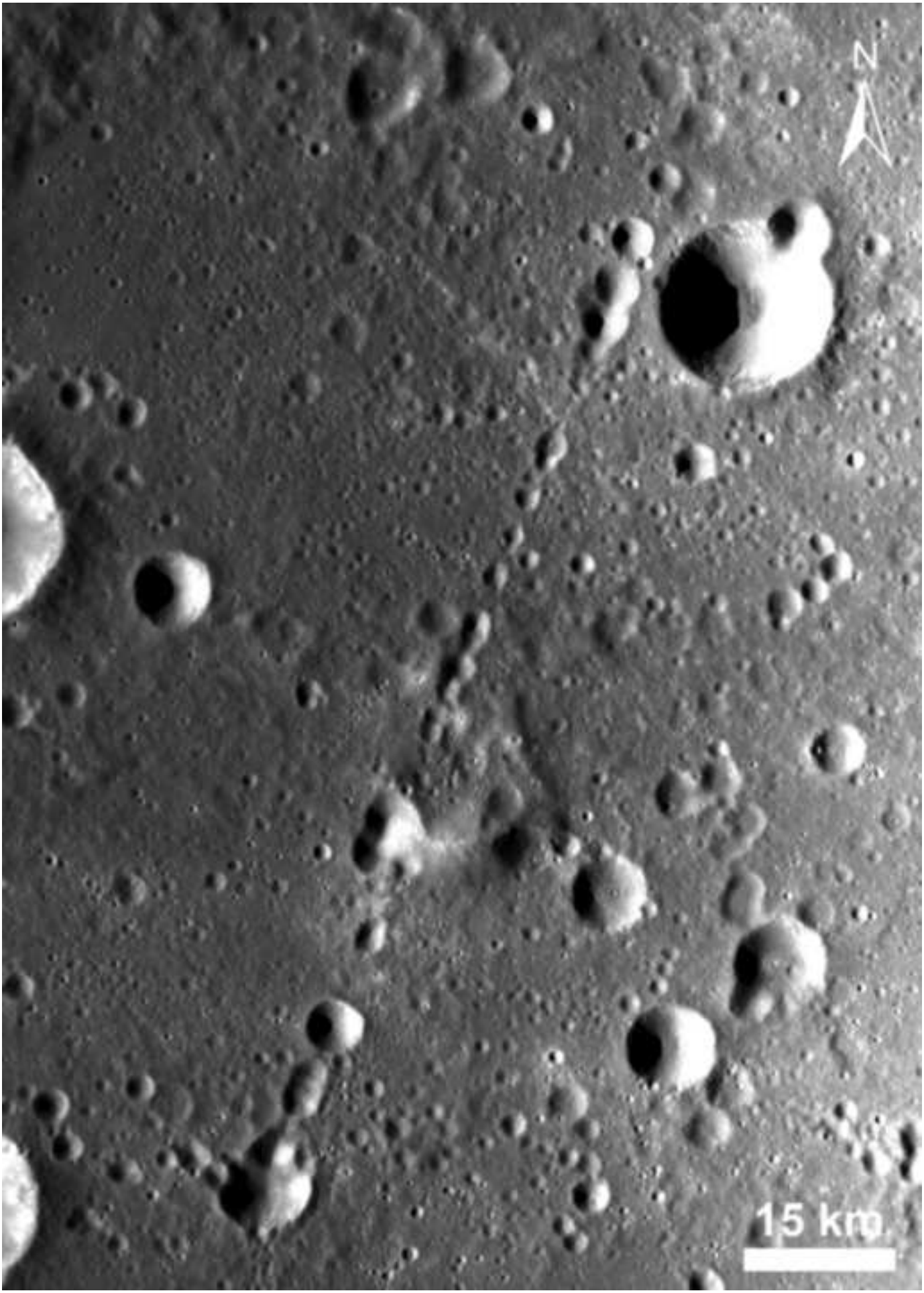

Figure 18

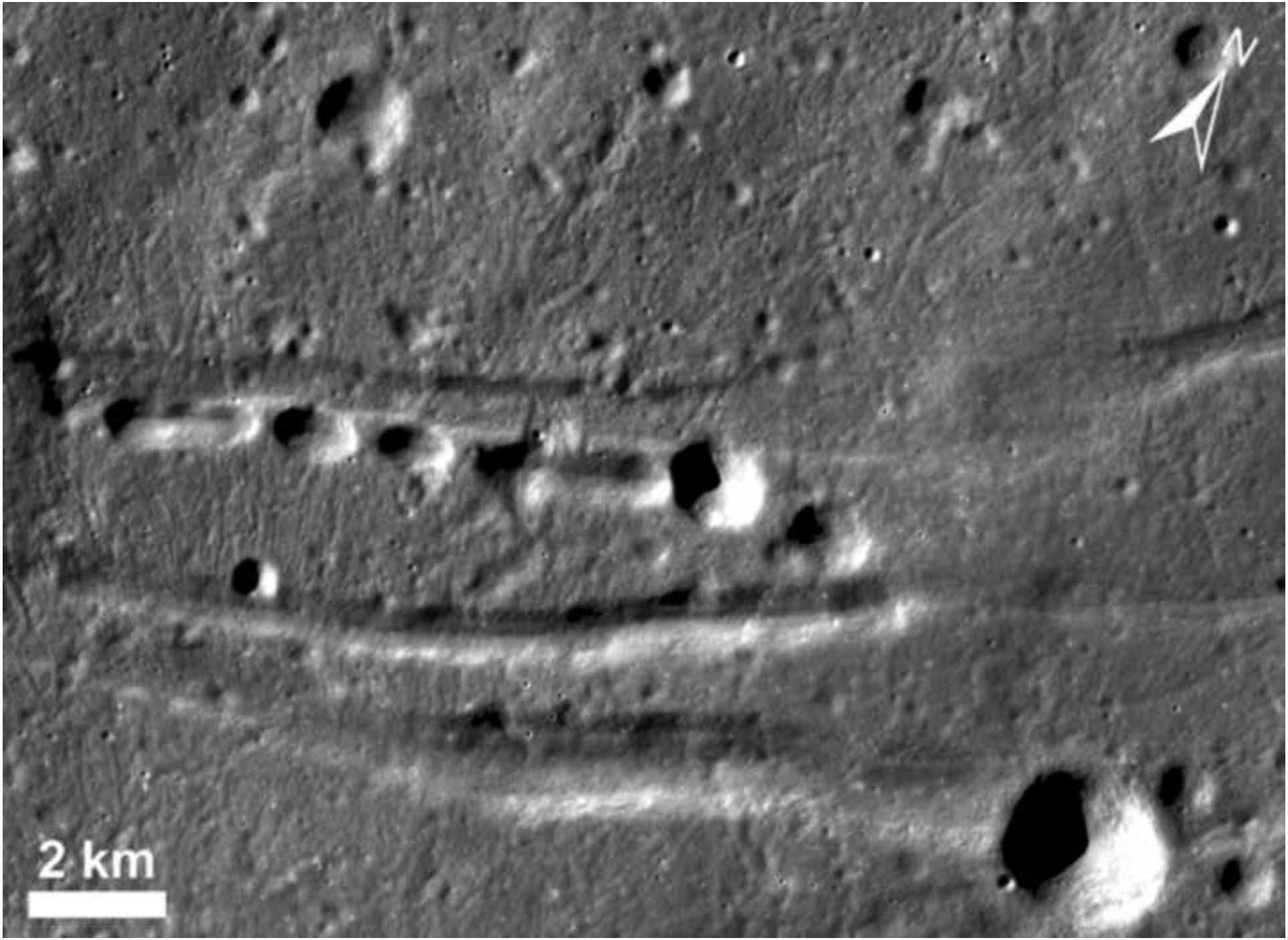

Figure 19ab

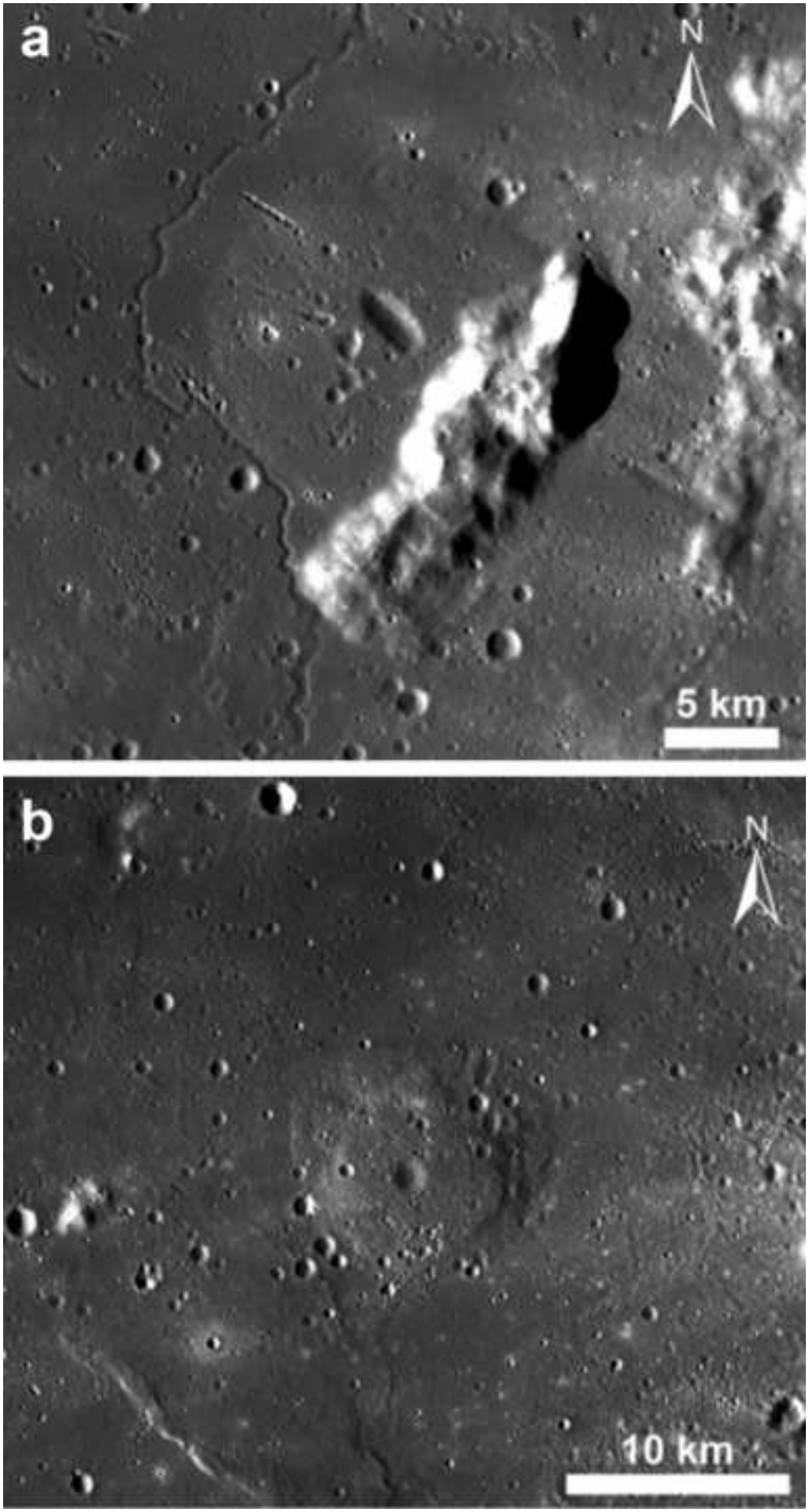

Figure 20

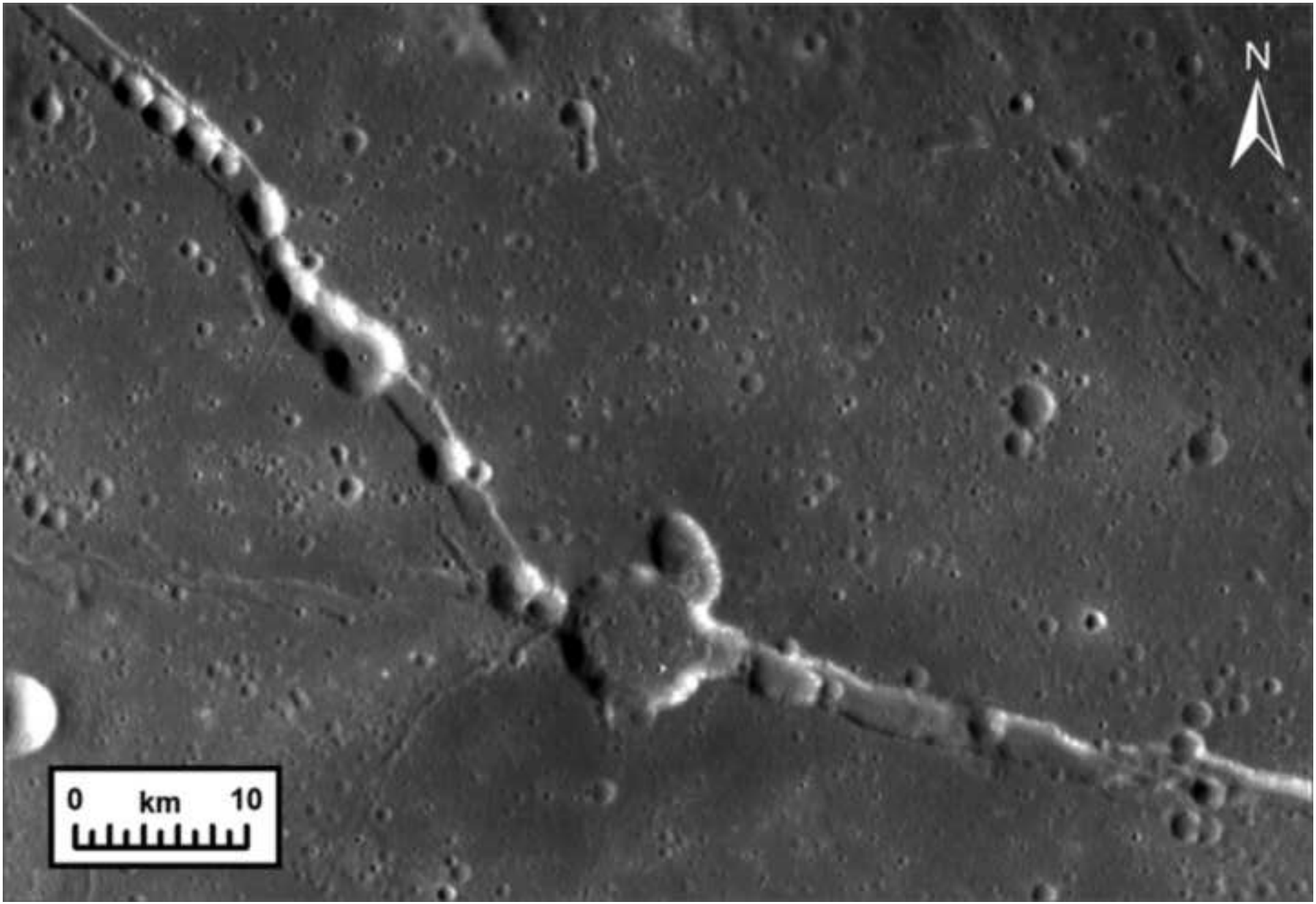

Figure 21

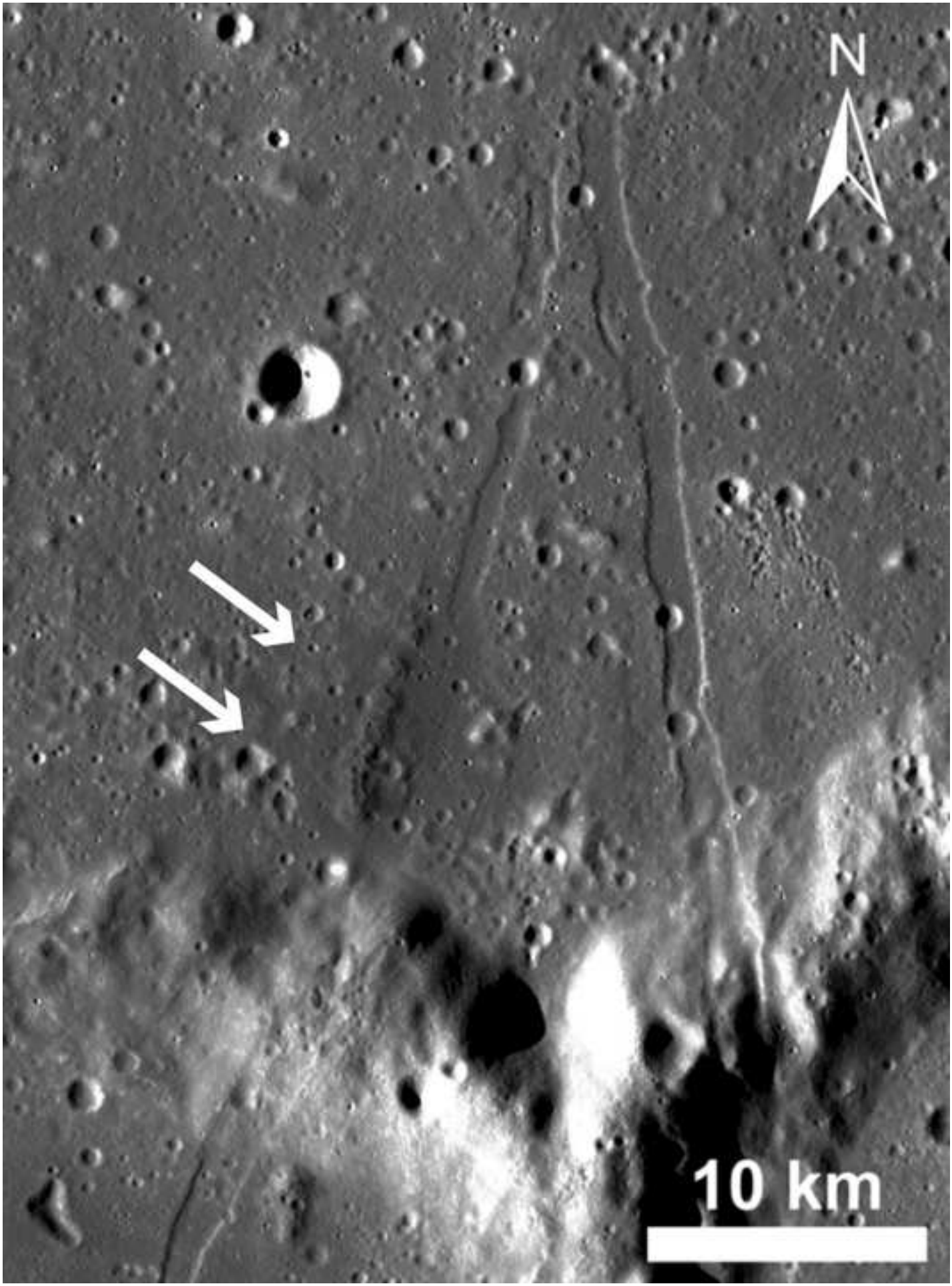

Figure 22

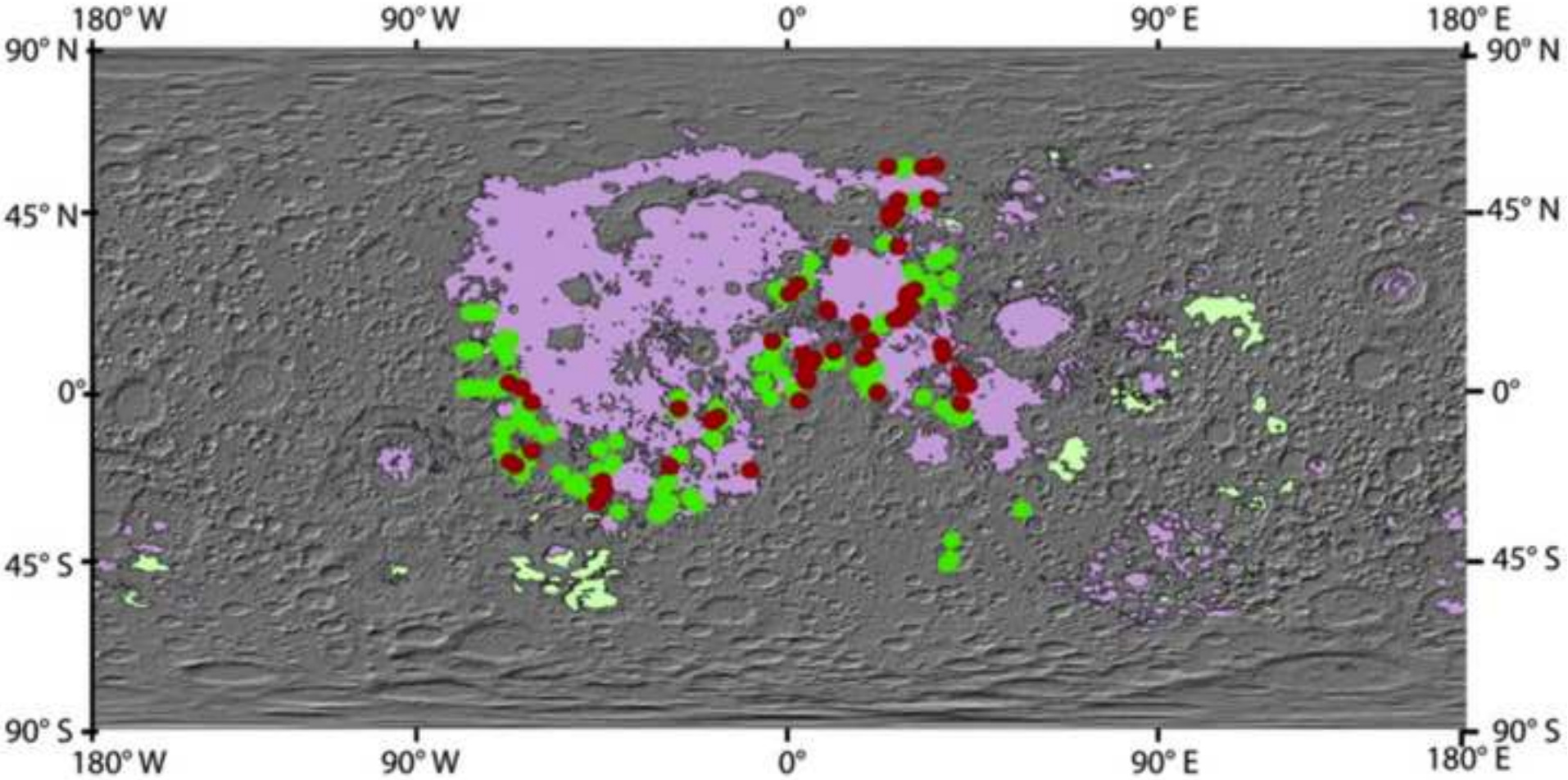

Figure 23abc

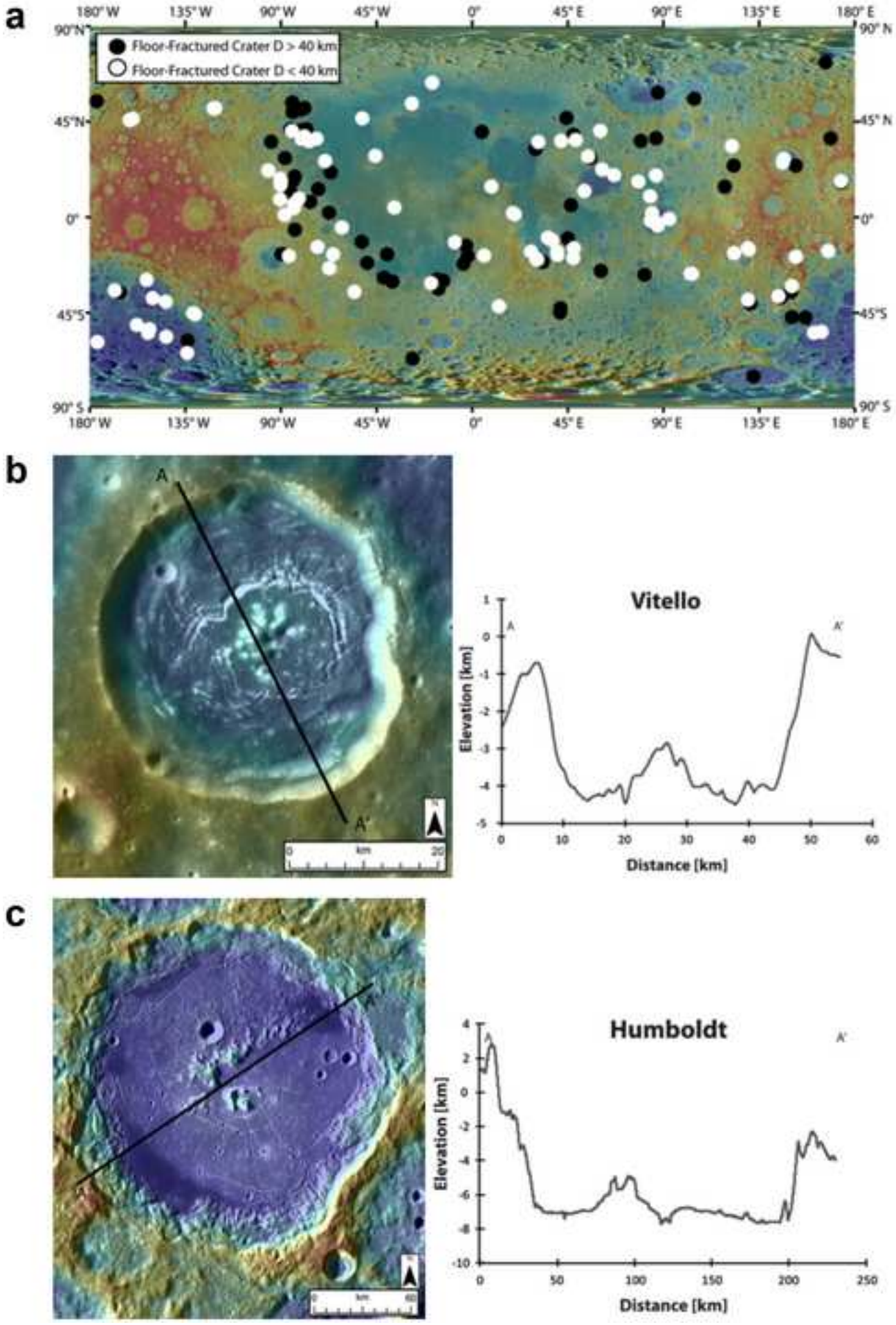

Figure 23d

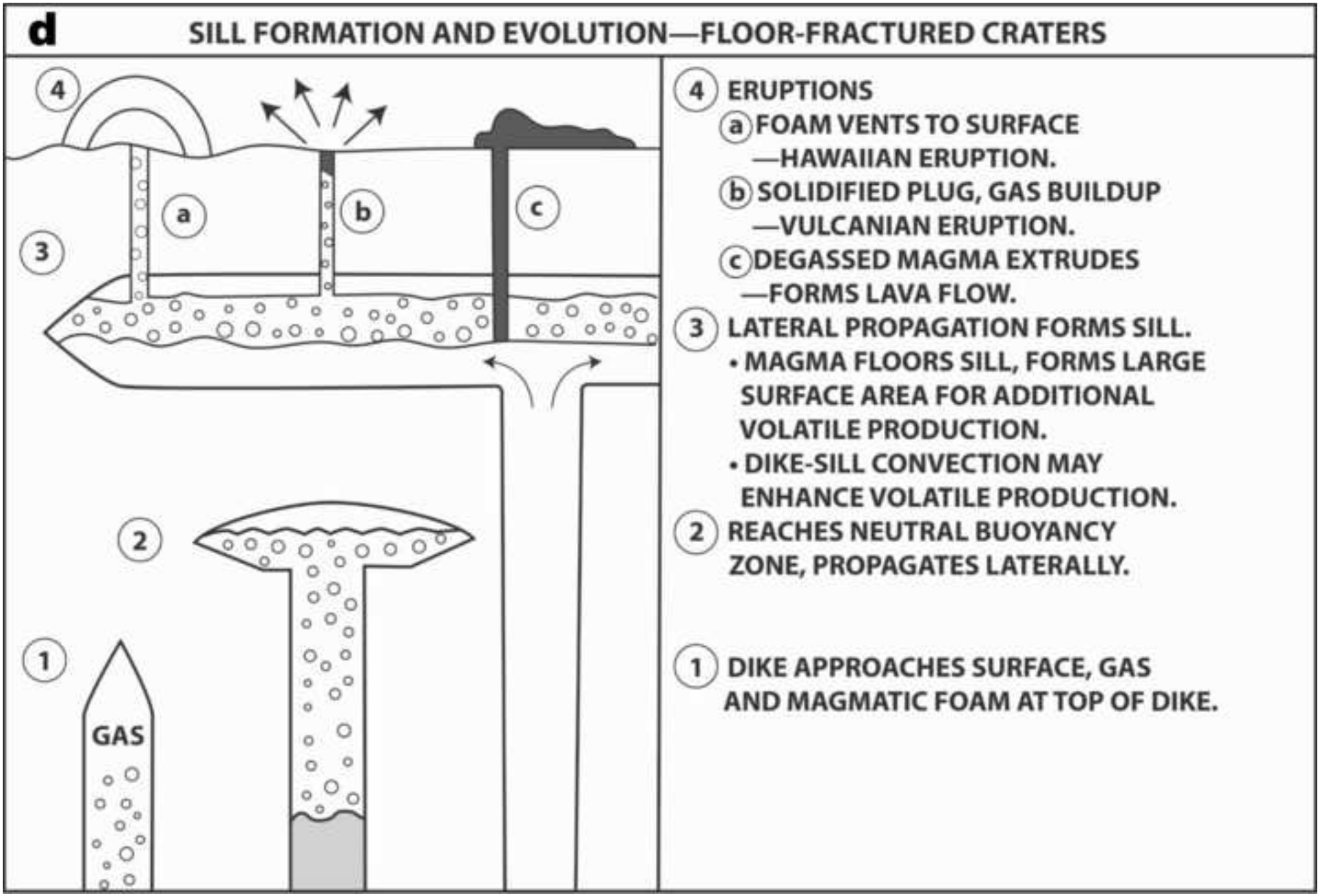
d
SILL FORMATION AND EVOLUTION—FLOOR-FRACTURED CRATERS
4
a
b
c
3
2
1
GAS
4 ERUPTIONS
a FOAM VENTS TO SURFACE —HAWAIIAN ERUPTION.
b SOLIDIFIED PLUG, GAS BUILDUP —VULCANIAN ERUPTION.
c DEGASSED MAGMA EXTRUDES —FORMS LAVA FLOW.
3 LATERAL PROPAGATION FORMS SILL.
• MAGMA FLOORS SILL, FORMS LARGE SURFACE AREA FOR ADDITIONAL VOLATILE PRODUCTION.
• DIKE-SILL CONVECTION MAY ENHANCE VOLATILE PRODUCTION.
2 REACHES NEUTRAL BUOYANCY ZONE, PROPAGATES LATERALLY.
1 DIKE APPROACHES SURFACE, GAS AND MAGMATIC FOAM AT TOP OF DIKE.

Figure 24a-e

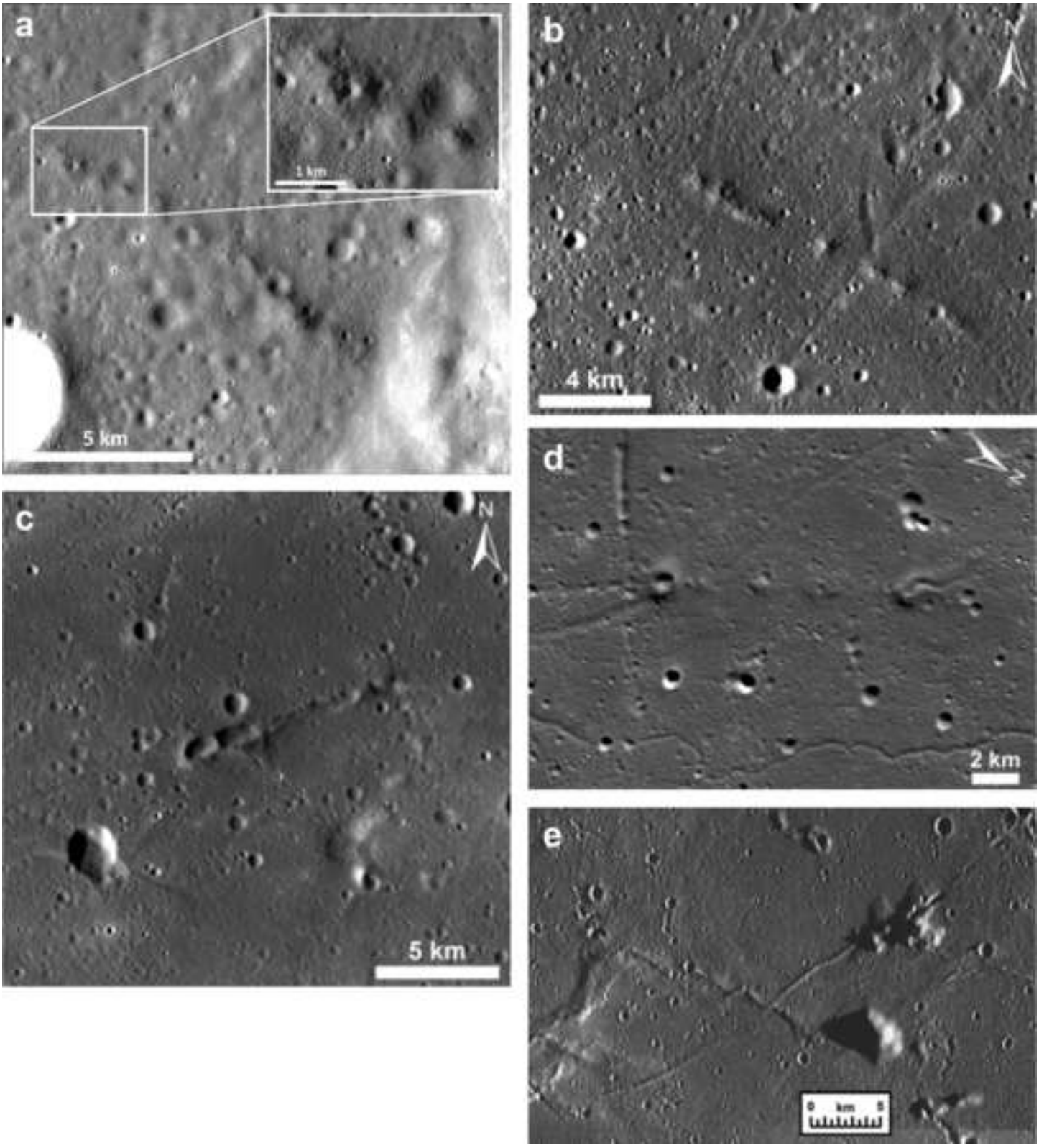

Figure 25

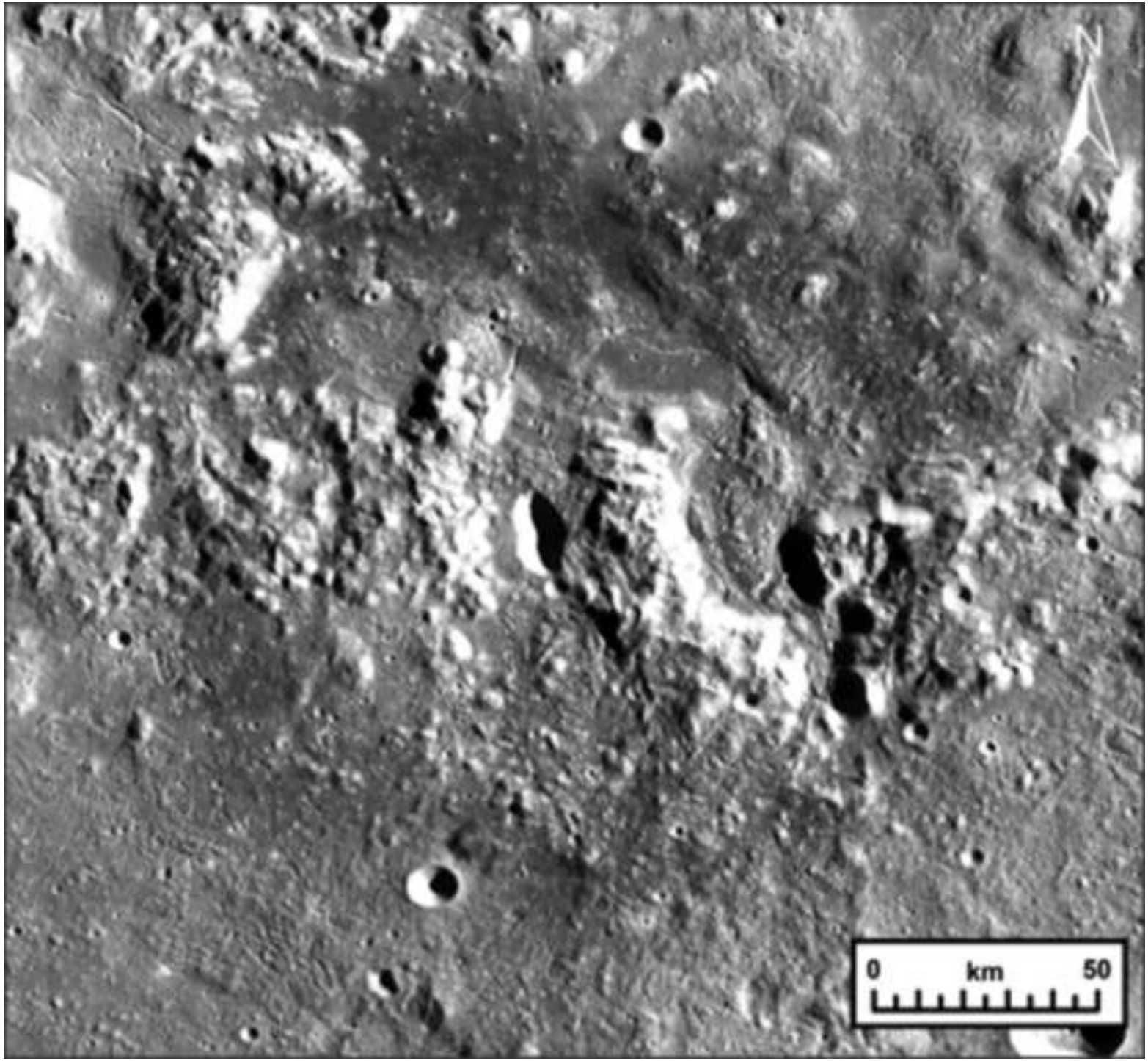

Figure 26ab

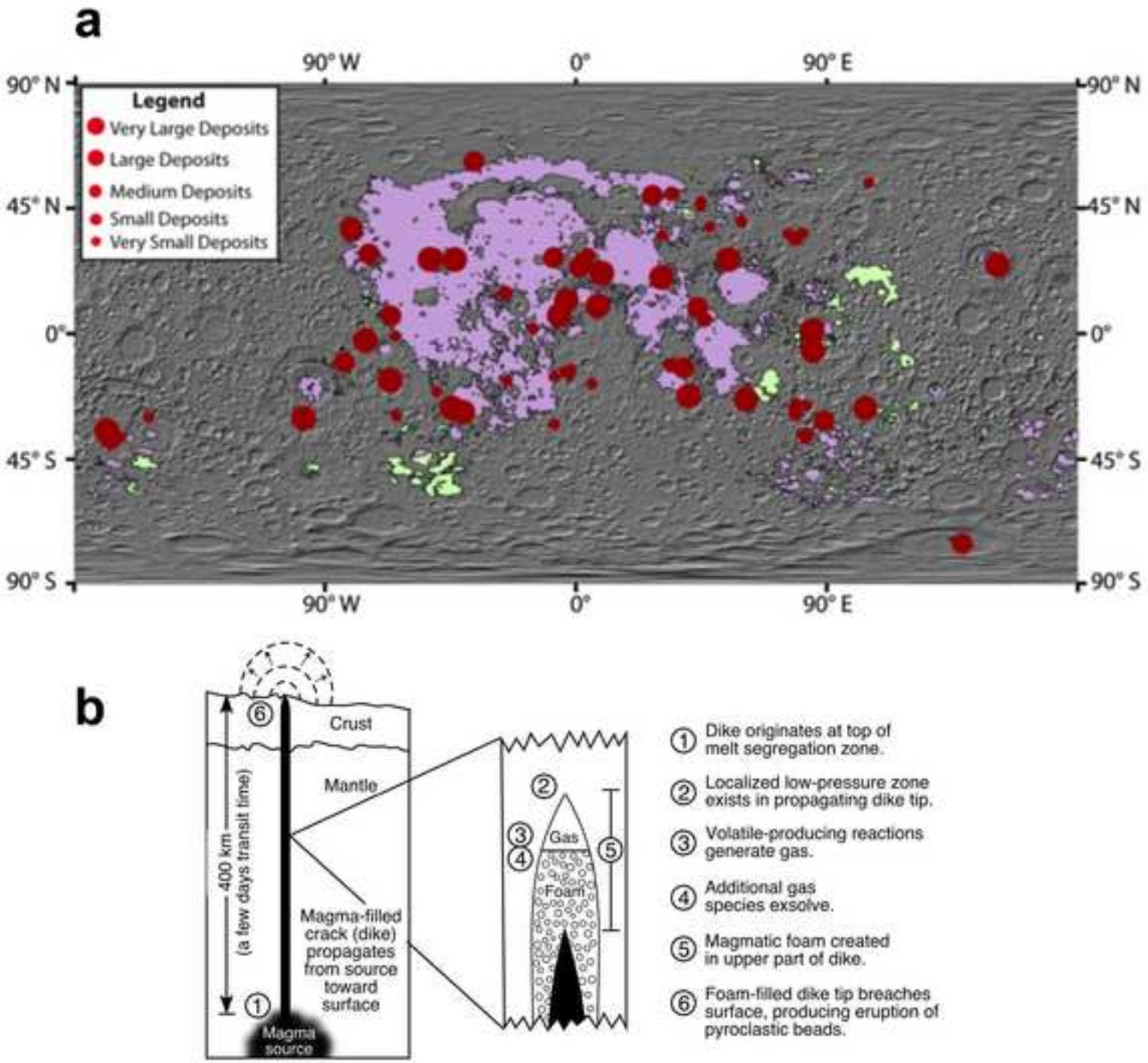
a
90° W
0°
90° E
90° N
45° N
0°
45° S
90° S
Legend
Very Large Deposits
Large Deposits
Medium Deposits
Small Deposits
Very Small Deposits
b
Crust
Mantle
400 km
(a few days transit time)
Magma-filled crack (dike) propagates from source toward surface
Magma source
Gas
Foam
① Dike originates at top of melt segregation zone.
② Localized low-pressure zone exists in propagating dike tip.
③ Volatile-producing reactions generate gas.
④ Additional gas species exsolve.
⑤ Magmatic foam created in upper part of dike.
⑥ Foam-filled dike tip breaches surface, producing eruption of pyroclastic beads.

Figure 26c-f

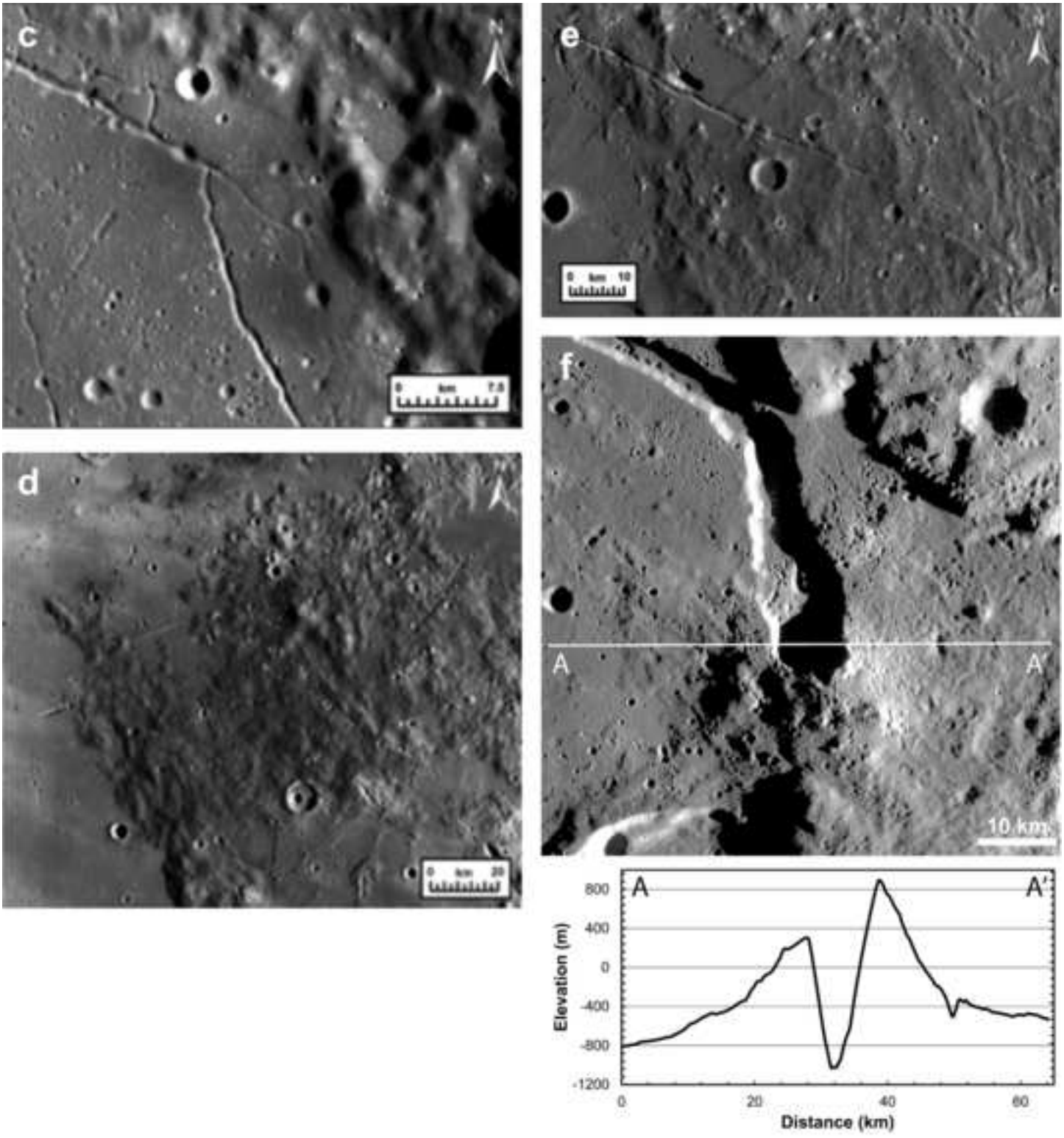
c
N
0 km 7.5
d
0 km 20
e
N
0 km 10
f
A
A'
10 km
A
A'
800
400
0
-400
-800
-1200
Elevation (m)
0
20
40
60
Distance (km)

Figure 27abc

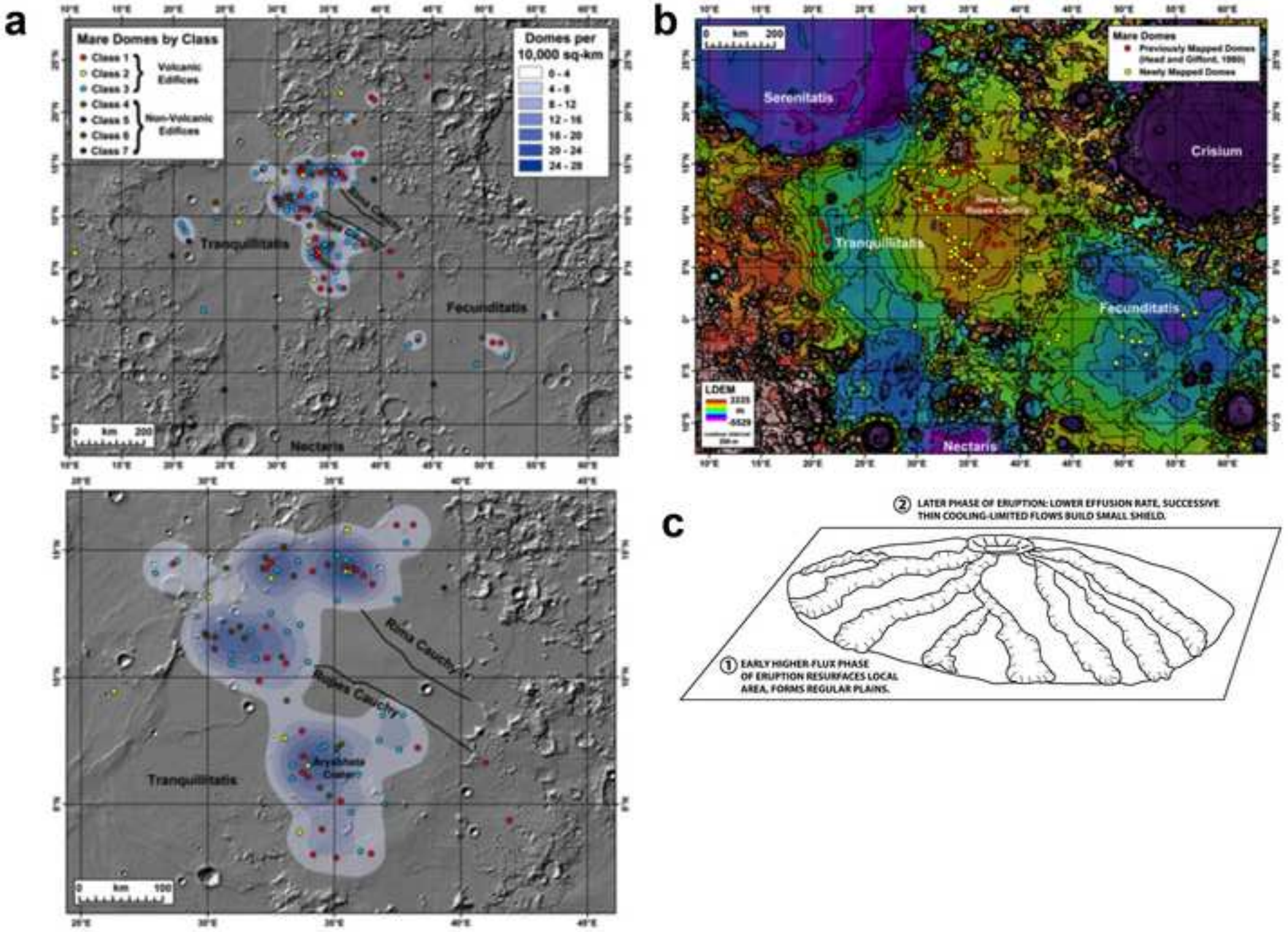

Figure 28

EARTH MAJOR SHIELD EDIFICE GROWTH

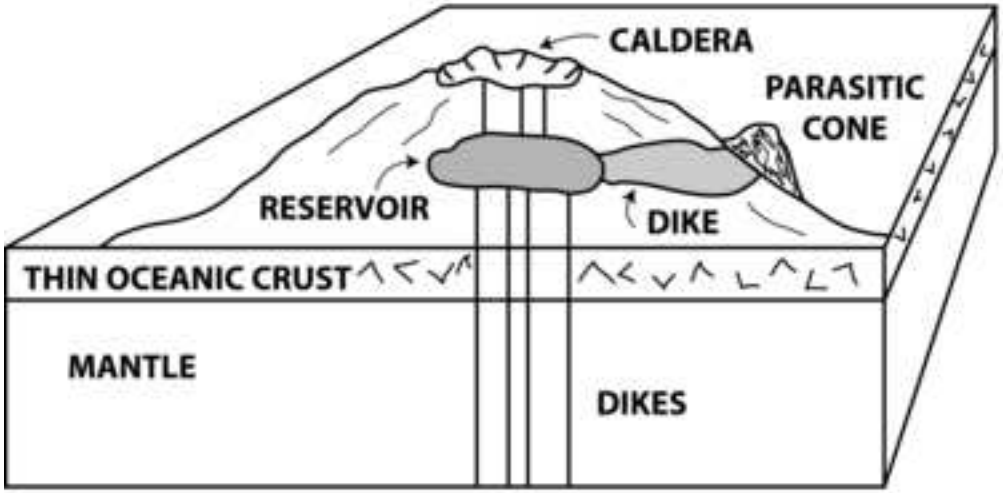

④ CALDERA COLLAPSE REFLECTS PRESENCE OF MAGMA RESERVOIR, MAGMA MIGRATION.
③ EVOLUTION OF RESERVOIR CAUSES LATERAL AND VERTICAL DIKE EMPLACEMENT AND NUMEROUS LOW-VOLUME ERUPTIONS, BUILDING EDIFICE.
② MAGMA STALLS AT NEUTRAL BUOYANCY ZONE; DIKE EMPLACEMENT FREQUENCY HIGH ENOUGH TO PRODUCE SHALLOW RESERVOIR.
① BUOYANT MAGMA RISES IN DIKES TO NEUTRAL BUOYANCY ZONE AT TOP OF CRUST OR WITHIN EDIFICE.

MOON LACK OF MAJOR SHIELD EDIFICES/CALDERAS

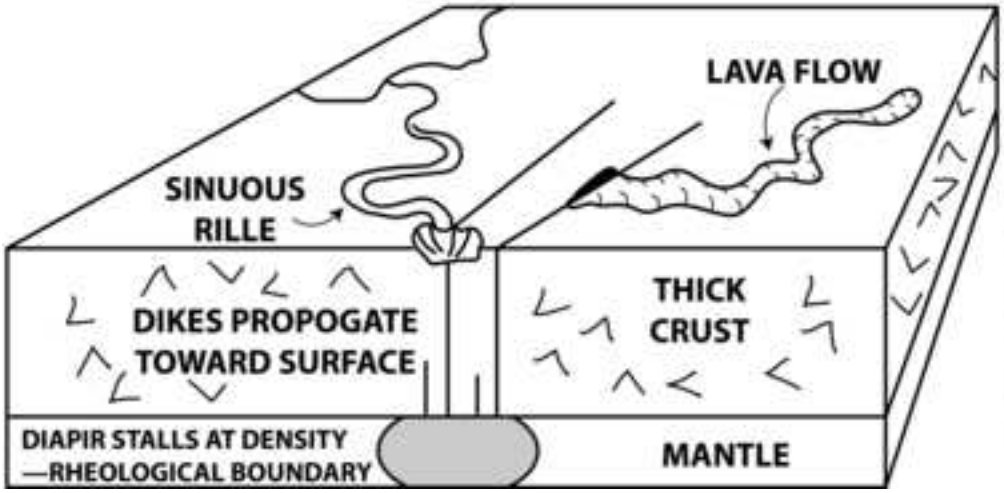

- HIGHEST VOLUME DIKES REACH SURFACE TO PRODUCE LONG FLOWS AND SINUOUS RILLES.
- DIKE EMPLACEMENT FREQUENCY TOO LOW TO PRODUCE SHALLOW RESERVOIR OR EDIFICE.
- SHALLOW CRUSTAL RESERVOIRS, LARGE SHIELDS, CALDERAS NOT FAVORED.

Figure 29abc

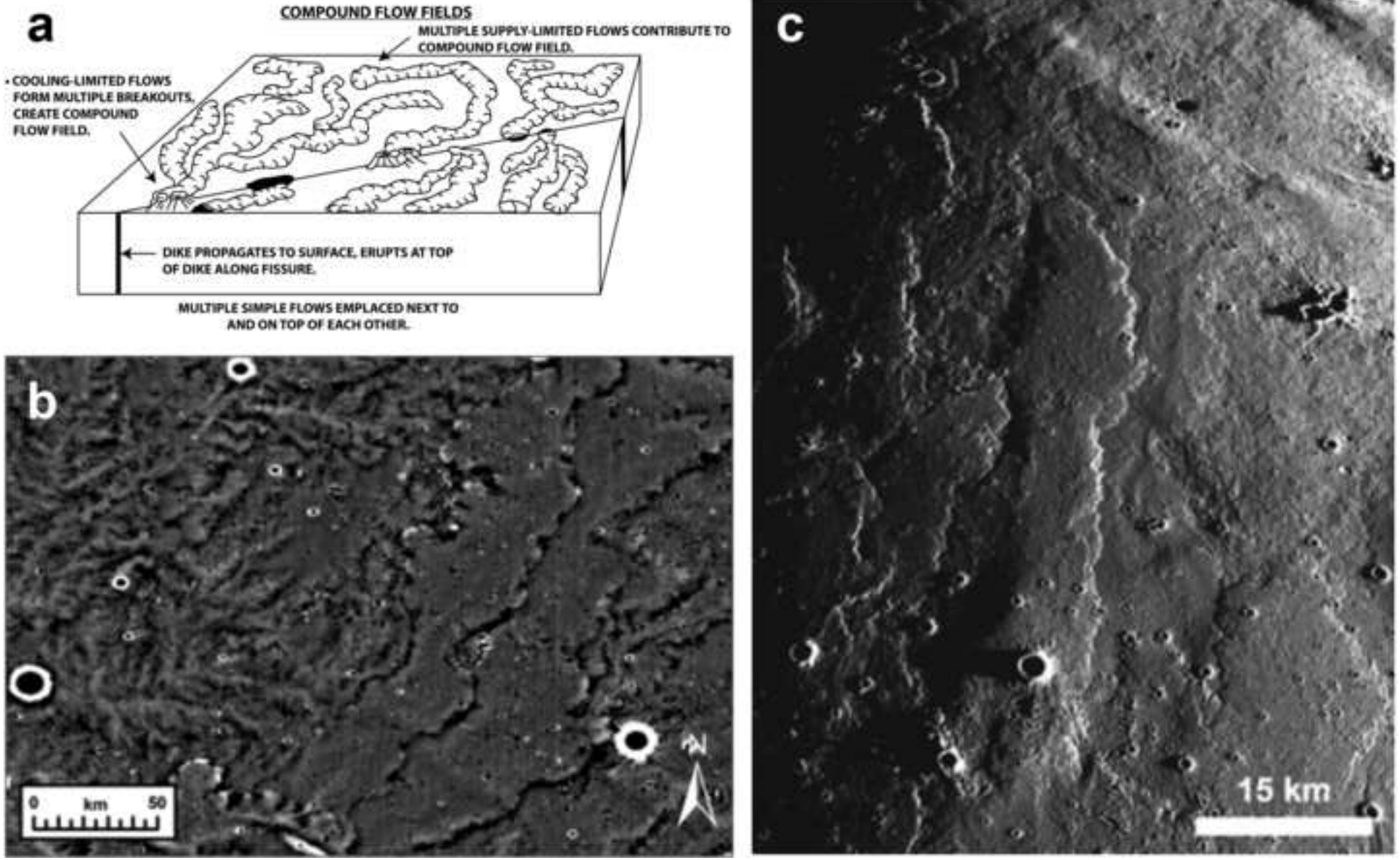

Figure 30a-e

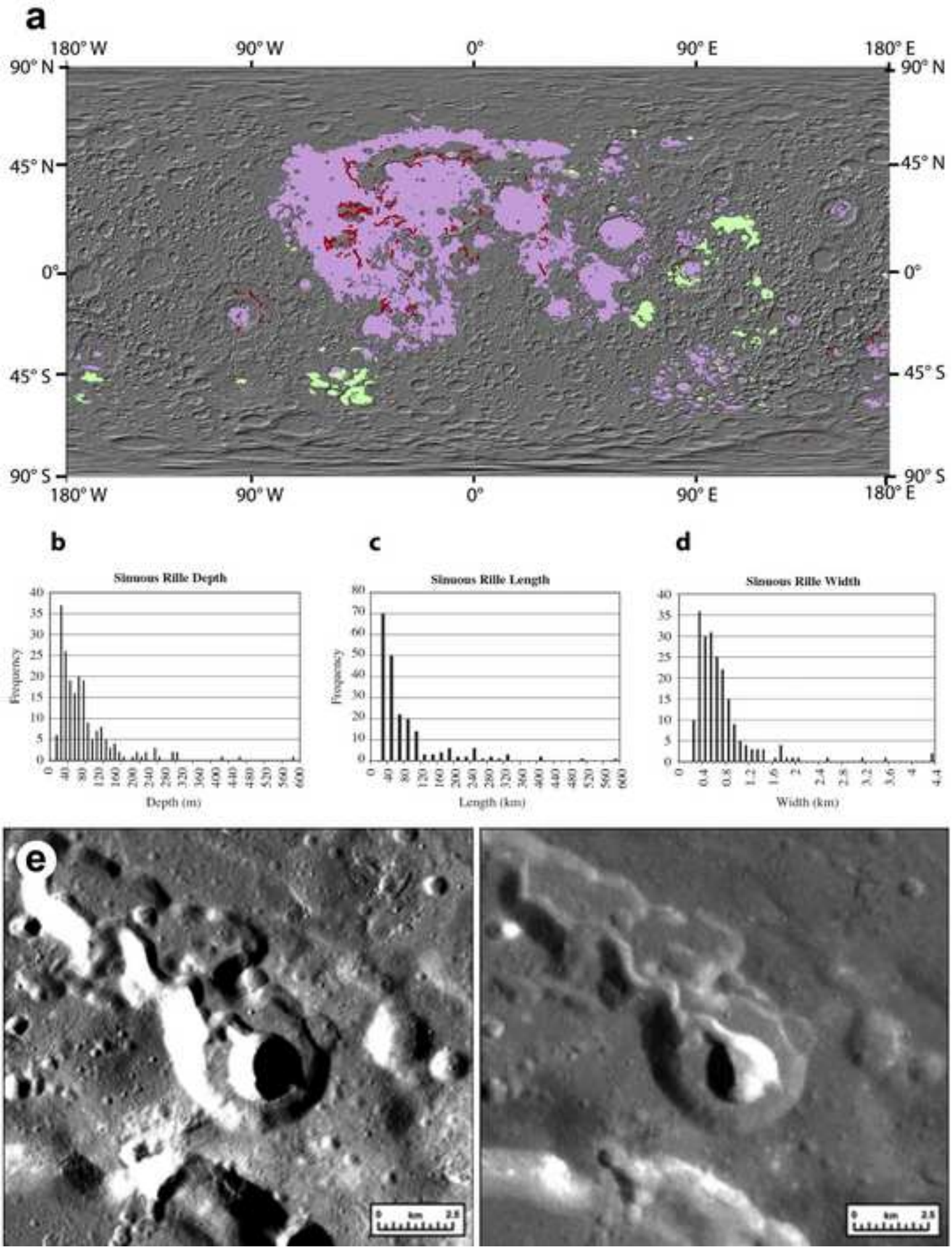
a
180° W
90° W
0°
90° E
180° E
90° N
45° N
0°
45° S
90° S
b
Sinuous Rille Depth
Frequency
Depth (m)
c
Sinuous Rille Length
Frequency
Length (km)
d
Sinuous Rille Width
Width (km)
e
0 km 2.5

Figure 31ab

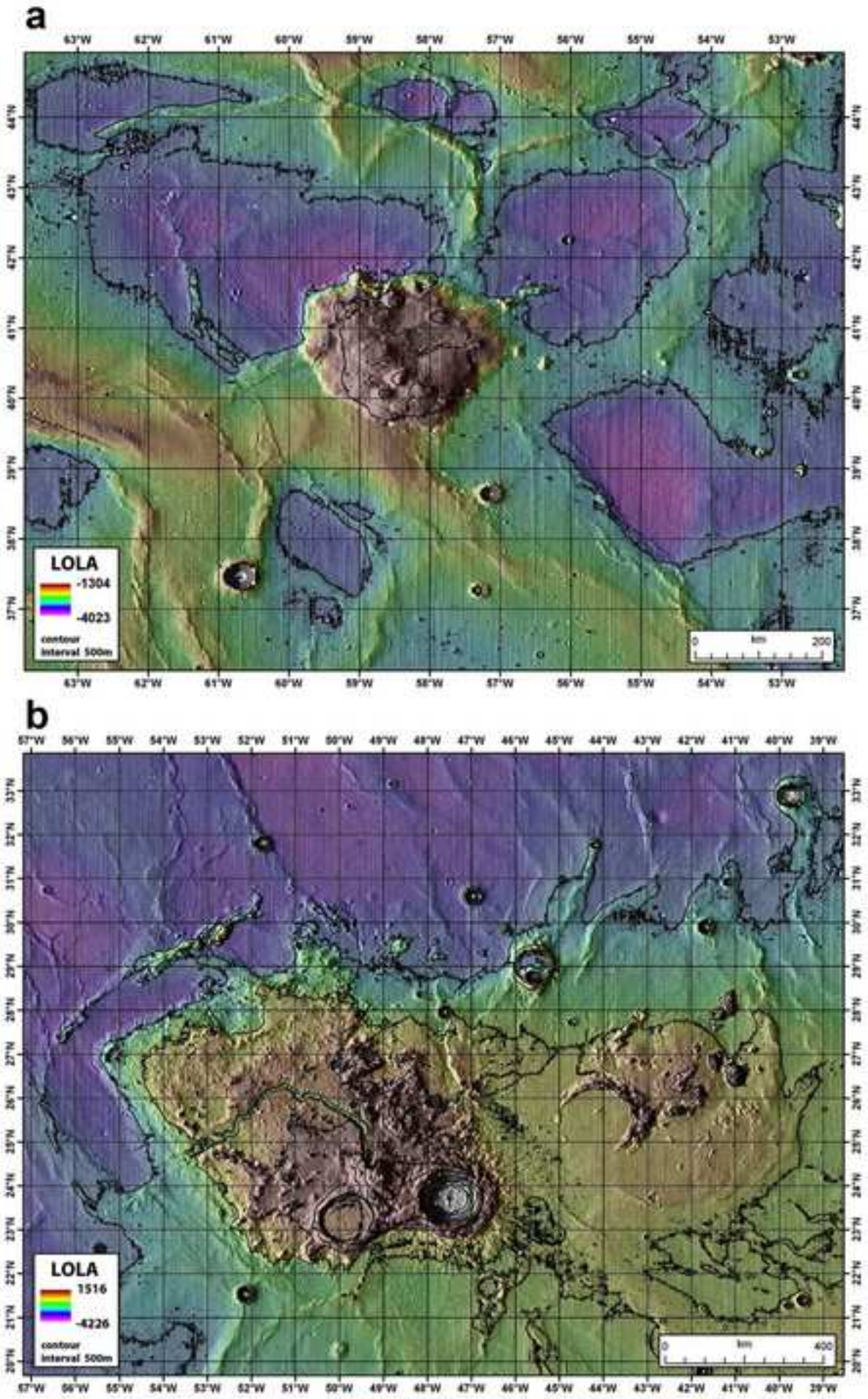
a
LOLA
-1304
-4023
contour
interval 500m
0 km 200
b
LOLA
1516
-4226
contour
interval 500m
0 km 400

Figure 31c

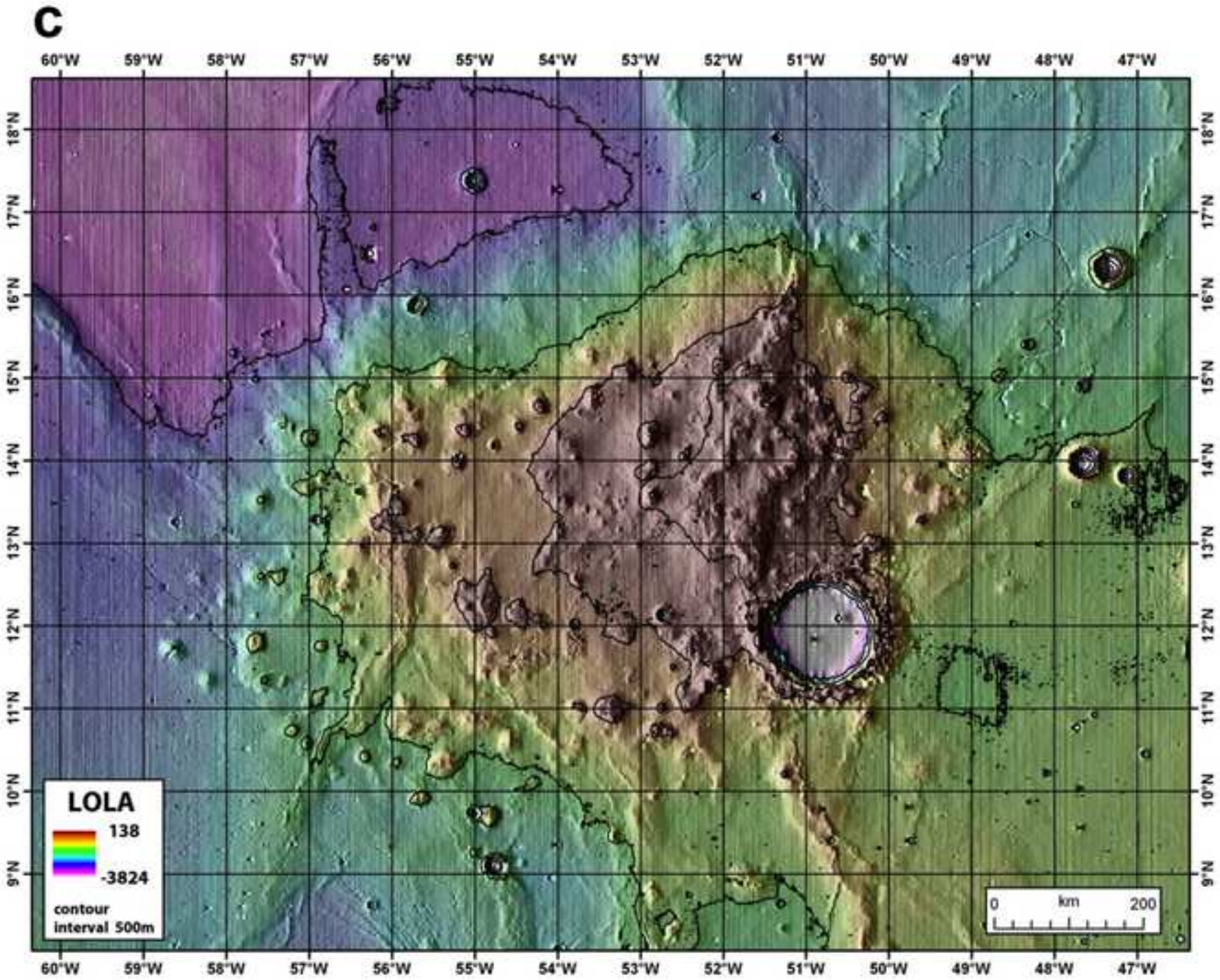
C
60°W
59°W
58°W
57°W
56°W
55°W
54°W
53°W
52°W
51°W
50°W
49°W
48°W
47°W
18°N
17°N
16°N
15°N
14°N
13°N
12°N
11°N
10°N
9°N
LOLA
138
-3824
contour
interval 500m
0
km
200

Figure 32abc

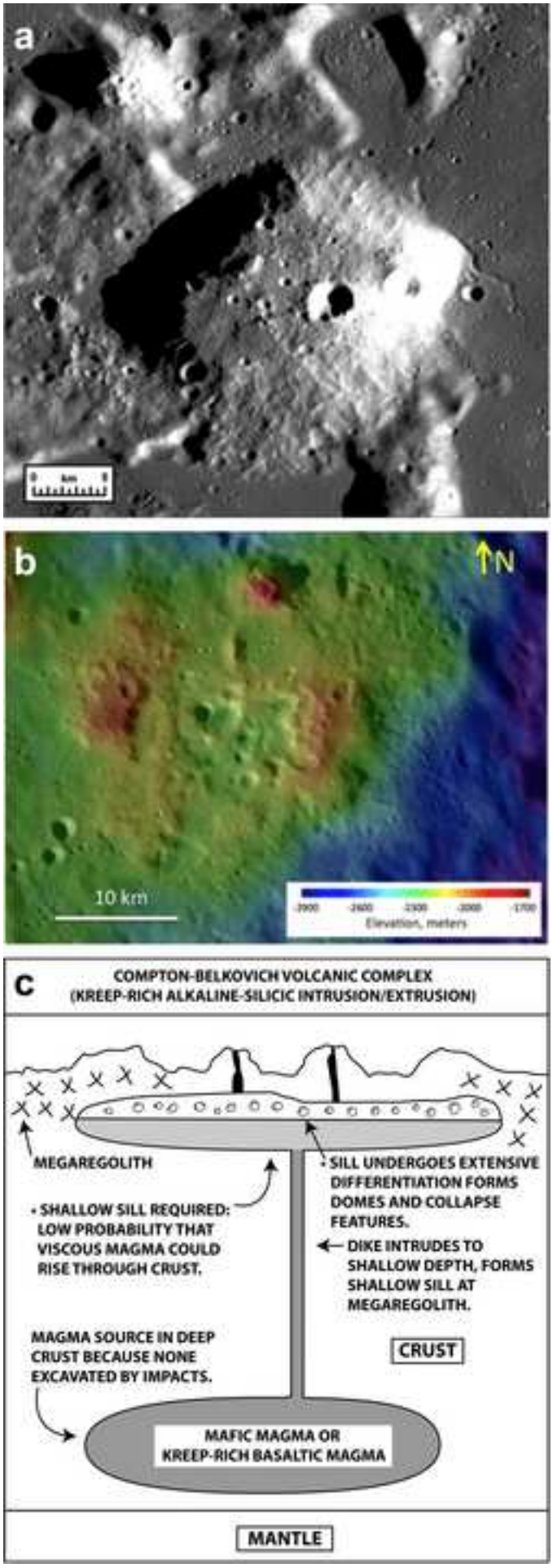

Figure 33a-d

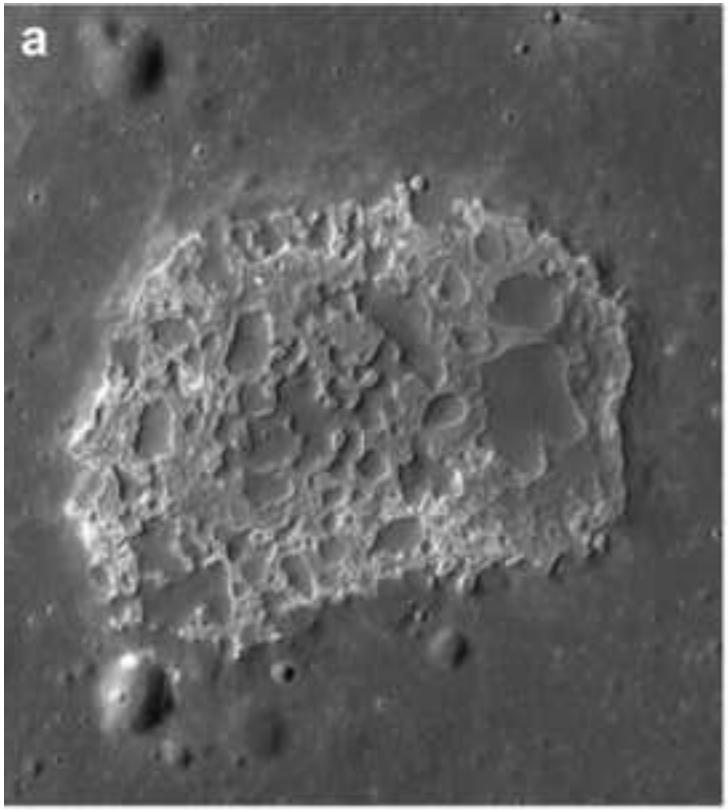

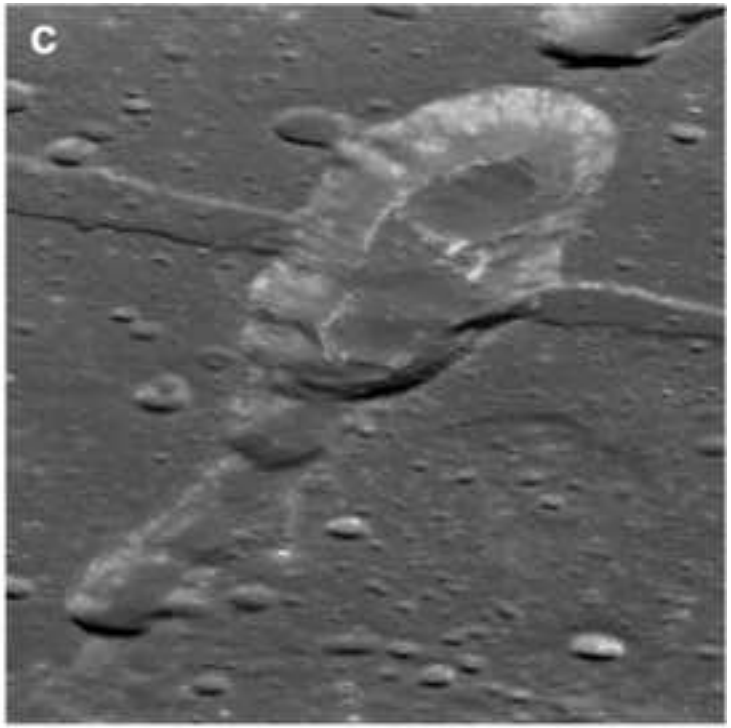

SOSIGENES STRUCTURE

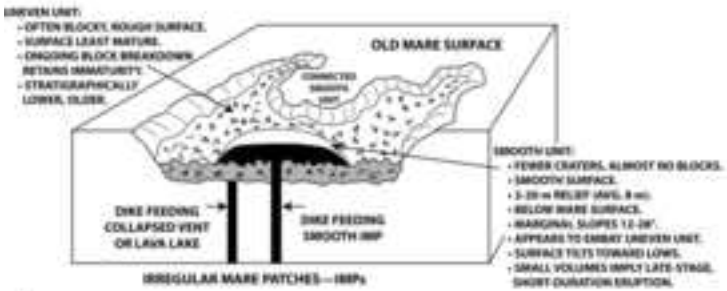

b